FORMATION, STRUCTURE AND COMPOSITION OF ANODIC-OXIDE FILMS ON BERYLLIUM

by

Mahmoud Tawfik Shehata, B.Eng.

A Thesis
Submitted to the School of Graduate Studies
in Partial Fulfilment of the Requirements
for the Degree
Doctor of Philosophy

McMaster University
June, 1978

FORMATION, STRUCTURE AND COMPOSITION
OF ANODIC-OXIDE FILMS ON BERYLLIUM

DOCTOR OF PHILOSOPHY (1978)
(Metallurgy and Materials Science)

MCMASTER UNIVERSITY
Hamilton, Ontario

TITLE: Formation, Structure and Composition of Anodic-Oxide Films on Beryllium

AUTHOR: Mahmoud Tawfik Shehata, B. Eng. (Cairo University, Egypt)

SUPERVISOR: Professor R. Kelly

NUMBER OF PAGES: xiii; 172

ABSTRACT

The formation, structure and composition of anodic-oxide films on Be is investigated. According to the choice of electrolyte, porosity, dissolution and crystallinity can be varied almost at will for the formed anodic films. Also the procedure for the anodic sectioning of Be is described and applied to determining the depth distributions of energetic ^{85}Kr ions.

The presence and the distribution of electrolyte components that are incorporated into the anodic films are investigated by the photon-emission technique. The depth profiles of the incorporated species are correlated with the mechanism of film formation.

Finally, a criterion for the structure of anodic oxide films on metals is developed based on the kinetics of the formation and crystallization processes of the various oxides. The criterion is applied and found to work successfully with all systems for which information is available, whereas for unstudied systems it enables predictions to be made.

ACKNOWLEDGEMENTS

I would like to express my sincere gratitude to Dr. Roger Kelly for his continuous guidance, encouragement and friendship throughout the course of this work.

I wish to express my thanks to the members of my supervisory committee, Drs. W.W. Smeltzer and J.A. Davies for their interest and encouragement. Thanks are extended to the many members of the Department of Metallurgy and Materials Science who contributed helpful comments and advice.

I wish to thank Mrs. Horridge for her skill and patience in typing this thesis, and I also thank D. Hodgson for the excellent drawings and photographs he did for the thesis.

I gratefully acknowledge the support of the National Research Council by grants to Dr. Kelly and McMaster University for support to the author.

Finally, I am deeply greatful to my wife, Amira, for her patience and constant support throughout the course of this work.

TABLE OF CONTENTS

LIST OF ILLUSTRATIONS

LIST OF TABLES

TABLE NO. PAGE

CHAPTER 1

INTRODUCTION

The pioneer work of Güntherschulze and Betz in the 1930's initiated much of the present day interest in the formation of anodic films. Such films have been used extensively in the capacitor industry for over forty years, with other important uses being in microcircuitry (1) and thin-film technology (2). More recently, major indirect uses have emerged for anodic films in the fields of ion-implantation, radiation damage and low-temperature diffusion. These new uses all centre around the possibility of anodic sectioning.

Anodic sectioning permits the quantitative removal of thin, uniform layers from a metal or semi-conductor surface, so that a detailed knowledge of the depth distribution of, for example, implanted ions can be determined. This in turn gives information about how deep the implanted ions (often a dopant in the case of semi-conductor) have penetrated. Similarly, in the field of radiation damage, the distance that an energetic recoil atom travels through the solid can be experimentally determined. A closely related problem is that of determining diffusion profiles under extreme conditions involving small thicknesses. As an example of comparing the various techniques employed to determine self-diffusion coefficients, use of lathe sectioning permits measurements of D down to $\sim 10^{-13}$ cm^2/s, chemical etching enables one to go to about 10^{-15} - 10^{-16} cm^2/s, whereas anodic sectioning (where possible) permits measurements to about 10^{-18} - 10^{-19} cm^2/s.

The present work will be seen to open up the possibility of studying depth distributions and diffusion in the lightest target that can be conveniently worked with in the field of atomic collisions, namely Be (mass 9).

In anodic sectioning, use is made of the fact that, when anodic oxidation is carried out at constant voltage and the electrolyte is suitable, then within a few minutes the film thickness approaches an almost constant value and the resulting film is extremely uniform (3). If such a film can be removed without affecting the substrate, then it should be possible to remove uniform layers of the metal with thicknesses down to 10-20A° (Table 1.1 (4)).

TABLE 1.1. Metal-removal thicknesses for anodic sectioning (4).

Metal	Minimum thickness (Å)	Maximum voltage	Maximum thickness (Å)
Al	30	400	3500
Mo	30	100	1100
Nb	15	70	700
Ta	10	100	400
V	50	100	1300
W	10	75	400
	15	140	800

We may point out that the difficulty in anodically sectioning Be, or in fact most metals, appeared at first sight to lie in establishing the conditions under which films could be formed which were simultaneously barrier-type, stable, and amorphous. Being barrier-type assures that a voltage-dependent limiting film thickness exists, stability assures, in a general sense, that the film does not dissolve extensively in the electrolyte during formation, while amorphicity often plays a role in enabling the films to be chemically stripped without the metal substrate being attacked. (Amorphous substances have a higher chemical potential than do crystalline substances.) In addition, it will emerge that the incorporation of electrolyte components into the films may, provided the component is appropriate, enhance the stripping of the film, thus leading to anodic sectioning.

In this dissertation, the formation, structure and composition of anodic-oxide films on Be is investigated. It will emerge that, according to the choice of electrolyte, porosity, dissolution, and crystallinity can be varied almost at will for the formed anodic film. In addition, the principles of perfect anodic sectioning of Be will be described and the application to determining the depth distributions of energetic ^{85}Kr ions will be considered. The results with Be showed the expected mixture of random and channelled stopping, whereas those in BeO showed random stopping alone. The latter is of interest in constituting an independent proof that anodic BeO is amorphous.

The presence and the distribution of electrolyte components that are incorporated into anodic films are investigated by the recently developed photon-emission technique. The profiles of the incorporated species will be seen to correlate with the mechanism of film growth with both Be and Zr. Thus it is concluded that the mechanism is dominantly cation transport with Be, whereas with Zr it is dominantly anion transport.

The Zr result obtained here, being similar to previous work, served as an indication for the effectiveness of the approach used. More important to the topic of anodic sectioning, the Zr results suggest that the possibility of altering the chemistry of anodic ZrO_2 by doping does not exist.

Finally, a criterion for the structure of anodic oxide films on metals is developed based on the kinetics of the formation and crystallization processes of the oxide. The criterion will be seen to work successfully when applied to all systems for which information is available, whereas for unstudied systems it enables predictions to be made.

Due to the interdisciplinary nature of this investigation, a general background review for the formation and structure of anodic films on metals is given in Chapter 2, and a similar review for the recently developed photon-emission technique is given in Chapter 5.

REFERENCES TO CHAPTER 1

1. D.A. McLean, Proc. Nat. Electronics Conf. U.S.A. (1960) p. 206.

2. W.L. Wilcox, D.L. Emerson, and B. Weekly, Inst. Radio Engrs. Trans. Nucl. Science NS-7 (1960) 126.

3. A. Charlesby, Atomic Energy Research Establishment U.K. Rept. M/R 714 (1951).

4. M.R. Arora and R. Kelly, Electrochimica Acta, 19 (1974) 413.

CHAPTER 2

FORMATION AND STRUCTURE OF ANODIC FILMS

(Background)

2.1 Formation of Anodic Films

Most of our present knowledge on the formation of anodic oxide films is concerned with the so-called "valve metals" of which Ta is often taken as the most typical example. (This was historically due to the technical importance of anodized Ta in the manufacture of capacitors). A thin air-formed oxide film is always present on the surface of a valve metal, which is insoluble in all but the most corrosive of electrolytes. When such a metal is made the anode of an electrolytic cell, and a voltage is applied, this voltage will produce a continuing growth of the oxide film by causing metal and/or oxygen ions to be pulled through the film. The growth of this film will be reflected by a continuous increase in the potential of the electrode to maintain the field through the film as will be discussed later (Sec. 3.3). The relationship between the anodic current and the electric field across the oxide film is generally found experimentally, at least to a first approximation, to follow an equation of the form:

$$i = A \exp(BE) \qquad (2.1)$$

where i is the ionic current, E is the field strength, and A and B are constants. The potential of the electrode may reach as much as 400 volts and the thickness of the film can be as much as several hundred nanometers. At thicknesses corresponding to voltages in excess of 5-15 V, interference colours are usually observed at the anode. The formation of the film is normally limited by electrical breakdown and oxygen evolution, both of which occur after a certain potential (or certain thickness) is reached.

It is worth pointing out, however, that although the above example represents typical behaviour of a valve metal, yet it is probable that no system adheres strictly to this description. For example, anodic-oxide films formed on aluminum are of two types. In neutral or weakly alkaline solutions the resultant films are continuous and behave essentially like those described above. On the other hand, films formed in most acidic solutions are found to be porous and discontinuous, and may grow at an almost constant voltage to thicknesses of several micrometers. These porous, discontinuous films may be attributed to the dissolution of some parts of the film in the solution.

The films which concern us here will be mainly of the non-porous, protective type which are stable towards the electrolyte. When such films are poor electronic conductors, ion conduction becomes the predominant mode of charge transport and the films consequently grow by such ion transport to a thickness approximately proportional to the forming voltage. Al(1,2), Be(3), Ge(4), Hf(5), Mo(6), Nb(7,8), Ta(2,9), Ti(10), Si(11), Sn(12), U(13), V(14), W(7,8) and Zr(15-17) readily give such films when anodized in a suitable electrolyte.

2.2 Thermodynamic Basis (Pourbaix diagrams)

All anodic reactions involving a metal and an aqueous solution, in the absence of complex-forming or precipitating anions other than hydroxyl, follow one or another of the following general overall processes:

$$M \rightarrow M^{z+}_{aq} + ze \qquad 2.2$$

$$M + zH_2O \rightarrow M(OH)_{z\ solid} + zH^+ + ze \qquad 2.3\ a$$

$$M + zOH^- \rightarrow M(OH)_{z\ solid} + ze \qquad 2.3b$$

$$M + zH_2O \rightarrow MO_{z\ aq}^{z-} + 2zH^+ + ze \qquad 2.4a$$

$$M + zOH^- \rightarrow MO_{z\ aq}^{-} + zH^+ + ze \qquad 2.4b$$

or other obvious equivalents in terms of hydroxy-oxides and metal oxy-anions containing hydroxyl groups. The pairs of processes represented by (2.3a) and (2.3b), and (2.4a) and (2.4b), are thermodynamically identical apart from the choice of the standard states, although they represent different atomistic paths for the reaction. In all cases the formulae represent overall processes and make no statement about detailed intermediate mechanisms. It should be noted that the anodic reactions (2.2) and (2.4) fall under the category of anodic dissolution processes whereas reaction 2.3 constitutes anodic passivation.

The electrode potentials of the half-cells based on the reversible reactions corresponding to processes (2.2), (2.3) and (2.4) have been measured, or computed from thermodynamic data, for many metals. Pourbaix(18) and his school have collected, assessed and collated such data, together with data for oxide or hydroxide solubilities, in a series of equilibrium diagrams in which the variation of the half-cell potentials and the solubilities of the solid phases with the pH of the solution at room temperature are plotted. Fig. 2.1 shows such a diagram for beryllium. It shows, among other things, that for potentials higher than ∿ -2.0 volts beryllium will tend to form a passive oxide or hydroxide layer in solutions of 4-10.5 pH. On the other hand, it will tend to dissolve in solutions forming Be^{++} at $pH < 4$ or $Be_2O_3^{--}$ at $pH > 10.5$.

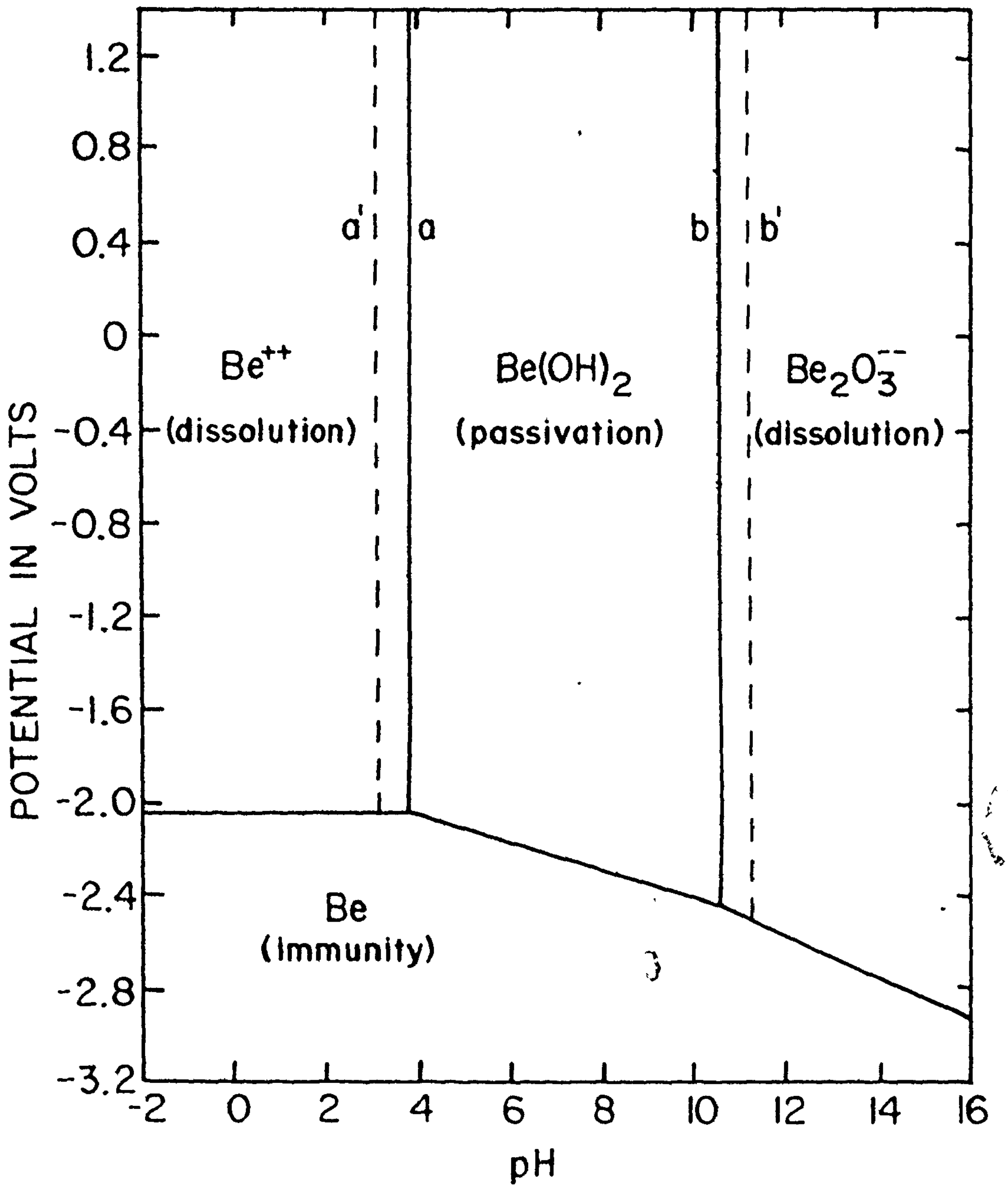

Fig. 2.1. Potential-pH diagram for beryllium at 25°C (Simplified) after Pourbaix$^{(18)}$.

The potential-pH diagrams are very useful because they give at a glance a picture of the expected reactions of an electrode in solution. In general, they are in a reasonable accord with the observed behaviour of electrodes. Thus, if a particular compound of an electrode material exists, it can usually be formed in a solution of the suitable pH and at a potential not far from the potential calculated from thermodynamic data.

However, it should be noted that under the formation conditions of anodic–oxide films, which may be far from equilibrium, it is possible for the behaviour of the electrode to deviate from that predicted by the diagram. Two examples are, first, that anodic–oxide films can be formed on most metals in acid solutions where they are in principle unstable, and, second, the fact that the hydration of films is normally different from that predicted. The first point can be understood by considering that at large over-voltages the rate of formation of a phase may exceed its rate of dissolution, so that equilibrium is not achieved. To some extent this would correspond to boundary shifts like a to a' and b to b' as in Fig. 2.1. The second point could be understood in terms of severely hindered kinetics of diffusion of OH^- or equivalent groups. It should also be mentioned that such formation conditions, deviating from equilibrium, can in effect produce different time-dependent conditions at the electrode surface, so that the anodic reaction may be a function of the time and/or current density. In spite of the limitations of the potential-pH diagrams described above regarding the formation conditions of anodic oxide films, the diagrams were found in this work to be a very useful first approximation to understanding why various electrolytes, almost invariably chosen without consideration of the Pourbaix diagrams, were or were not effective. Examples are shown in Table 2.1, where the electrolytes used to form anodic films on most metals are found to be in good agreement with the pH range that could be predicted from their potential-pH diagrams. Shown, for example, are simplified diagrams for Al, W and Ta in Fig. 2.2. The only exception, probably indicative of uncertainty in the Pourbaix diagram, occurs with Nb, films on which were recently shown to be soluble in alkaline solutions (7).

Table 2.1 Examples of electrolytes which are used to form anodic films on various metals and the predicted pH range for passivation from the Pourbaix diagram. The agreement is quite good except for Nb, where films are soluble in alkaline solutions.

Metal	pH range predicted(18)	Electrolyte used	Reference
Al	3.5-8.5	5% ammonium pentaborate	1
Sn	1-9	1 liter ethylene glycol, 300 ml water; 330 g ammonium pentaborate	12
Zr	4-12.5	3% ammonium pentaborate	16,17
Ge	< 6	sodium acetate in acetic acid	4
Mo	< 4	glacial acetic acid; 0.02 M $Na_2B_4O_7 \cdot 10H_2O$	6,8
Si	< 11	ethylene glycol; 4% water; 0.4% KNO_3	11
V	< 4.5	see Mo	14
W	< 4	water; 0.4 M KNO_3; 0.04 M HNO_3	8
Nb	any; possibly not basic	0.2% KF; also H_2SO_4 + $(C_2H_5)_2SO_4$.	8,7
Ta	any; possibly not basic	see Nb	9,7

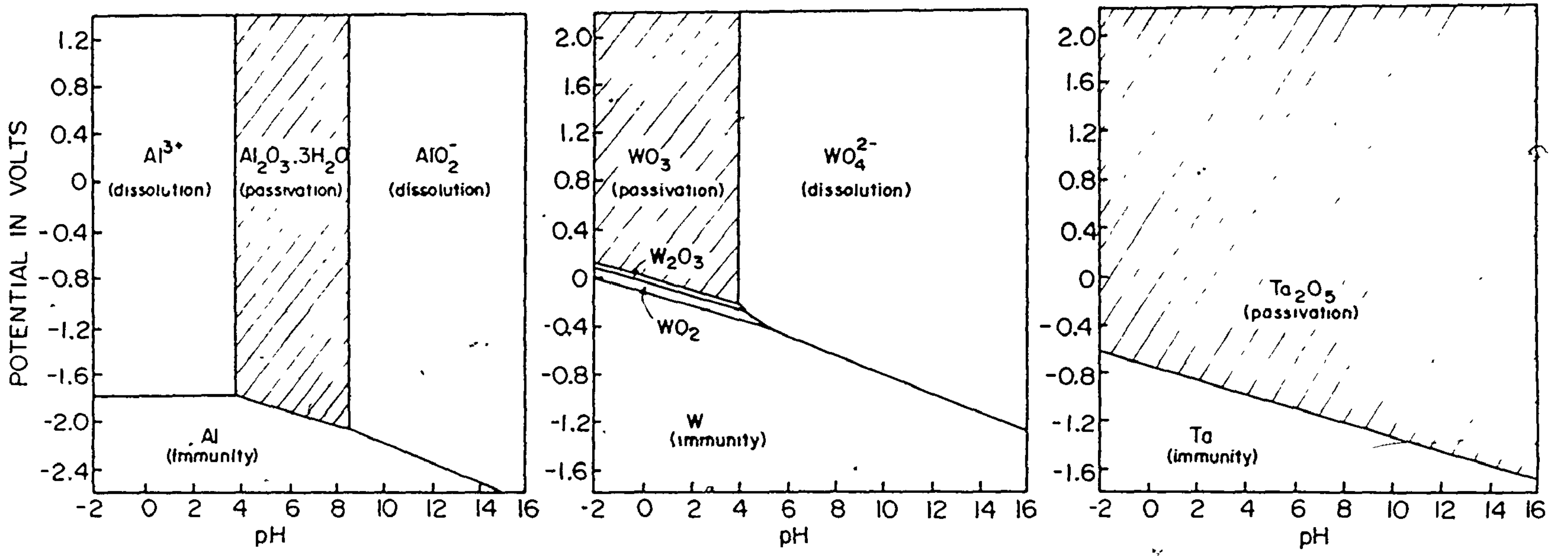

(a) (b) (c)

Fig. 2.2. Potential-pH diagrams for (a) Al, (b) W and (c) Ta at 25°C (simplified) after Pourbaix(18); hatched regions indicate the pH range of passivity.

2.3 Ionic Motion Under the Influence of a Field

As stated above, the dependence of the ionic current density on the field strength is observed, as a first approximation, to follow equation (2.1). Such dependence can arise if the field alters the energy barrier for the moving ion in the manner shown in Fig. 2.3, and if the flux in the direction opposed by the field is negligible. Mott and Cabrera(19,20) proposed that the energy barrier is between a cation site in the metal lattice and one in the metal/film interface. Verwey(21), on the other hand, supposed it to be that between two positions of minimum potential energy for the moving ion within the film substance. In other words, Mott and Cabrera assumed that the ion current is limited by the necessary polarization - in the electrochemical sense - of the actual anodic process $M^{2+}_{metal} \rightarrow M^{2+}_{film}$, whereas Verwey assumed that it is limited by the non-ohmic resistance of the solid oxide film. Fig. 2.4 illustrates the two assumptions schematically; the heights of the "interface" and "film" energy barriers are respectively designated W and U, with corresponding well-to-peak (half-width) distances b and a. The heights of either possible barrier (in the absence of field) are evidently at least 40 kT, because substantially no movement of matter occurs at ordinary temperatures by thermal agitation, i.e., the rate of non-electrolytic oxidation is vanishingly small. This follows by evaluating $\nu t\ \exp(-40)$ for t = 1 day.

The Mott-Cabrera model leads immediately by elementary rate theory to

$$i = \overrightarrow{i} - \overleftarrow{i} = nq\nu\left[\exp\left(\frac{-w+qbE}{kT}\right) - \exp\left(\frac{-w-qbE}{kT}\right)\right]$$

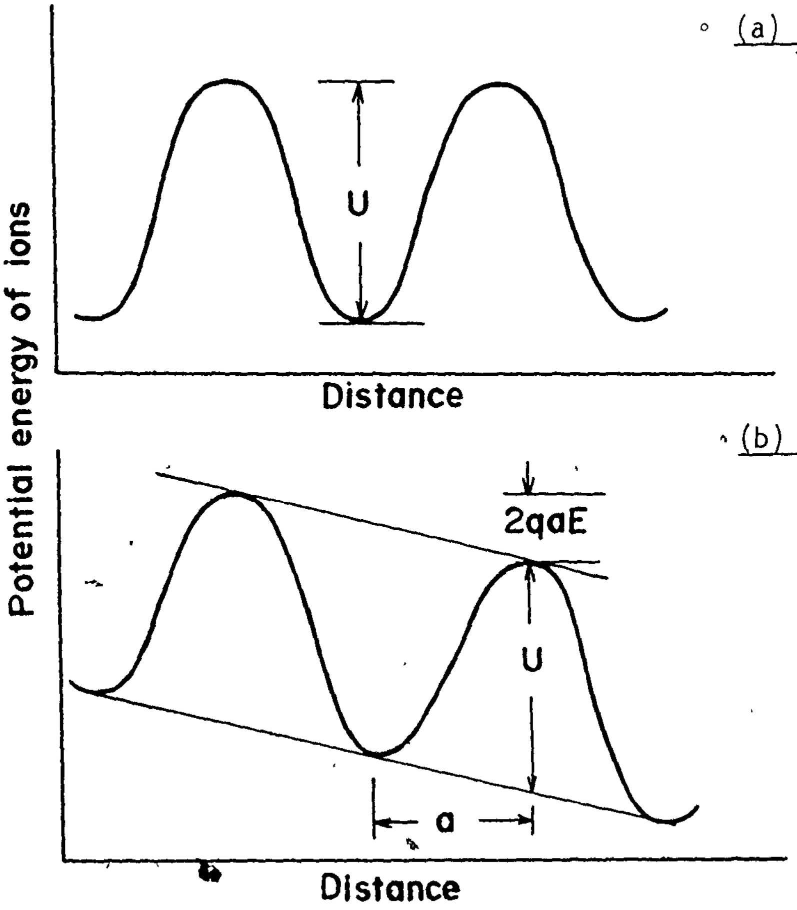

(a) Without Field

$$\overrightarrow{i} = \overleftarrow{i} = i_0$$

$$i_0 = nq\nu \exp(\frac{-U}{kT})$$

(b) With Field E

$$\overrightarrow{i} = nq\nu \exp[-(\frac{U-qaE}{kT})]$$

$$\overleftarrow{i} = nq\nu \exp[-(\frac{U+qaE}{kT})]$$

Fig. 2.3. Schematic energy - distance relationships with and without field.

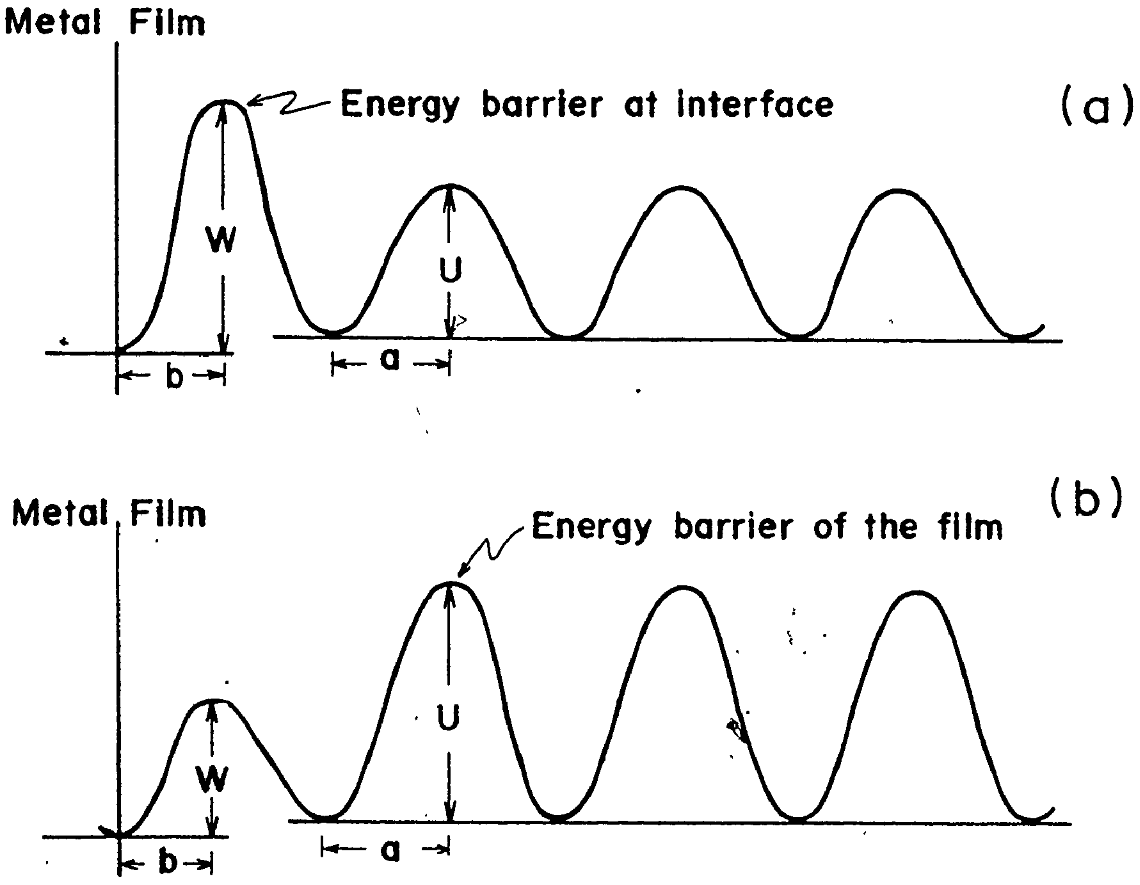

Fig. 2.4. Schematic energy–distance relationships for anodic-oxide film formation on metals. (a) Model of Mott-Cabrera (20) and (b) model of Verwey (21).

and at high enough fields, to

$$i \approx \vec{i} \approx nq\nu \exp\left(\frac{-w+qbE}{kT}\right) \qquad (2.5)$$

where n is the number of cations per cm^2 of metal surface able to undergo anodic transfer into the film, q their charge, and ν their vibration frequency. The parameters A and B of equation (2.1), above, are therefore given by:

$$A \doteq nq\nu \exp\left(\frac{-W}{kT}\right) \ ; \quad B = \frac{qb}{kT}$$

Analogously, Verwey's model leads, at high enough fields, to

$$i \approx \vec{i} \approx n' \, q\nu' \exp\left(\frac{-U}{kT}\right) \exp\left(\frac{aqE}{kT}\right) \qquad (2.6)$$

where n' is the number of mobile cations per cm^2 in each monolayer of the film and ν' is their vibration frequency. For this model the parameters A and B can be understood in terms of:

$$A = n' \, q\nu' \exp\left(\frac{-U}{kT}\right) \ ; \quad B = \frac{aq}{kT}$$

If we now introduce the self-diffusion coefficient, D, defined as

$$D = \frac{4a^2}{6} \nu \exp(-U/kT)$$

we can write relation (2.6) as:

$$i \approx \frac{3n'qD}{2a^2} \exp\left(\frac{qaE}{kT}\right) \qquad (2.7)$$

We will later (Sec. 7.3.2) use eq. (2.7) to estimate D.

Young(22) has made a generalized model with the above two as the limiting cases. The model leads to the same type of general expression as given by eq. (2.1), reduces to Mott's relation for small thicknesses, and reduces to Verwey's relation for large thicknesses. The field thus changes with thickness at first but eventually becomes constant at Verwey's value. However, Young suspected that the physical limitation that a film cannot be less than one unit cell thick may mean that the film may never be thin enough for Mott's model to be applicable to anodic oxidation.

Certain inadequacies of the above models have been noted:

(i) Work with Zr(23), for example, has shown that the parameters A and B are dependent on the thickness of the anodic film, although no such anomaly was found for films thicker than 10 nm on Ta, Nb, Bi, Ti, etc. Such an effect, Young thinks, may suggest that anodic films on Zr are inhomogeneous. We would add as an alternative that the effect may be related to the amorphous or crystalline nature of the films. As will be discussed in Ch. 7, films on Zr were found to be crystalline, whereas on most other metals were found to be amorphous except, in a few cases, for very small thicknesses.

(ii) All the above models ignored the amorphous nature of most anodic films, thence the possibility that distances and barriers were distributed.(24)

(iii) The possibility of a more complicated argument in equation 2.1:

$$i = A \exp(BE + B'E^2 + ...)$$

has been proposed(25,26) to overcome reported anomalies relating to the steady state anodic oxidation of Ta(25).

(iv) Other inadequacies may arise from the assumption that only the metal ions are mobile. On the contrary, the tracer work of Davies _et al._(27) (cf. Ch. 7), indicates that at least with Ta, Nb, Al and W both metal and oxygen ions are mobile and travel through the film. A new difficulty now arises in that the relative metal and oxygen ion mobilities would in general be expected to display a rapid change with the field unless there existed fortuitously close similarities between the activation energies and activation distances. The latter is quite unlikely to occur with more than one metal. This means that metal and oxygen movement are somehow coupled.(28)

Our stand in what follows will be to assume, without further discussion, Verwey's model or, equivalently, the large thickness limit of Young's model. Also, we will overlook the problems listed above as (i) to (iv).

In summary, the formation of anodic films is basically a process of ion transport in the presence of electric fields, since it occurs at ordinary temperatures under conditions when substantially no movement of matter occurs by thermal agitation only. The electric field can be said to reduce the energy barrier for the moving ions at such temperatures. However, the details of the transport process are rather complicated, since the transport is usually observed in amorphous films, which may in principal have a distribution of distances and barriers. Finally, we will assume that validity of eqs. 2.6 and 2.7 when necessary.

2.4 Structure of Anodic Films

Anodic-oxide films formed on metals are found to be of variable structure. They are formed either in the amorphous or the crystalline state depending on the material, on the film thickness, and on the various anodizing conditions, including the kind of electrolyte being employed and the anodizing temperature. In particular, the films formed on Hf(5), Sn(12), Zn(29) and Zr(30,31) are believed to be invariably crystalline, those on Ge(4) and Si(32) are believed to be invariably amorphous, while those on Al(33), Be (see Sections 3.3 and 3.5), Mo(6,34), Nb(34), Ta(33-36), Ti(31,33,34), V(14,34), W(31,33,34) and U(13,34) have been found to have a variable structure. If we regard amorphous films to be the norm in the last 9 cases, then crystalline films can be said to appear under certain conditions as follows:

high anodizing temperatures	Al, Nb, Ta and Ti
particular electrolytes	Be
small film thicknesses (< 10 V, i.e. < 30 nm)	Mo, Ta, V, W and U
large film thicknesses or long anodizing times	Al, Nb, Ta and Ti

Apart from empirical correlations as above, the question of why the various anodic films are amorphous or crystalline has not been answered yet. There is no previous rule which could be followed to determine the structure of anodic films, with the exception of the very recent attempt made by Arora and Kelly.(34) In this attempt, to be discussed in greater detail in Sec. 7.2.3, an analogy was proposed between the crystallization produced by the energy deposited by an impacting ion and that produced by a defect moving in an oxide under an electric field. If such analogy is valid, then based on the same criterion for the crystallinity of an ion bombarded solid (also to be discussed in Sec. 7.2.2), oxides can be classified as follows. Those oxides for which we have

$$\text{(crystallization temperature/melting temperature)} = T_c/T_m > 0.3$$

affect the rates at which they can be dissolved. For example, it has been noted for films on Nb and Ta, cf. Fig. 2.5 (7), that they have enhanced solubilities when formed in sulfate containing electrolytes, and this principle was successfully exploited in establishing anodic-sectioning techniques (7). In fact, it will be shown in Chapter 4, that the same principle can be exploited with Be and is regarded as one of the key points in establishing an anodic-sectioning procedure. The presence of the incorporated material and its distribution in depth will be investigated in more detail in Chapter 6, where some important conclusions will be reached about the mechanism of film growth.

The incorporation of electrolytic species into anodic films has been also inferred to affect the rate at which the films form, as embodied in the quantity $\frac{dV}{dt}$ for film growth at fixed current. This was first noted by Arora and Kelly$^{(7)}$ who observed factor of two greater values of $\frac{dV}{dt}$ for Nb and Ta when a sulfate electrolyte was used (Fig. 2.6). They interpreted the result as originating from film doping such that the dielectric constant, ε_r, was decreased , hence the value of V/x was increased. This interpretation assumes the validity of Dignam's anodizing theory (28) in which the field, E, in eq. (2.6) governing film formation, usually expressed as the Maxwell field (V/x), is replaced by the Lorentz field (VK/x), where K is a factor similar to $(1/3)(\varepsilon_r+2)$. This correlation with the doping of anodic films will be discussed in more detail for Be in Sec. 4.3.

Finally, doping leads to rather explicit effects when the weights of anodic films are considered, as in Sec. 4.4.2.

affect the rates at which they can be dissolved. For example, it has been noted for films on Nb and Ta, cf. Fig. 2.5 (7), that they have enhanced solubilities when formed in sulfate containing electrolytes, and this principle was successfully exploited in establishing anodic-sectioning techniques (7). In fact, it will be shown in Chapter 4, that the same principle can be exploited with Be and is regarded as one of the key points in establishing an anodic-sectioning procedure. The presence of the incorporated material and its distribution in depth will be investigated in more detail in Chapter 6, where some important conclusions will be reached about the mechanism of film growth.

The incorporation of electrolytic species into anodic films has been also inferred to affect the rate at which the films form, as embodied in the quantity $\frac{dV}{dt}$ for film growth at fixed current. This was first noted by Arora and Kelly$^{(7)}$ who observed factor of two greater values of $\frac{dV}{dt}$ for Nb and Ta when a sulfate electrolyte was used (Fig. 2.6). They interpreted the result as originating from film doping such that the dielectric constant, ε_r, was decreased , hence the value of V/x was increased. This interpretation assumes the validity of Dignam's anodizing theory (28) in which the field, E, in eq. (2.6) governing film formation, usually expressed as the Maxwell field (V/x), is replaced by the Lorentz field (VK/x), where K is a factor similar to $(1/3)(\varepsilon_r+2)$. This correlation with the doping of anodic films will be discussed in more detail for Be in Sec. 4.3.

Finally, doping leads to rather explicit effects when the weights of anodic films are considered, as in Sec. 4.4.2.

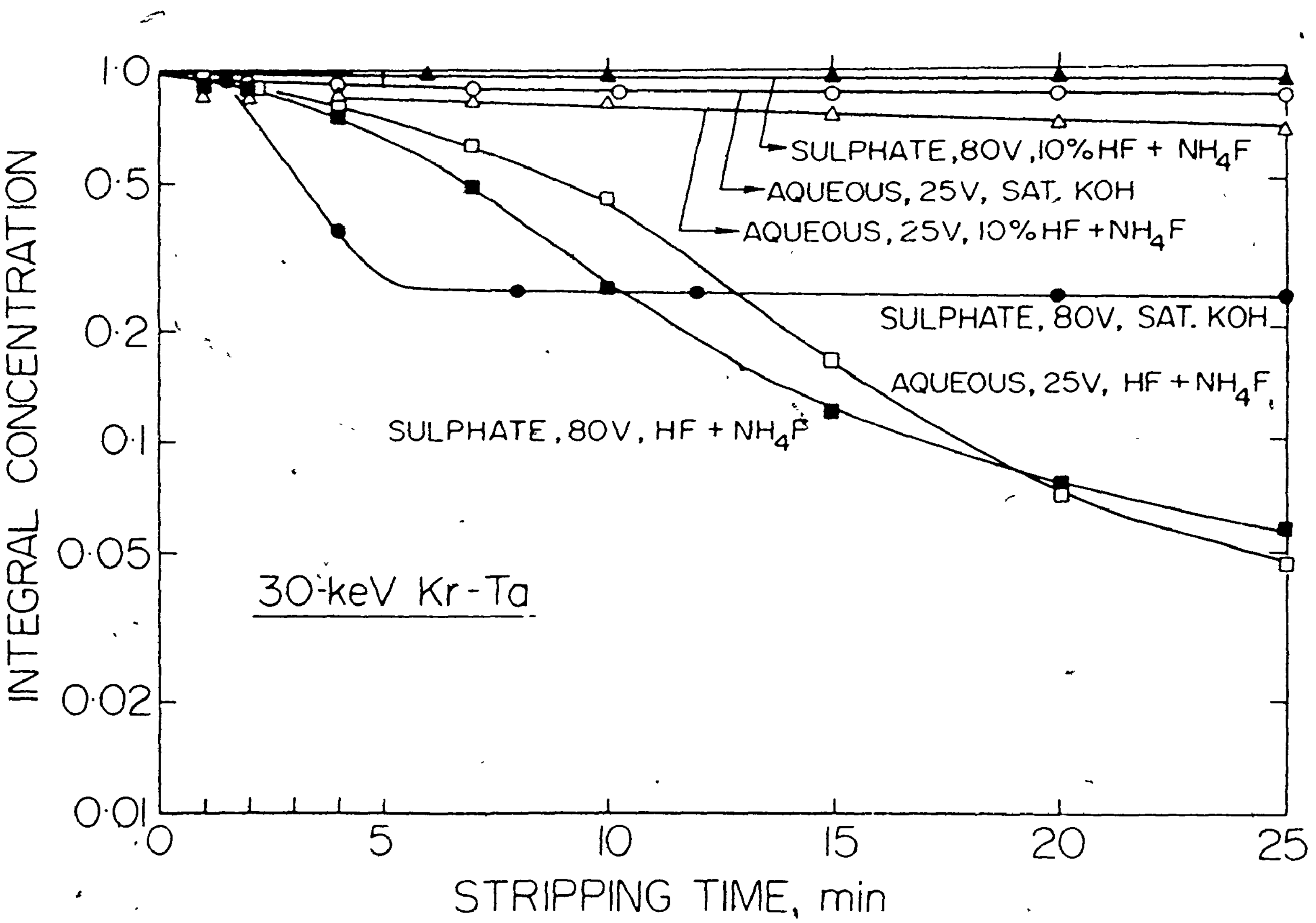

Fig. 2.5. Dissolution of anodic films on Nb as inferred by the loss of activity that was introduced prior to anodization as 5×10^{15} ions/cm^2 of 30-keV Kr^{85}. "Aqueous" refers to films formed in 0.2% KF while "sulfate" refers to films formed in an electrolyte consisting of a 1:3 mixture of H_2SO_4 and $(C_2H_5)_2SO_4$ (7).

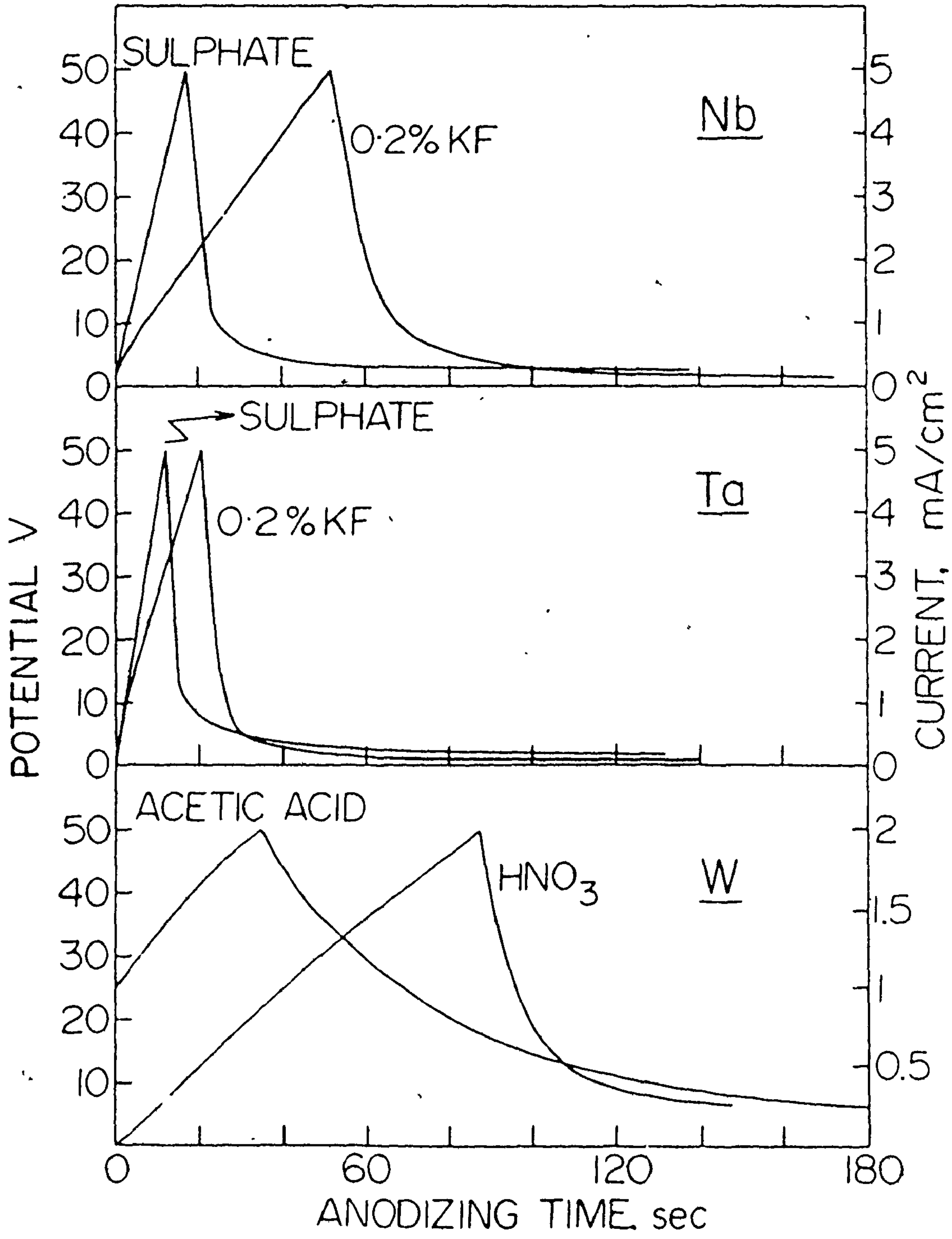

Fig. 2.6. Typical voltage-time and current-time curves for the anodization of Nb, Ta and W. Rising parts: voltage-time with voltages as in scale at left. Falling parts: current-time with current as in scale at right. The electrolytes are the same aqueous and non-aqueous ones of Fig. 2.5 (7).

2.6 Previous Work on Beryllium

Although much has been written on the anodic oxidation of metals, little has been published on the anodic behaviour of Be. The only experimental results of which the writer is aware of are those due to Kerr and Wilman(44), Levin(45), Heusler(3), Al'tovskii et al.(46) and Vol'fson et al.(47) In no case was typical valve-metal behaviour achieved.

In 1956, Kerr and Wilman(44) showed for the first time that anodic-oxide layers can be formed on Be in a mixture of nitric and chromic acid solutions and that they grow in thickness linearly with respect to time at constant current. They were unable to produce oxide films on Be by anodizing in nitric or sulphuric acid solutions and believed that both the oxide film and the metal substrate were being dissolved by the acid. They concluded that the formation of the oxide layer using the $CrO_3 + HNO_3$ mixture is likely also to be associated with partial dissolution of the oxide in such a way as to result in the BeO layer being porous, which could account for its continuous increase in thickness with time. The films formed in this case may therefore be similar to the anodic films formed on Al in dilute sulphuric acid, as mentioned before in Sec. 2.1.

Levin(45) found that films formed in $CrO_3 + HNO_3$ were invariably crystalline. On the other hand, with ethylene glycol containing ammonium borate, a non-aqueous electrolyte, the anodic film is amorphous. Levin attributed this difference in behaviour of Be in two types of electrolyte to the ability of the aqueous solutions to conduct high local current densities so as to initiate crystallization. He postulated that the surface temperature was in regions of high, local current density, above 300°C even for overall current densities as low as 0.5 mA/cm^2. The amorphousness of the films formed in ammoniated ethylene glycol was attributed to the absence of these large local current densities because of the high specific resistivity of this electrolyte. Levin's postulates have been questioned by Young(48) who showed that such a high temperature increase could not occur uniformly over the surface. Young rather preferred to assume specific electrolyte effects of unknown mechanism. We will show in Ch. 7 that Levin's description is probably wrong and, furthermore, that the "electrolyte effects" referred to by Young can be understood in terms of the incorporation of various anions from the electrolyte into the film so as to yield films that are doped. The film doping would, as we pointed out in Section 2.5, be reflected by an increase in the rate at which the film forms (higher $\frac{dV}{dt}$ value), so as to lead to the formation of an amorphous film, see Section 7.5.

Heusler(3) observed the growth of anodic-oxide layers on Be in a weakly alkaline aqueous solution of 0.5 M Na_2CO_3. The anodic behaviour of Be in this case was different from that found for acid solutions.(44,45) Thus, as seen in Fig. 2.7, when the current is initially applied the potential increases slightly and then remains constant for a time which depends on the current density used (e.g. 50 min for a current density of 5 mA/cm^2). As the current continues to flow an apparent transition from the active to the passive state occurs. Here an oxide layer is formed which is presumably insoluble or slightly soluble in the electrolyte. The oxide film then increases in thickness, as reflected by an increase in the potential, until it reaches the preset value where the current starts to drop down. Typical valve-metal behaviour is thus found following the transition. The thickness of the oxide was calculated from the measured field strength to be 3.2 nm/V. In addition, the as-formed oxide film was reported crystalline.

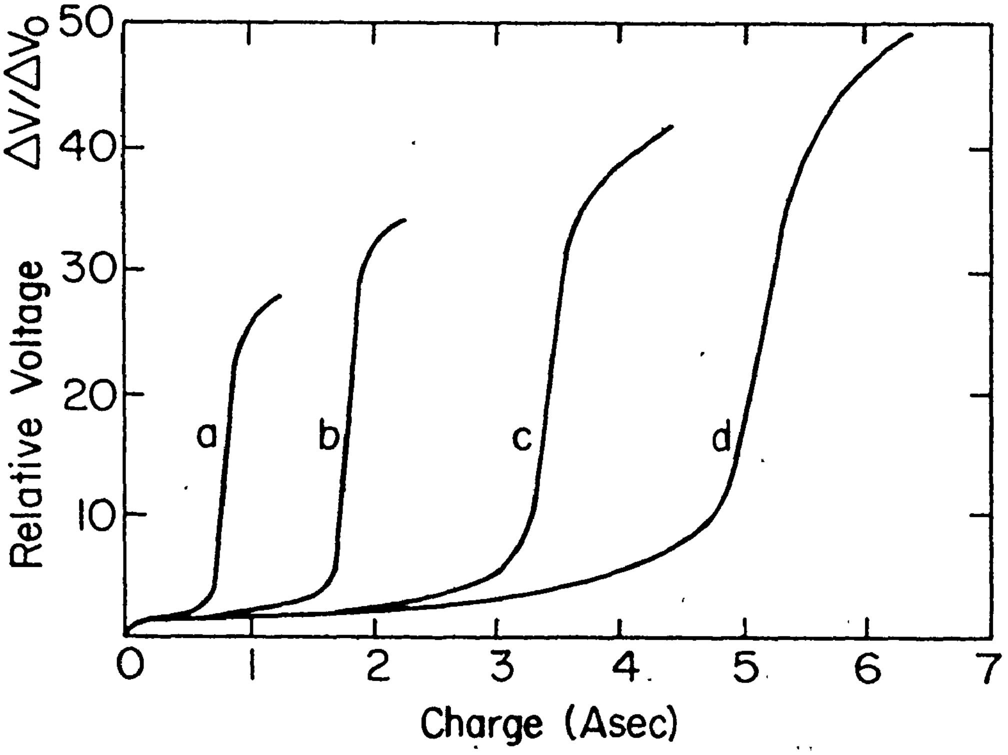

Fig. 2.7. Kinetics of anodic-oxide growth on beryllium in 0.5m K_2CO_3 solution (ref. 3). Area = 0.4 cm^2.

a = 30 mA, ΔV_o = 6.1 V

b = 10 mA, ΔV_o = 5.1 V

c = 5 mA, ΔV_o = 4.8 V

d = 2 mA, ΔV_o = 3.8 V

Al'tovsky et al.(46) and Vol'fson et al.(47) have studied the formation of anodic layers formed on Be in a 20% CrO_3 aqueous electrolyte. At the start of anodization, they reported a voltage rise (at constant current of 100 mA/cm^2) of 3-6 volts after which the current density fell. However, they reported a film thickness of 30 μm that they associated with the initial formation of a non-porous barrier layer on which the porous anodic film grows. The film formed in this case is therefore similar to that studied by Kerr and Wilman(44).

In summary, the previous experimental results showed that the anodization of Be yielded films that are characterized by one or more of being porous, being subject to extensive dissolution, or being crystalline. In the following chapter we will describe conditions under which Be will form anodic films that are, unlike those of previous work, found simultaneously to be non-porous, formed with minimal or no dissolution, and amorphous. The formation of such films will lead first to the microsectioning of Be as will be shown in Chapter 4. It will lead secondly to the possibility of studying secondary particle emission from BeO as in Chapter 6, hence to establish the mechanism of film formation. It will lead thirdly, and perhaps most important, to setting up principles according to which the anodic oxidation as well as anodic sectioning of unstudied systems should be approached. An explicit case for the former is Fe, the results for which were obtained mostly by DiDonato(49), and are only summarized in this thesis. It was found readily possible here to grow protective films on Fe with voltages in excess of 100 V. An explicit case for the latter is the anodic sectioning of Zr. It was found that the stripping of the oxide film is the main problem, since it cannot be aided either by doping the anodic film, Sec. 6.4, or by inducing the film to form in the amorphous state, Section 7.4.

REFERENCES TO CHAPTER 2

1. P. Jespersgard and J.A. Davies, Can. J. Phys., 45 (1967) 2983.
2. J. Siejka, J.P. Nadai and G. Amsel, J. Electrochem. Soc., 118 (1971) 727.
3. K.E. Heusler, Ber. Bunsengesellschaft, 67 (1963) 943.
4. S. Zwerdling and S. Sheff, J. Electrochem. Soc., 107 (1960) 338.
5. M.T. Thomas, ibid., 117 (1970) 396.
6. M.R. Arora and R. Kelly, ibid., 119 (1972) 270.
7. M.R. Arora and R. Kelly, Electrochim. Acta, 19 (1974) 413.
8. N.Q. Lam and R. Kelly, Can. J. Phys., 48 (1970) 137.
9. R.E. Pawel, Rev. Sci. Instr., 35 (1964) 1066.
10. W. Mizushima, J. Electrochem. Soc., 108 (1961) 825.
11. E.F. Duffek, E.A. Benjamini and C. Mylroie, Electrochem. Technol., 3 (1965) 75.
12. E. Giani and R. Kelly, J. Electrochem. Soc., 121 (1974) 394.
13. O. Flint, J.J. Polling and A. Charlesby, Acta Met., 2 (1954) 696.
14. M.R. Arora and R. Kelly, J. Electrochem. Soc., 120 (1973) 128.
15. A. Charlesby, Acta Met., 1 (1953) 340.
16. J.J. Polling and A. Charlesby, Proc. Phys. Soc., 67B (1954) 201.
17. R.D. Misch, Acta Met., 5 (1957) 179.
18. M Pourbaix, Atlas of Electrochemical Equilibria, Pergamon Press (1966).
19. N.F. Mott, Trans. Faraday Soc., 43 (1947) 429.
20. N. Cabrera and N.F. Mott, Repts. Prog. Physics, 12 (1948-49) 163.
21. E.J.W. Verwey, Physica, 2 (1935) 1059.
22. L. Young, Can. J. Chem., 37 (1959) 276.

23. L. Young, Trans. Faraday Soc., 55 (1959) 632.

24. L. Young, Proc. Roy. Soc., A258 (1960) 465.

25. L. Young, ibid., A258 (1960) 496.

26. M.J. Dignam, Can. J. Chem., 42 (1964) 1155.

27. J.A. Davies, B. Domeij, J.P.S. Pringle and F. Brown, J. Electrochem. Soc., 112 (1965) 675.

28. M.J. Dignam, ibid., 112 (1965) 729.

29. S.M. El-Raghy (University of Cairo), personal communication (1975).

30. P.H.G. Draper and J. Harvey, Acta Met., 11 (1963) 873.

31. D.G. Brandon, J. Zahavi, A. Aladjem and J. Yahalom, J. Vac. Sci. Technol., 6 (1969) 783.

32. M.A. Wilkins, Harwell (U.K.) Report AERE-R5875 (1968).

33. R.A. Harrington and H.R. Nelson, AIMME Inst. Metal, 137 (1940) 62.

34. M.R. Arora and R. Kelly, J. Materials Science, 12 (1977) 1673.

35. R. Kelly and N.Q. Lam, Rad. Effects, 19 (1973) 39.

36. D.A. Vermilyea, J. Electrochem. Soc., 102 (1955) 207.

37. J.J. Randall and W.J. Bernard, Electrochim. Acta, 20 (1975) 1359.

38. C.J. Good, M.Sc. thesis, McMaster University (1976).

39. J.J. Randall, A.J. Bernard and R.R. Wilkinson, Electrochim. Acta, 10 (1965) 183.

40. D.A. Vermilyea, Acta Met., 2 (1954) 482.

41. P.H.G. Draper, ibid., 11 (1963) 1061.

42. D.M. Smyth, T.B. Tripp and G.A. Shirn, J. Electrochem. Soc., 113 (1966) 100.

43. G. Amsel, C. Cherki, G. Feuillade and J.P. Nadai, J. Phys. Chem. Solids, 30 (1969) 2117.

44. I.S. Kerr and H. Wilman, J. Inst. Metals, 84 (1955-56) 379.

45. M.L. Levin, Trans. Faraday Soc., 54 (1958) 935.

46. R.M. Al'tovskii, A.G. Fedotova, M.I. Urazbev and S.I. Korolven, Prot. Metals, 5 (1969) 172.

47. A.I. Vol'fson, N.E. Markova, V.V. Chernyshev, V.N. Lebedev and V.V. Vavakin, ibid., 9 (1973) 321.

48. L. Young, Anodic Oxide Films, Academic Press (1961) 222.

49. C. DiDonato and R. Kelly, unpublished work, McMaster University (1978).

CHAPTER 3

FORMATION AND STRUCTURE OF ANODIC FILMS ON BERYLLIUM

3.1 Introduction

Anodic films on metals are often classified as porous or non-porous. Non-porous films, sometimes termed "barrier films", are normally found to form in electrolytes in which the oxide has a low solubility, and to grow until they reach an almost limiting thickness which, for a given time scale, is proportional to the applied potential. They are characterized by a high resistivity and by conduction which is mainly ionic in character. Non-porous films are often amorphous though there are many exceptions, including Hf, Sn, Zn and Zr in general and Al, Mo, Nb, Ta, Ti, U, V, and W under particular conditions as mentioned in Section 2.4.

On the other hand, electrolytes in which the oxide is somewhat soluble are occasionally found to support the growth of porous films which increase more or less indefinitely in thickness while the applied potential varies slightly or not at all. They are characterized by a low resistivity. Though normally described as "crystalline", they are variously amorphous (Al anodized at room temperature) or crystalline (Be, probably Sn).

Films formed on Be have invariably been found to show one or more of the characteristics of a porous film. Thus no films at all were obtained with some dilute aqueous electrolytes (1,2). Those formed with HNO_3, CrO_3, or mixed CrO_3-HNO_3 electrolytes were crystalline (1,2) and had thicknesses up to ∿ 400 nm (1) or more (3). Those formed with ammonia in ethylene glycol appeared to have had a low resistivity and to have been subject to dissolution (1,2), while use of 0.5 m Na_2CO_3 resulted in crystalline films (4).

The object of this chapter is to describe experiments concerning the formation of anodic films on Be which, unlike those of previous work, are simultaneously non-porous, formed with minimal or no dissolution, and amorphous. This goal was achieved, such that films could be formed under conditions when the potential drop across the film was about 15×10^8 V/m and the efficiency at constant current was 0.95 ± 0.02. Beryllium can thus be made to anodize in a similar manner as with most other metals (Table 3.1). The formation of such films is in principle of importance in the understanding of anodic oxidation from an electrochemical point of view, but we regard it of greater interest to work on diffusion and on ion-solid collisions. It leads first of all to a microsectioning technique, thence to the possibility of studying diffusion and ion depth distributions in Be. The details on microsectioning Be, which is the lightest target that can be conveniently bombarded, will be given in Chapter 4. It leads secondly to the possibility of studying secondary-particle emission from BeO and the possibility of correlating the depth profiles of incorporated anions with the mechanism of film formation. This will be discussed in detail in Chapter 6.

TABLE 3.1. Comparison of fields and efficiencies for anodizing various metals.

Metal	Electrolyte	Field to form a 50-V film (10^8V/m)	Efficiency at constant current of 2 or 3 mA/cm^2	Ref.
V	mainly acetic acid	2.8	0.95	7,9
Mo	mainly acetic acid	2.9	0.95	6,9
Nb	aqueous	3.4	∿ 1.0[a]	5,10
Zr	aqueous	4-6 (sic)	0.50	11
W	mainly acetic acid	4.6	0.96	5,9
Ta	aqueous	6.2-6.6	0.99	8
Al	aqueous	8.7-9.1	0.90	8
Be	ethylene glycol + Na_2HPO_4 + Na_2SO_4	15	0.95	here, Section 2.5

---

[a] Not for constant current

From a different point of view, we regard the anodizing of Be as a "test case" to demonstrate the feasability of forming anodic films on arbitrary metals. Our approach will be seen to be highly empirical yet successful, and we will terminate the chapter with a brief discussion of how this approach succeeded with the technologically most important metal of all. This is Fe, which, using the ideas developed here, can be anodized at up to ∿ 150 V (12) resulting in the formation of a thick, amorphous, and nearly protective oxide. This oxide, when crystallized, yields the diffraction pattern of γ-Fe_2O_3. However, it suffers one practical drawback: it tends to be cracked and badly adherent.

3.2 Experimental

The Be specimens used throughout this work were polycrystalline foils with dimensions of approximately 25 x 12.5 x 0.25 mm and with purities claimed to be 99.5%. They were obtained from Ventron Corp. (Alpha Products). After an initial polishing with a series of increasingly fine SiC papers, the specimens were given further treatment consisting either of chemical polishing (in 5 wt% sulphuric acid, 75 wt% phosphoric acid, 7 wt% chromic acid, and 13 wt% water) or else of mechanical polishing using 6 μm and 1 μm diamond paste with kerosene as a lubricant. For experiments where reproducible flat surfaces were required, the specimens were finally anodized and sectioned 5 times. The anodizings were carried out at 50 V in ethylene glycol which is saturated in both Na_2HPO_4 and Na_2SO_4 and will be subsequently called "electrolyte A". The sectionings were accomplished by exposing the film to 10% KOH for two minutes. Such treatment may be assumed to remove submicroscopic irregularities.

All anodizings were performed at room temperature (∿ 22°C) using a power supply such that limits to both the current and potential could be preset (Hewlett-Packard Model 6186B). With such a power supply an automatic transition from constant current to constant potential is obtained when the preset potential has been reached. The cathode was made of platinum gauze in the form of a cylinder with an inside diameter of 25 mm. Potentials refer to the total value from anode to cathode rather than to the value across the oxide film. The anodizings were carried out in unstirred electrolytes and without protection from air, and the electrolytes were therefore discarded after 5 or 6 anodizings or one hour, whichever came first.

The extent of metal dissolution during anodizing was determined using a depth-distribution technique due to Giani (13). ^{85}Kr, which is beta-active, was implanted in Be at 30 keV to a dose of 2×10^{15} ions/cm^2 and the activity was noted before and after anodizing. The experimental depth distribution of such implant is shown in Fig. 4.4 and enabled the retained activity fraction to be expressed as a depth. Such a depth is a lower limit to the metal loss during anodizing, the lower-limit aspect entering due to the film forming mainly by outward migration of Be, as will be discussed in Chapter 6, thence to a burying of the marker in the manner shown by Pringle (14) for Ta.

The structure of the anodic oxide film was determined by two means, electron microscopy and gas release. For the microscopy, a Philips EM 300 was used with the reflection-diffraction stage. Gas-release measurements were carried out using a conventional gas-release arrangement (cf. ref. 15), where a stream of He flowing at a constant rate is passed over the sample and through a β-counting chamber, while the sample is heated linearly at 25 K/min. The counter and the thermocouple were connected to a two-channel recorder so that the rate of gas release ($\frac{dF}{dt}$, where F is the fractional gas release) and the temperature of the specimen were recorded simultaneously. This differential gas-release system was calibrated using Sn and Al bombarded at high doses, where narrow release peaks appear at the melting temperatures. The calibrations showed the apparent temperatures, as recorded in the gas-release spectra, to be too high by 45 ± 5°C and all figures to follow were drawn taking this into account. The temperature difference is due to the time lag for the carrier gas to reach and pass through the counting chamber.

3.3 Results of Be Anodization in Various Electrolytes

In this section we survey the various types of electrolytes, seeking those which permit the formation of barrier films on Be showing minimal or no dissolution and having an amorphous structure. The barrier-type films will be shown to have the expected voltage dependent limiting thickness which in turn permits the precise control of the thickness by controlling the formation voltage. At the same time, forming the films with negligible dissolution in the electrolyte is a prerequisite for the removal of uniform controlled sections of the metal. The amorphous nature of the films, as well as their doping (to be discussed later in Section 4.3 and 6.4), aids the successful stripping of such oxide layers by chemical etching. In other words, amorphous doped films tend to dissolve at a much higher rate than their crystalline metal substrates. For Be we investigated the following categories of electrolytes:

(1) Strong oxidizing electrolytes:

CrO_3-HNO_3 mixture

(2) Dilute aqueous electrolytes:

acidic: 1% H_2SO_4, 1% HNO_3,

basic: 1% KOH, 0.5 M Na_2CO_3

(3) Non-aqueous electrolytes:

acidic: 0.02 M $Na_2B_4O_7 \cdot 10\ H_2O$ in acetic acid (borate doping)

$(C_2H_5)_2SO_4$-H_2SO_4 3:1 mixture (sulphate doping)

$(C_2H_5)_2HPO_4$ (phosphate doping)

neutral: ethylene glycol containing

Na_2CO_3	(no doping expected)
Na_2SO_4 and/or Na_2HPO_4	(sulphate and/or phosphate doping)
$Na_2B_4O_7$	(borate doping)

With each of the above electrolytes we studied the voltage-time (V-t) and current-time (I-t) behaviour, since the formation of a barrier type film is normally reflected by a rapidly rising V-t curve followed by a falling I-t curve; cf. Fig. 3.1 (curve B) for anodizing Be in aqueous 0.5 M Na_2CO_3. The voltage continues to rise, in such cases, to maintain the field across the thickening oxide film until it reaches a preset value. Then the current drops rapidly due to the decreasing value of the field across the slowly thickening oxide film until the current reaches a very small value. Although not strictly correct, the film can then be said to have a limiting thickness. In contrast, such characteristics are not obtained in case of the formation of a porous film. For example, when anodizing Be in the CrO_3-HNO_3 electrolyte (curve A of Fig. 3.1) there is neither a voltage rise nor a falling current, and the resulting films (Fig. 3.2) are clearly porous. In curve C of Fig. 3.1, for anodizing Be in diethyl phosphate, we observe a voltage rise but the current stays roughly constant. Such a case can be interpreted in terms either of the initial formation of a barrier film followed by a porous layer or of a barrier film which dissolves significantly. The results for V-t and I-t behaviour together with the pH, the predicted behaviour from the thermodynamic data, and the extent of dissolution determined in each of the above electrolytes are all summarized in Table 3.2.

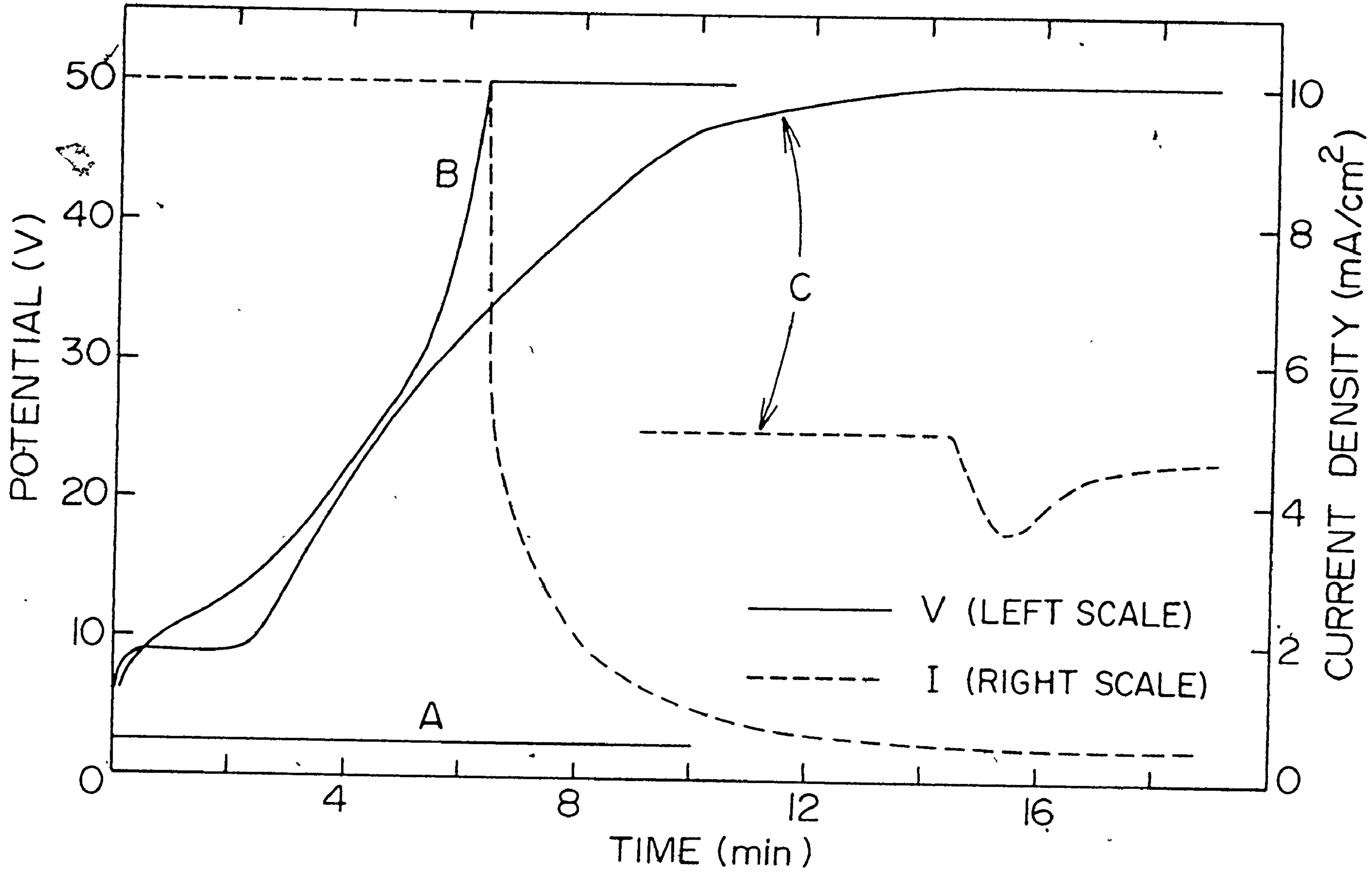

Fig. 3.1. Typical voltage-time and current-time curves for the anodization of Be in the CrO_3- HNO_3 electrolyte (curve A, always 30 mA/cm^2), 0.5 m Na_2CO_3 (curve B), and $(C_2H_5)_2HPO_4$ (curve C). Solid lines: V-t, with potential as in scale at left. Dashed lines: I-t, with current as in scale at right.

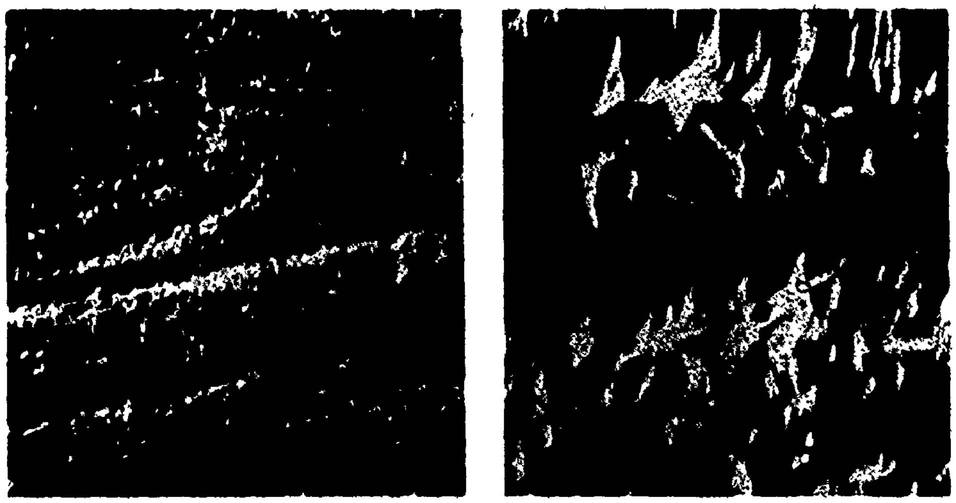

Fig. 3.2 Scanning electron micrographs with different magnifications of film formed by anodizing Be in the CrO_3-HNO_3 electrolyte for 2 min at 30 mA/cm^2. The films are markedly porous, the scale of the porosity being 100-1000 nm.

Fig. 3.3 Reflection electron diffraction patterns taken at 80 kV of film formed by anodizing Be in the CrO_3-HNO_3 electrolyte for 2 min at 30 mA/cm^2. Image a: as-formed film, showing diffuse rings characteristic of a fine-grained, untextured polycrystalline structure. Image b: film heated in a vacuum of 1×10^{-4} Pa at 600°C and showing sharpened rings identifiable as hexagonal BeO.

TABLE 3.2 V-t, I-t behaviour, pH, and dissolution for the anodization of Be (preset potential 50 V)

Electrolyte	pH	Prediction from Pourbaix diagram (Fig. 2.1)	Final potential (volts)	Time to reach preset potential 50 V (min)	Initial current (mA/cm^2)	Final current (mA/cm^2)	Total anodizing time (min)	Fraction of Kr implant which is retained	Inferred loss of Be$^{(*)}$ (nm)
(1) Strong oxidizing:									
CrO_3-HNO_3 mixture	2	Be^{2+}	∼ 3	never	30	30	2	0.19 ± 0.5	$\gtrsim 40$
(2) Dilute aqueous:									
1% H_2SO_4	1	Be^{2+}	∼ 0	never	20	20	5	< 0.003	$\gtrsim 120$
1% HNO_3	2	Be^{2+}	∼ 3	never	20	20	5	0.15 ± 0.01	$\gtrsim 50$
1% KOH**	12	$Be_2O_3^{2-}$	30	4**	20	3	10	0.07 ± 0.02	$\gtrsim 60$
0.5M Na_2CO_3	11	$Be_2O_3^{2-}$	50	6	10	0.4	15	$0.13 \pm .03$	$\gtrsim 50$
(3) Non-aqueous:									
mainly acetic acid	4	$Be(OH)_2$	50	0.5	10	1	15	$0.06 \pm .01$	$\gtrsim 60$
$(C_2H_5)_2SO_4$-H_2SO_4 (mixture)	1	Be^{2+}	50	0.3	20	∼ 20	10	< 0.01	$\gtrsim 90$
$(C_2H_5)_2HPO_4$	5	$Be(OH)_2$	50	14.5	5	4.5	20	< 0.01	$\gtrsim 90$
E.G. + Na_2CO_3**	10	$Be(OH)_2$	30	1.6**	2	0.3	4	0.88 ± 0.04	$\gtrsim 5$
E.G. + $Na_2B_4O_7$	6	$Be(OH)_2$	50	0.8	3	0.2	4	0.92 ± 0.04	$\gtrsim 4$
E.G. + Na_2SO_4	6	$Be(OH)_2$	50	1.5	3	0.3	4	0.73 ± 0.04	$\gtrsim 11$
E.G. + Na_2HPO_4	8.5	$Be(OH)_2$	50	0.25	3	0.1	2	$0.994 \pm .008$	$\sim >$ 0
"electrolyte A"	7.5	$Be(OH)_2$	50	0.3	3	0.1	2	$0.986 \pm .006$	$\sim >$ 0

---

* deduced from the preceding column with the help of Fig. 4,4.

** preset potential 30 V.

In the following subsections we will discuss in greater detail the results of the anodization behaviour of Be in each of the above categories of electrolyte.

3.3.1 Strong Oxidizing Electrolytes

The Pourbaix diagram (Fig. 2.1, p. 9) suggests unambiguously that a CrO_3-HNO_3 mixture with pH 2 will lead to dissolution rather than film formation with Be. In essential agreement, porous films are found and dissolution losses are very high.

The CrO_3-HNO_3 mixture consisting of 200 g/l of CrO_3 in 10% HNO_3 is known to yield films with Be such that the films grow in thickness linearly with time while the current remains constant (1,2). Thicknesses of up to ∿ 400 nm were obtained in refs. 1 and 2 and the films showed brilliant, though non-uniform, interference colours. While the films were crystalline, they had significantly broadened rings in their diffraction patterns. Anodic films have also been obtained using as electrolyte 20% aqueous CrO_3 (3,15). The results were interpreted in terms of the initial formation of a non-porous layer of small but constant thickness followed by a thick film which could be shown to be porous. For example, a formation potential of 3-6 V gave a limiting film thickness of 30,000 nm in 4 h.

We have undertaken a limited number of additional experiments using the CrO_3-HNO_3 electrolyte of ref. (1,2). The V-t behaviour, as shown in curve A of Fig. 3.1 and also in Table 3.2, suggests (though does not prove) that thick, porous films are formed. The extent of porosity was investigated explicitly by means of scanning electron microscopy. The results, given in Fig. 3.2, show clearly the porous nature of the films, the scale of the porosity being 100-1000 nm. The extent of metal dissolution during anodizing was determined by the depth-distribution technique and found to be significant (Table 3.2).

Structural information was sought using reflection electron diffraction. Results for an as-formed film are shown in Fig. 3.3. The rings are somewhat diffuse, though are nevertheless clearly identifiable as rings rather than halos. This broadening is probably the result of the grain size being very small (> ∿ 5.0 nm). Other specimens were heated in a vacuum of 1×10^{-4} Pa at 600°C to encourage grain growth, thence a sharpening of the diffraction rings (Fig. 3.3b). The resulting pattern is compared in Table 3.3 with those of hexagonal and tetragonal (16) BeO. We regard an identification with hexagonal BeO as preferable. As a final step, a visual comparison of Figs. 3.3a and 3.3b can be made. As can be seen, there is good reason to believe that the as-formed films are the same as those heated at 600°C and therefore also consist of hexagonal BeO. Be in this respect resembles Mo (thin films only (17)), Sn (13), and U (18), where the as-formed anodic films consist of crystalline oxides in their normal modifications. It differs from Hf (19), Ta (thin films only (17)), Ti (20), V (thin films only (17)), and Zr (21,22), where unexpected phases appear.

In conclusion, the anodic films formed on Be with the CrO_3-HNO_3 electrolyte have none of the properties which were desired regarding porosity, dissolution, and structure.

TABLE 3.3 Diffraction analysis of anodic film formed on Be using the CrO_3-HNO_3 electrolyte

Observed spacings	Spacings for hexagonal BeO[a]	Spacings for tetragonal BeO[b]
(Å)	(Å)	(Å)
...	...	3.35
2.34	2.34	2.38
2.17	2.19	2.13
2.02	2.06	...
1.60	1.60	1.68
1.45	1.35	1.50
...	...	1.37
1.26	1.24	1.32
1.17	1.17	1.19
...	1.15	1.15
...	1.13	1.12
...	1.10[c]	...
1.05	1.03	1.06
...	0.99[c]	...

---

[a] ASTM 4-0843

[b] ASTM 20-164

[c] < 1% relative intensity

3.3.2 Dilute Aqueous Electrolytes

The Pourbaix diagram (Fig. 2.1, p. 9) suggests that acidic solutions will lead to dissolution rather than film formation and this is observed. Basic aqueous solutions with pH 11-12 are near a boundary and we therefore anticipate either a film with dissolution or dissolution alone; in fact, it is the former that occurs. Neutral aqueous solutions would in principle lead to film formation, though have not been discussed in previous work nor were they considered here. Rather the main effort here will be given to neutral non-aqueous solutions (Section 3.3.3).

For the acidic aqueous electrolytes it was concluded by Levin (2) that no film at all is formed on Be in 1% H_2SO_4, though 1% HNO_3 led to crystalline BeO if the current density was high enough. Survey experiments undertaken in the course of this work have largely confirmed these results. This follows from the V-t and I-t behaviour (Table 3.2). In addition, we have sought to obtain additional information on the use of these electrolytes employing the depth distribution technique. Unacceptable extents of metal dissolution during anodizing were revealed (Table 3.2).

Concerning basic aqueous electrolytes with Be, Levin (2) have concluded that no film is formed in 1% KOH with pH 12, but Heusler (4) was able to form films in an electrolyte containing 0.5 m Na_2CO_3 with pH 11. The films were crystalline, could be formed up to a thickness of ∿ 250 nm (at 200 V), and were accompanied by oxygen evolution.

We have sought to obtain additional information about the use of both 1% KOH and 0.5 m Na_2CO_3 solutions with Be. Films were found to form with V-t and I-t behaviour (shown in Table 3.2 for both and in curve b of Fig. 3.1 for Na_2CO_3) that suggests, though does not prove, that non-porous films result. The extent of porosity was again investigated by scanning electron microscopy. The results, given in Fig. 3.4 for the 0.5 m Na_2CO_3 case, show that the films are mainly non-porous, but with evidence for both local and general dissolution. The metal dissolution during anodizing, determined by the depth-distribution technique, occurred to a significant extent (Table 3.2), which is in agreement with the Pourbaix diagram. Therefore, the use of the above basic electrolytes, pH 11-12, for anodizing Be is unsatisfactory in the present context because of the significant dissolution. Porosity, on the other hand, is not a problem.

3.3.3 Non-aqueous Electrolytes

The Pourbaix diagram leads to similar predictions for both aqueous and non-aqueous solutions, principally that films will be formed and dissolution be minimal for pH 4-10.5. The observed results were in good agreement, such that stable films appeared for pH 6-10. Apart from considerations of pH, however, it emerges that doping, i.e. incorporation of electrolyte components into the anodic film, also plays a role.

An indication that non-aqueous electrolytes may be of interest with Be is found in work by Kerr and Wilman (1). They established, using a 25 g/l solution of ammonia in ethylene glycol, that 30 nm thick amorphous films could be formed. Unfortunately, the current remained roughly constant, as if the films were not insulating or alternatively were dissolving. Presumably they had exceeded the critical pH 10.5 suggested by the Pourbaix diagram.

Non-aqueous electrolytes have been used successfully in our laboratory in the last few years to develop anodic sectioning techniques for Mo (6), V (7), Nb, Ta and W (5) and the following was concluded. Those electrolytes based on acetic acid probably lead to minimal doping

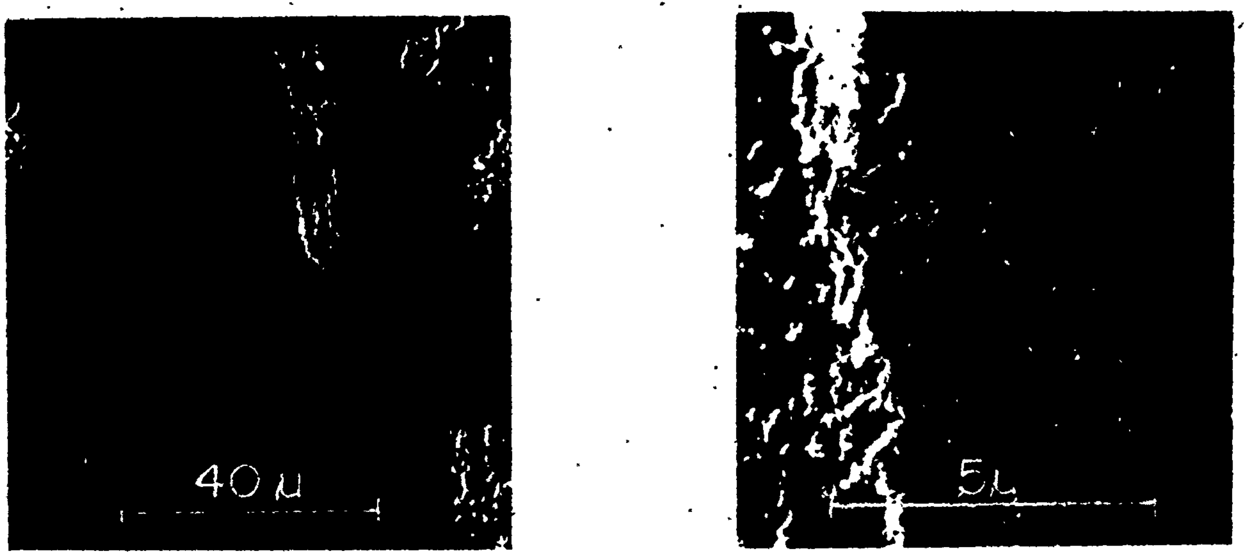

Fig. 3.4 Scanning electron micrographs with different magnifications of film formed by anodizing Be in 0.5 m Na_2CO_3 for 15 min with a preset current of 10 mA/cm^2 and a preset potential of 50 V. The films are mainly non-porous, though show features suggestive of both local and general dissolution.

of the anodic films, and are useful when the film is chemically unstable. Those based on the $(C_2H_5)_2SO_4$-H_2SO_4 are useful when heavy sulphate doping is desired, while those based on the system $(C_2H_5)_2HPO_4$ are useful when heavy phosphate doping is needed. In fact, doping of anodic films by anions incorporated from the electrolyte has played a great role in establishing anodic sectioning techniques as mentioned above. Such doping effects are beyond the scope of this chapter, though will be investigated more explicitly in Chapters 4 and 6.

In the present work we have investigated the anodization behaviour of Be in the above non-aqueous acidic electrolytes in addition to neutral electrolytes based on ethylene glycol. The results were as follows:

(i) Acetic acid. An acetic-acid based electrolyte, consisting of acetic acid, $Na_2B_4O_7 \cdot 10H_2O$, and water, is one of the few which permits Mo (6) and V (7,23) to be anodized. Its use with Be appeared at first sight encouraging in view of the V-t and I-t behaviour (Table 3.2); however, in agreement with the pH being 4, unacceptable metal dissolution occurs (Table 3.2).

(ii) $(C_2H_5)_2SO_4$-H_2SO_4. A mixture of 75% $(C_2H_5)_2SO_4$ and 25% H_2SO_4 has been successfully used in the anodic sectioning of Nb and Ta (5). Anodizing Be in this electrolyte results in V-t and I-t curves of non-ideal type (Table 3.2). The electrolyte is implied by this to be unsatisfactory and this conclusion was confirmed by finding similar metal dissolution to occur during anodizing as with diethyl phosphate (Table 3.2).

(iii) <u>$(C_2H_5)_2HPO_4$</u>. Anodizing Be in diethyl phosphate results in a V-t curve suggestive of a barrier film but an I-t curve leading to the converse conclusion (curve <u>c</u> of Fig. 3.1 and also Table 3.2). To gain further information, the extent of metal dissolution during anodizing was determined and found to be unacceptably high (Table 3.2).

(iv) <u>Ethylene glycol</u>. More satisfactory results were obtained with ethylene glycol which has been saturated with certain salts (Table 3.2). As seen in Fig. 3.5, the choice of Na_2CO_3 (curve A) or Na_2SO_4 (curve B) as the salt is unsatisfactory owing to the low value of dV/dt, whence an implied low efficiency. The choice of Na_2HPO_4 (curve C) or $Na_2B_4O_7$ or both Na_2HPO_4 and Na_2SO_4 (curve D and also Table 3.2), however, results in V-t and I-t curves similar to those found when barrier films are formed on Nb, Ta, V, or W (5,7). We will subsequently refer to the electrolyte consisting of ethylene glycol saturated with both Na_2HPO_4 and Na_2SO_4 as "electrolyte A". This electrolyte was finally chosen, Sec. 4.2.2, to be employed in the anodic sectioning procedure for Be as it yields more satisfactory results in stripping the films. Therefore, additional investigations were carried out concerning electrolyte "A" which will be discussed in the following sections.

3.4 Anodizing efficiency with "electrolyte A"

Experiments of two kinds were done to determine the anodizing efficiency with electrolyte A. First of all, Be thicknesses inferred by integrating I-t curves with expanded time scales, such as those shown in curves A and B of Fig. 3.6 were compared with true Be thicknesses calibrated gravimetrically, Sec. 4.4. The results, summarized in Table 3.4, indicate an efficiency of ∿ 0.7, valid for conditions of fixed current followed by fixed potential.

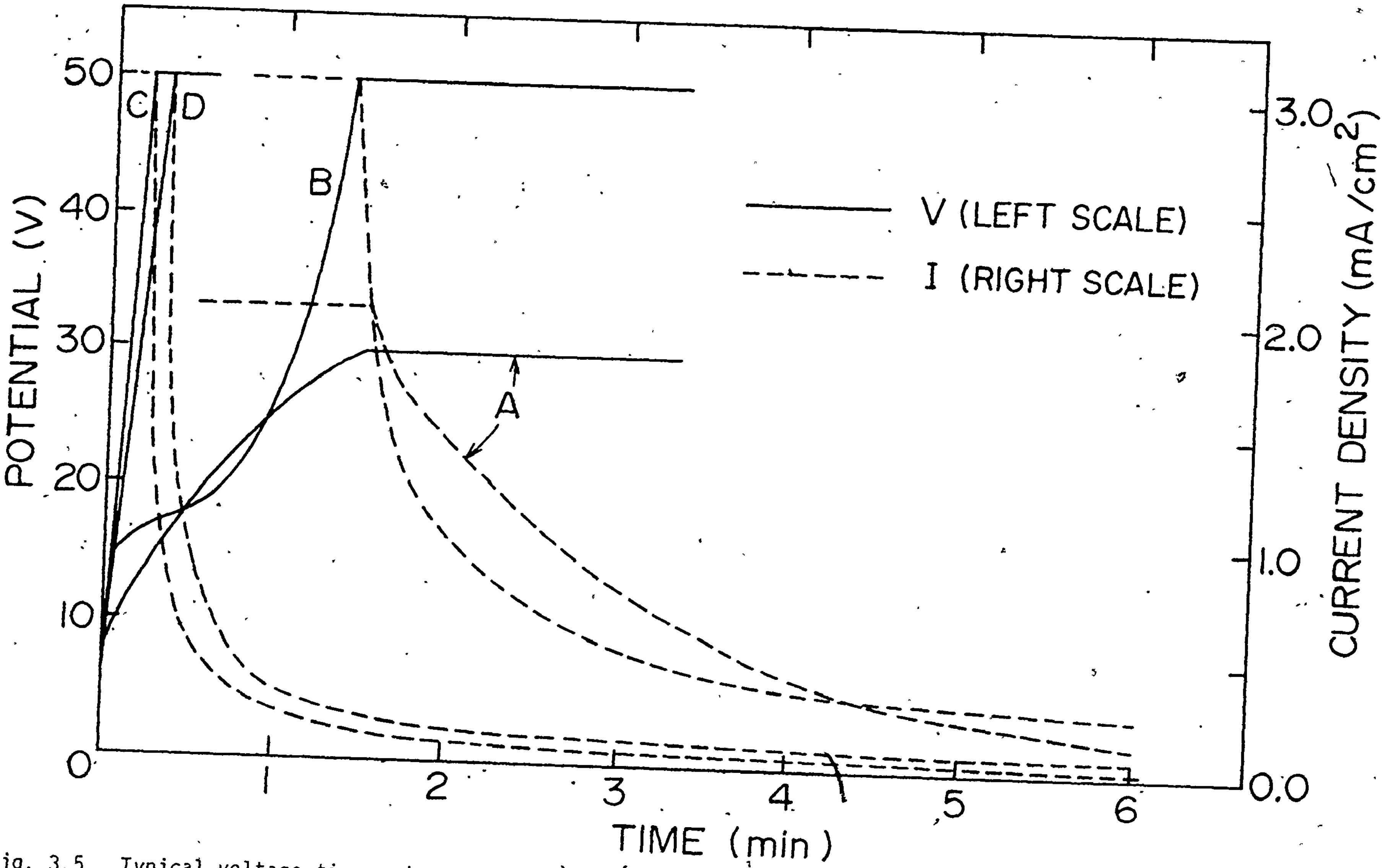

Fig. 3.5. Typical voltage-time and current-time curves for the anodizing of Be in ethylene-glycol-based electrolytes. Curve A: ethylene glycol saturated with Na_2CO_3 (abnormally low dV/dt). Curve B: ethylene glycol saturated with Na_2SO_4 (abnormally low dV/dt). Curve C: ethylene glycol saturated with Na_2HPO_4 (no anomalies). Curve D: ethylene glycol saturated with both Na_2HPO_4 and Na_2SO_4 ("electrolyte A"; no anomalies). Solid lines: V-t, with potential as in scale at left. Dashed lines: I-t, with current as in scale at right.

The dependence of dV/dt on the total current I can be used to estimate the efficiency under conditions of fixed current. The basic relation, which remains valid even if (as in the present work) the I-R drop in the electrolyte is not corrected for, is

$$\frac{dV}{dt} \propto i_1 = k(I-i_2-i_3), \qquad 3.1$$

where i_1 is the ionic current, i_2 is the electronic current (which usually causes oxygen evolution) and i_3 is the current leading to film dissolution (8). Accordingly, a second group of experiments was carried out. The primary data were as in Fig. 3.6, and from these dV/dt vs. I plots as in Fig. 3.7 were constructed. The intercept with the current axis represents the non-ionic current density, namely,

$$i_2 + i_3 = 0.15 \pm .05 \text{ mA/cm}^2,$$

when I is 3 mA/cm^2. The efficiency follows as 0.95 ± 0.02 and is thus markedly greater for fixed current than for fixed current plus potential. This result is understandable if it is remembered that the contribution of $i_2 + i_3$ will depend on the total anodizing time (7) and the times were ∿ 15 s at fixed current but 100 s at fixed current plus potential.

3.5 Porosity, dissolution, and crystallinity with "electrolyte A"

Fig. 3.8 shows scanning electron micrographs obtained for a film formed on Be with "electrolyte A". Comparison with Figs. 3.2 and 3.4 suggests a significant freedom from porosity.

The depth-distribution technique showed that the metal dissolution during anodizing was essentially a minimum (Table 3.2). "Electrolyte A" differs in this respect from all others that were examined. Stated in other terms,

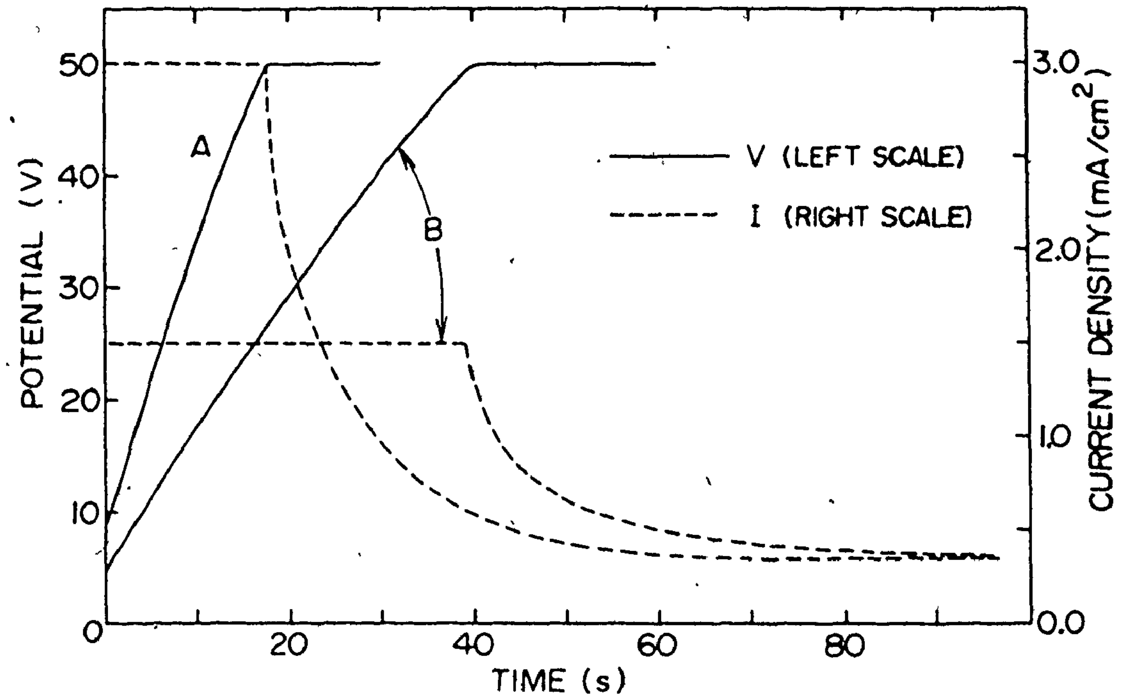

Fig. 3.6. Like curve D of Fig. 3.5 but plotted with an expanded time scale. An appropriate analysis of such curves is shown to yield the anodizing efficiency for conditions both of constant current and of constant current followed by constant potential.

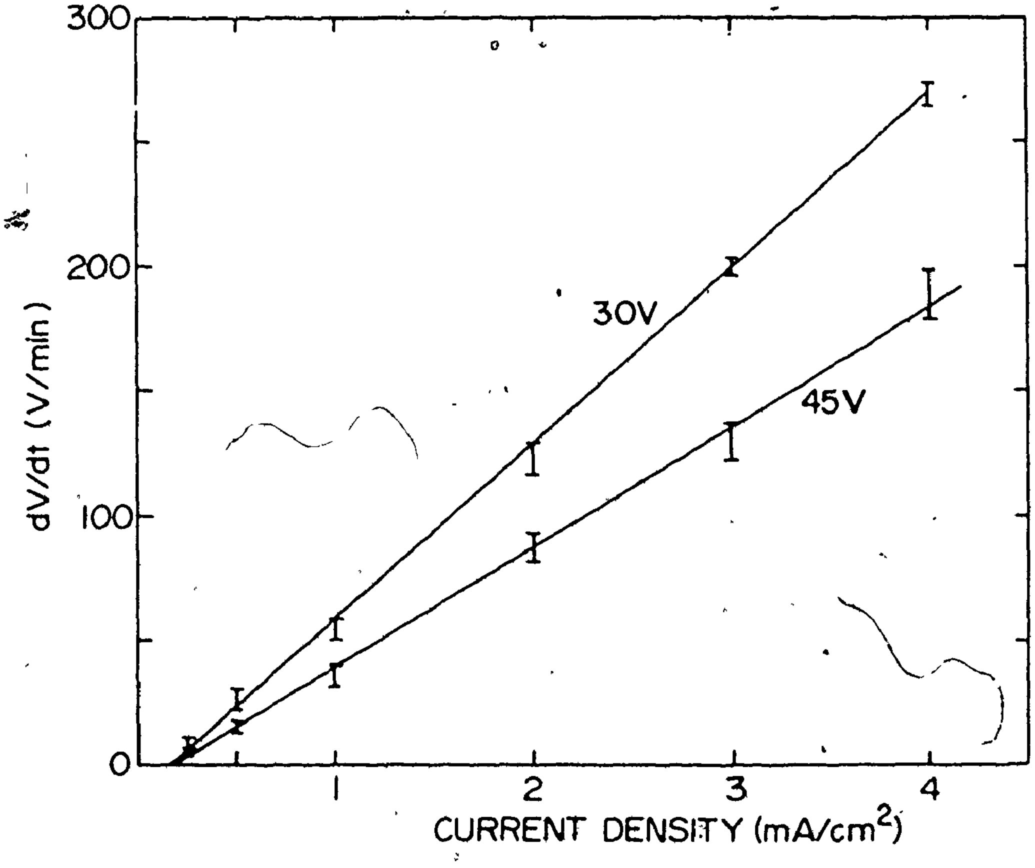

Fig. 3.7. dV/dt vs. I for the anodization of Be in "electrolyte A". Given that dV/dt is proportional to the ionic current as in Eq. (3.1), these curves serve to separate the total current of 3 mA/cm^2 into an ionic part of 2.85 ± 0.05 mA/cm^2 and a non-ionic part of 0.15 ± 0.05 mA/cm^2.

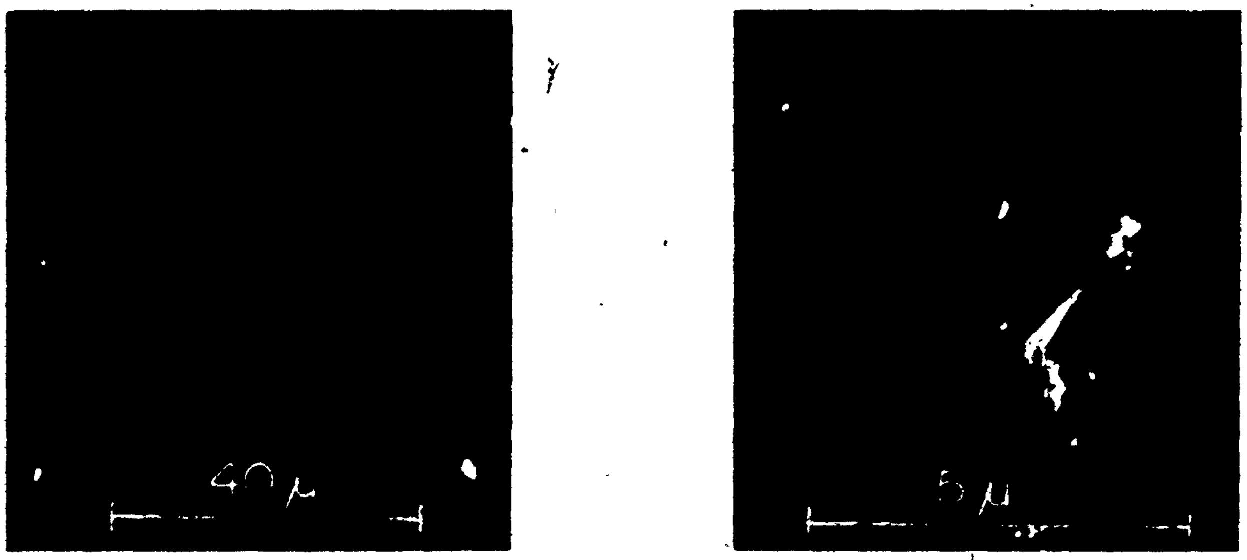

Fig. 3.8 Scanning electron micrographs with different magnifications of film formed by anodizing Be in "electrolyte A" for 1.5 min with a preset current of 3 mA/cm^2 and a preset potential of 50 V. The films are significantly free from porosity.

TABLE 3.4. Anodizing efficiency for Be using "electrolyte A"

Preset potential	Anodizing time	Charge passed[a]	Be thickness from Faraday's law[b]	True Be thickness from Eq. 4.1	Anodizing efficiency
(V)	(s)	(C/m^2)	(μg/cm^2 of Be)	(μg/cm^2 of Be)	
25	100	475±20	2.21±0.09	1.51±0.15	0.68±0.4
50	100	1010	4.71±.14	3.15±.25	0.67±.04

[a] Given by the total area under I-t curves as in Fig. 3.6 for an initial current density of 3.0 mA/cm^2. Repeated 3 times for each preset potential.

[b] Calculated assuming an efficiency of 1.00.

the dissolution current, i_3, is evidently less important than the electronic current, i_2, in lowering the anodizing efficiency to $\sim$ 0.7 for conditions of fixed current plus potential.

Fig. 3.9a shows a reflection electron diffraction pattern typical of a film as formed with "electrolyte A". The film is nominally amorphous. After heating the films in a vacuum of about 1 x 10^{-4} Pa at 315°C (Fig. 3.9(b)), 365°C (c), 415°C (d), 465°C (e) or 600°C (f), the diffraction patterns revealed increasing degrees of crystallinity, such that the heating at 600°C led to overt polycrystallinity. The comparison with Fig. 3.3b showed that the rings were those of hexagonal BeO.

It is important to note here that the existence of halos in an electron diffraction pattern is not sufficient to prove non-crystallinity.

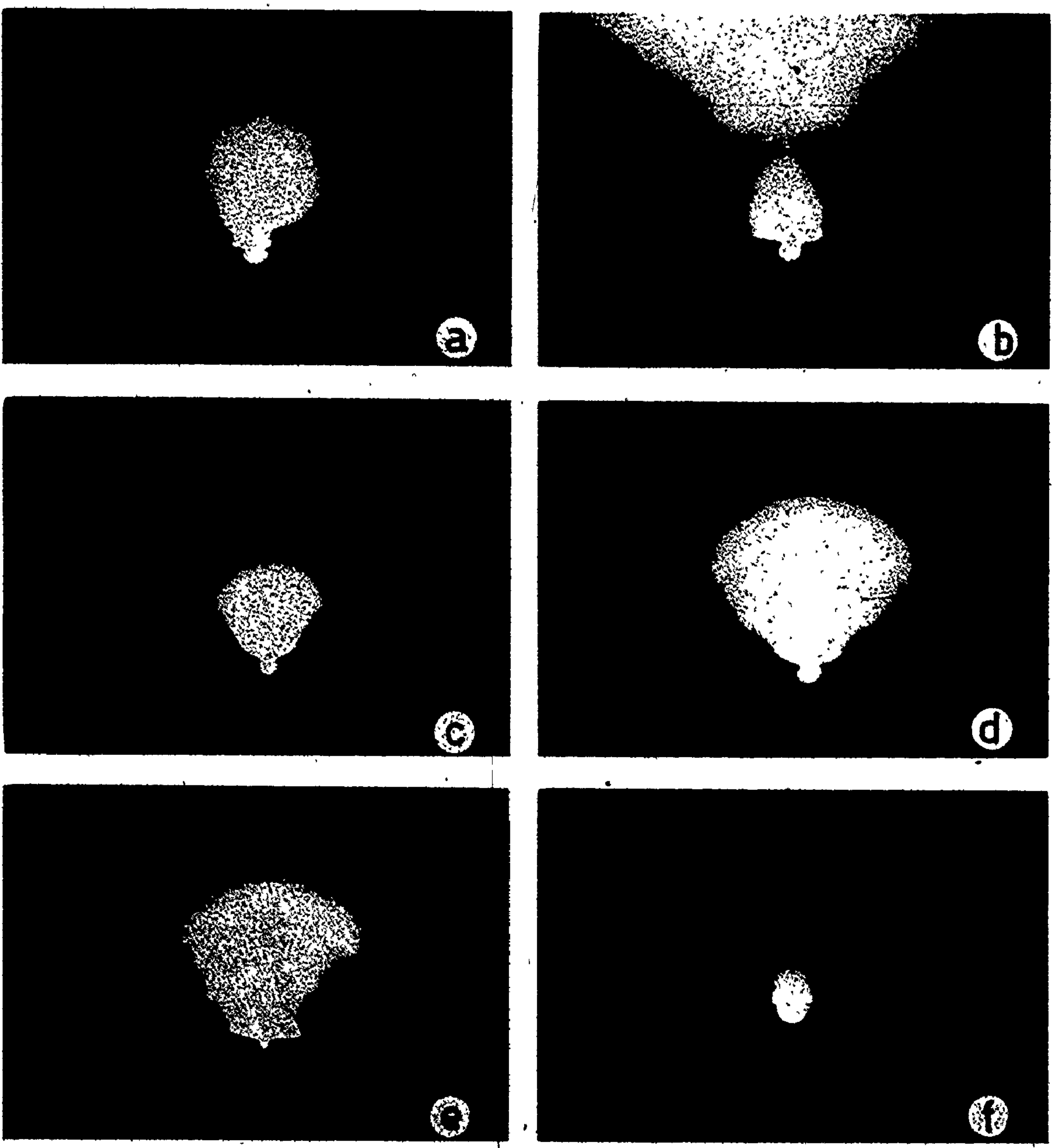

Fig. 3.9. Reflection electron diffraction patterns taken at 80 kV of film formed by anodizing Be in electrolyte A at 50 V. Image a: as-formed film showing halos such as are conventionally ascribed to an amorphous structure though can also arise from microcrystallites having sizes of 1-2 nm. Other images are for films heated for 1/2 hour in a vacuum of 1 x 10^{-4} Pa at (b) 315°C, (c) 365°C, (d) 415°C, (e) 465°C and (f) 600°C, showing the halos to have split into rings identifiable as hexagonal BeO.

The halos might be due to the overlapping of several diffraction rings, each of which is broadened due to small grain size (24). The halo width can be followed as a function of temperature, with the help of Fig. 3.9, and this indicates that the as-formed film either crystallises at ∿ 300°C or else is subject to grain coarsening at this temperature. For a material with such a high melting temperature (2550°C) and low diffusivity ($D \approx 10^{-12}$ cm^2/s at 1100°C) only the former (crystallization) is reasonable, and the films are more likely amorphous. To get further information on the amorphicity of the as-formed films, a gas-release analysis was undertaken. The details for the various stages or processes of gas-release analysis are described elsewhere; cf. the review paper by Matzke (25) and earlier papers of Kelly and Matzke (26) and Kelly and Jech (27). Here, we are considering stage IB release which is defined as release of implanted inert gas which is swept out by the motion of the amorphous-crystal interface. Such interface motion has been analysed (28) and found to lead to a temperature width, at the half maximum height of the release peak, of $\Delta T_{1/2}/T_{max} < 0.12$ K/K. The experimentally observed values for Al_2O_3, Cr_2O_3, Fe_2O_3, MoO_3, TeO_2, TiO_2, V_2O_5, Ge and Si all lie in the range 0.060 to 0.093 K/K (28). The temperature width for stage IB is thus much narrower than that for a true diffusion process. For example, stage IIA release of implanted inert gas, assumed to be due to unperturbed diffusion, is characterized by (28) $\Delta T_{1/2}/T_{max} = 0.15 \pm 0.01$ K/K. However, we should point out that in order to apply gas-release analysis to confirm the amorphicity of anodic films, one has to insure that the amorphous structure is not developed by ion impact. An encouraging result for our case is that crystalline BeO does not amorphise during ion impact, remaining crystalline even at high bombardment doses (29,30).

The results for anodic BeO films are shown in Fig. 3.10. Curve A appears to correspond to a crystallization process in view of the value of $\Delta T_{1/2}/T_{max}$ = 0.072 ± .007 K/K. Accordingly the crystallization temperature for the as-formed amorphous film is 290 ± 10°C in good agreement with the diffraction patterns of Fig. 3.9. Curve B of Fig. 3.10, with $\Delta T_{1/2}/T_{max}$ = 0.13 ± .01 K/K is evidently more nearly indicative of diffusion than crystallization and this serves to confirm the initial assumption that BeO was not subject to amorphization under ion impact. Though of no interest in the present context the peak temperature of curve B, 660 ± 20°C, could in principle be used to deduce a diffusion coefficient for the system Kr-BeO.

3.6 Discussion and Conclusions

3.6.1 Anodization of Beryllium

The results presented here have shown that the behaviour of Be with regard to anodizing is much like that of Al (31) and Sn (13,32). Porosity, dissolution, and crystallinity can be varied almost at will depending on the electrolyte, with overall results as in Table 3.5. There is a fairly good correlation between the three possible results, namely dissolution, film plus dissolution, and film without dissolution, and the pH as predicted by the Pourbaix diagram. Doping, i.e. electrolyte incorporation, also plays a role, however, and it is therefore difficult to judge whether pH or doping is more important in particular cases. The fault here lies in the failure to realize the importance of the Pourbaix diagrams, which indeed are normally not used in the context of anodizing,

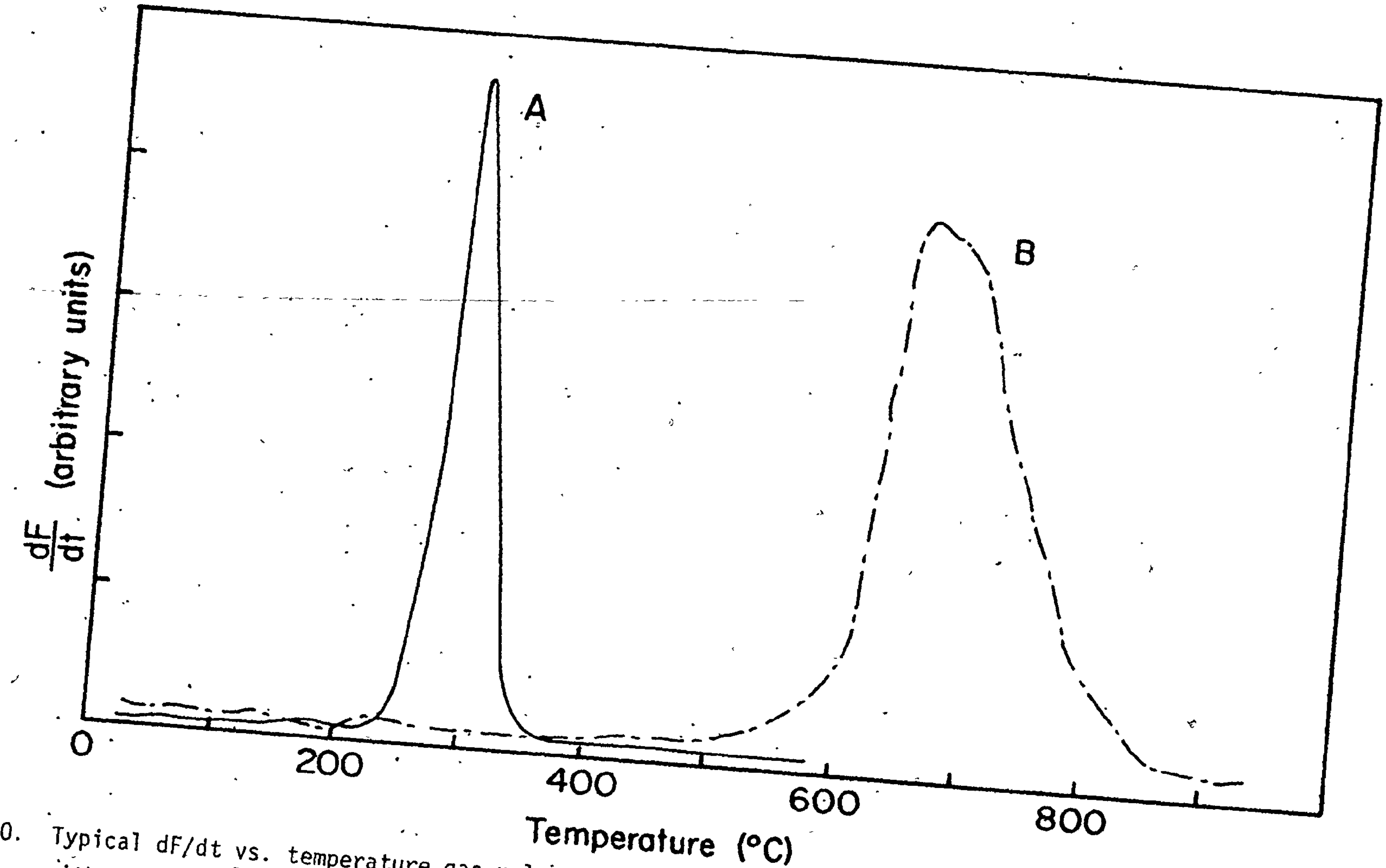

Fig. 3.10. Typical dF/dt vs. temperature gas-release curves for BeO anodic films which have been labelled with 20 keV Kr^{85} (10^{15} ions/cm^2). The flow gas was He. (A) As formed amorphous film showing $T_c \approx 290 \pm 5$°C. (B) BeO crystallized by a prior heating at 600°C for 1/2 hr, showing gas-release which correlates with unperturbed diffusion at ∼ 660°C.

TABLE 3.5 Summary of Be Anodizing

Electrolyte	Film?	Current at fixed potential	Porous?	Dissolution?	Crystallinit
1. Strong oxidizing					
CrO_3-HNO_3 mixture	yes	constant	yes	yes	hexagonal BeO
2. Aqueous					
1% H_2SO_4 or 1% HNO_3	no	constant	-	yes	-
1% KOH	yes	falls slowly	-	yes	-
0.5 m Na_2CO_3	yes	falls slowly	slight	yes	crystalline
3. Non-aqueous					
mainly acetic acid	yes	falls rapidly	-	yes	-
$(C_2H_5)_2SO_4$-H_2SO_4 mixture	yes	constant or nearly constant	-	yes	-
$(C_2H_5)_2HPO_4$	yes	nearly constant	-	yes	-
E.G. + Na_2CO_3	yes	falls rapidly	-	yes	-
E.G. + $Na_2B_4O_7$	yes	falls rapidly	-	yes	-
E.G. + Na_2SO_4	yes	falls rapidly	-	yes	amorphous
E.G. + Na_2HPO_4	yes	falls rapidly	-	no	-
"electrolyte A"	yes	falls rapidly	no	no	amorphous

sufficiently early in the work.

The most interesting electrolytes would appear to be those consisting of ethylene glycol saturated with Na_2HPO_4 or both Na_2HPO_4 and Na_2SO_4 ("electrolyte A"). The V-t and I-t behaviour suggested that a voltage-dependent limiting thickness was obtained (Figs. 3.5 and 3.6). The films were found to be non-porous (Fig. 3.8) and dissolution to be undetectable (Table 3.2). The films were also found to be amorphous, with a crystallization temperature of 290 ± 10°C and with the crystallization product consisting of hexagonal BeO (Fig. 3.9). They thus more nearly resembled the chemically precipitated BeO studied by Kerr (30) than the anodic films obtained in previous work (1,2,4). Anion incorporation in the anodic film from the electrolyte, such as that demonstrated with Ta (5,33), is believed to have played a role and will be investigated in Chapter 6.

The anodizing efficiency using "electrolyte A" was determined in two ways: from Faraday's law and from dV/dt. Use of the former gave a value of ∿ 0.7, valid for conditions of fixed current followed by fixed potential. Use of dV/dt gave a value of 0.95 ± 0.02, valid for fixed current. Efficiencies of less than unity will arise whenever electronic current, i_2, or dissolution current, i_3, play a role. The lack of dissolution (Table 3.2) shows that i_2 is the more important in the present case. We attribute this role of electronic current to the relatively low thicknesses of the anodic films formed on Be (Eq. 4.3) such that the resulting fields across the films are a factor of 3 higher than with most other metals (Table 3.1). This could in principle lead to Frenkel-Poole emission.

We will in the next chapter treat the converse of film formation, namely the quantitative removal of films. This leads first of all to a microsectioning technique, thence to the possibility of studying diffusion and ion depth distributions in Be. We note in this connection that Be is a particularly interesting material for depth-distribution work in view of its low mass. Film removal also has a purely electrochemical interest, in that it leads to explicit information on efficiencies such as that in Table 3.4.

3.6.2 Application to Other Systems (Fe)

The present work constitutes the first instance in which Be has been anodized under controlled conditions, the important feature being the choice of the electrolyte. In this respect we have established a logic in categorizing the various types of electrolytes, have suggested that Pourbaix diagrams play an important role, and have made use of simple, rapid experiments to establish, even if indirectly, the ability of an electrolyte to form an anodic film. The effectiveness of this approach is shown by its recent application to iron, the technologically most important metal of all. Thus recent results (12) showed that Fe, based on the ideas developed here, can be anodised at up to 150 V (Fig. 3.11) resulting in the formation of a thick, amorphous, and nearly protective oxide. However, the films suffer one practical drawback: they tend to be cracked (Fig. 3.12) and badly adherent. Nevertheless, the following details are significant:

(1) The formation of the anodic film on Fe was carried out in ethylene glycol electrolyte saturated with metaphosphoric acid (containing 60%

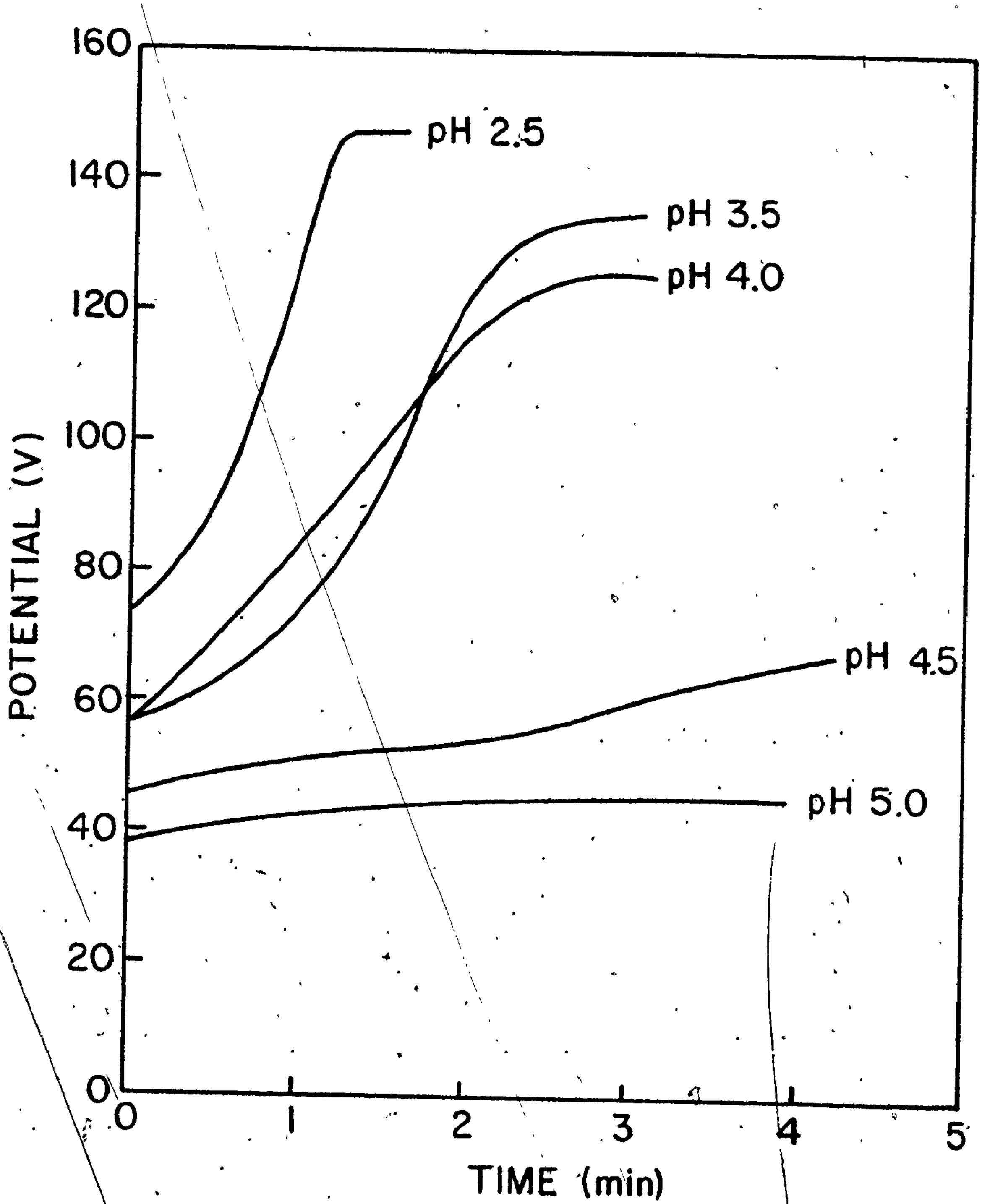

Fig. 3.11. Voltage-time curves for anodizing Fe in electrolytes of varying pH. The solutions are made more alkaline by adding different amounts of NaH_2PO_4 to ethylene glycol which was previously saturated with metaphosphoric acid (ref. 12).

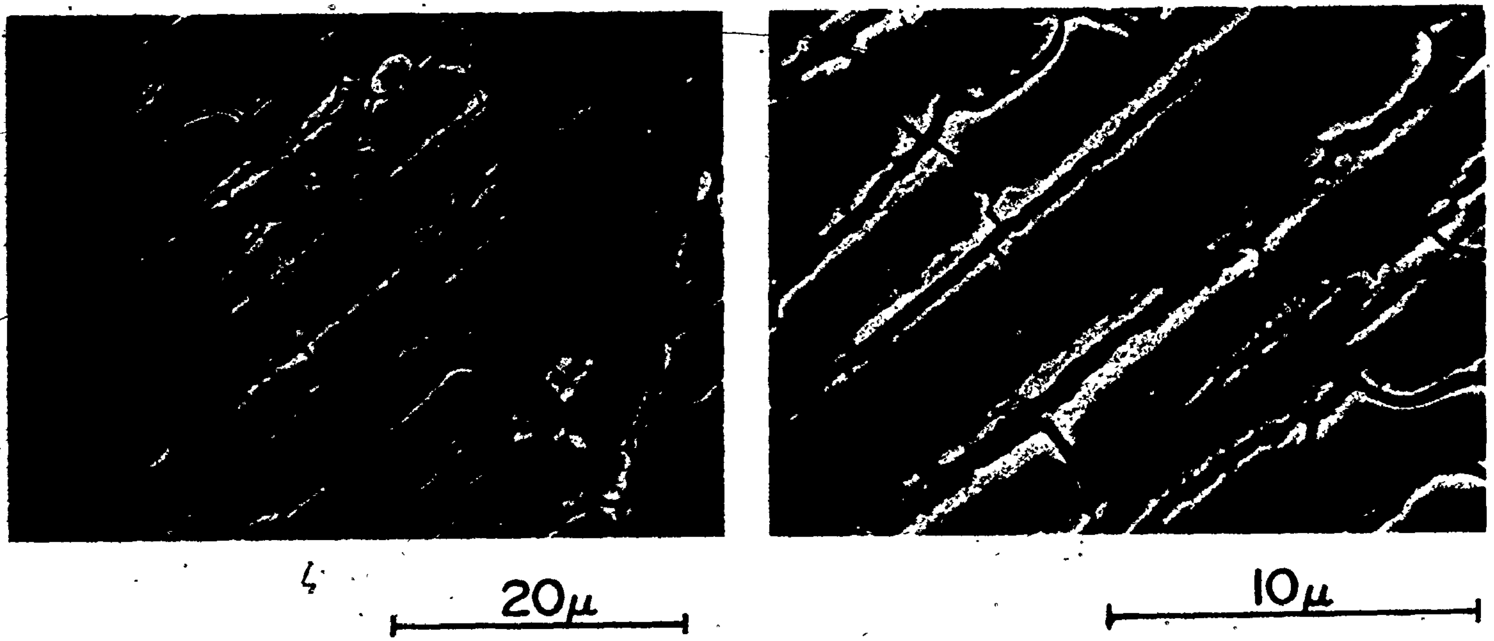

Fig. 3.12 Scanning electron micrographs with different magnifications of film formed by anodizing Fe in ethylene glycol electrolyte saturated with metaphosphoric acid (containing 60% NaH_2PO_4) at 135 V. The film tends to be cracked and badly adherent (ref. 18).

$NaPO_3$). This gives a solution with a pH of 2.5, which is in the range expected from the Pourbaix diagram for iron (Fig. 3.13). In disagreement with the diagram, however, solutions with pH > 5 were unsuccessful.

(2) The as-formed anodic film is found to be amorphous, and when crystallized, yields the diffraction pattern of γ-Fe_2O_3. The stoichiometry of the film thus agreed with the result of Cohen (34), who has shown that a thin film of γ-Fe_2O_3 is formed on iron during passivation. This thin film is found to be a strongly oriented, epitaxial microcrystalline cubic oxide. The fact that the thicker films were found to be amorphous in the recent work is not a problem. As pointed out in Section 2.5, anodic films on Al, Mo, Ta, V, and W are also amorphous when thick but crystalline when thin (< 9-30 nm).

(3) Phosphates are found to be a necessary electrolyte component for the successful formation of the oxide film, whereas in an analogous sulphate solution the oxide film was unsatisfactory, in spite of the pH of the solution being adjusted to 2.5-3. In such a case, a poorly adherent film is formed which tends to dissolve into the electrolyte. This, interestingly, resembles the findings with Be observed here, namely that the dissolution when anodizing Be in the sulphate electrolyte is higher than that when using phosphate electrolyte. In the latter, almost no dissolution at all is observed (Table 3.2). Likewise, with Nb and Ta, the use of sulphate-containing electrolytes was found essential to impart solubility (5).

(4) In general, we are thus again left in the quandary that both pH and doping appear to play an important role in the formation of anodic films. It will have to await future work for a more systematic study

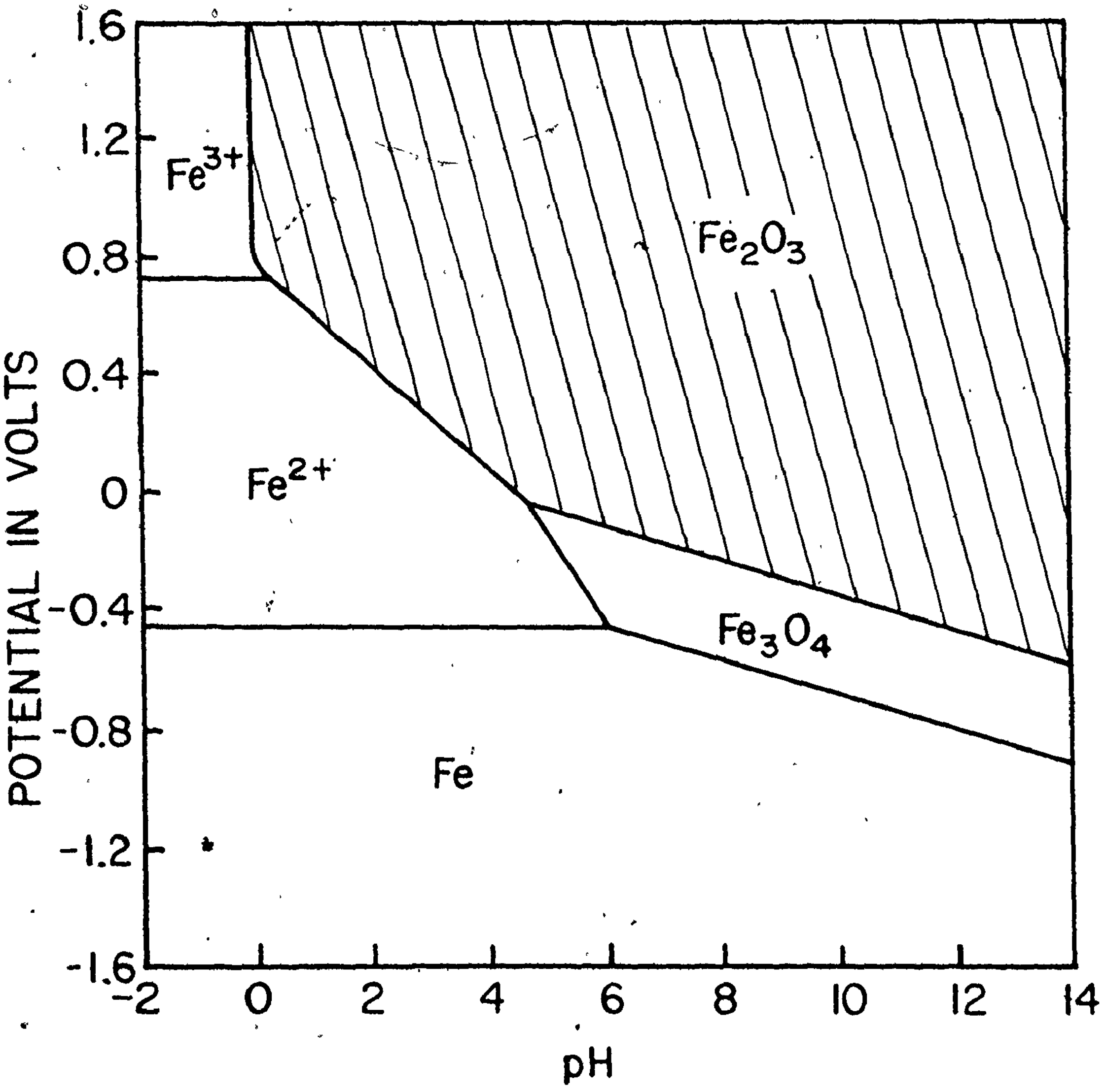

Fig. 3.13. Potential pH diagram for iron at 25°C (simplified).

to be made and a genuinely scientific basis established for anodizing. When that time comes, it is hoped that a number of technical important materials such as Cr, Ni, and Zn can be considered.

REFERENCES TO CHAPTER 3

1. I.S. Kerr and H. Wilman, J. Inst. Metals, 84, 379 (1955-56).
2. M.L. Levin, Trans. Faraday Soc., 54, 935 (1958).
3. R.M. Al'tovskii, A.G. Fedotova, M.I. Urazbaev, and S.I. Korolev, Prot. Metals, 5, 172 (1969).
4. K.E. Heusler, Ber. Bunsengesellschaft, 67, 943 (1963).
5. M.R. Arora and R. Kelly, Electrochimica Acta, 19, 413 (1974).
6. M.R. Arora and R. Kelly, J. Electrochem. Soc., 119, 270 (1972).
7. M.R. Arora and R. Kelly, ibid., 120, 128 (1973)
8. J. Siejka, J.P. Nadai and G. Amsel, ibid., 118, 727 (1971).
9. M.R. Arora, Ph.D. Thesis (McMaster University, 1974), p. 60.
10. N.Q. Lam and R. Kelly, Can. J. Phys., 48, 137 (1970).
11. A. Charlesby, Acta Met., 1, 340 (1953).
12. C. DiDonato and R. Kelly, unpublished work, McMaster University (1978).
13. E. Giani and R. Kelly, J. Electrochem. Soc., 121, 394 (1974).
14. J.P.S. Pringle, ibid., 120, 398.
15. A.I. Vol'fson, N.E. Markova, V.V. Chernyshev, V.N. Lebedev, and V.V. Vavakin, Prot. Metals, 9, 321 (1973).
16. D.K. Smith, C.F. Cline, and S.B. Austerman, Acta Cryst., 18, 393 (1965).
17. M.R. Arora and R. Kelly, J. Mat. Sci., 12 (1977) 1673.
18. O. Flint, J.J. Polling and A. Charlesby, Acta Met., 2, 696 (1954).
19. M.T. Thomas, J. Electrochem. Soc., 117 (1970) 396.
20. A. Aladjem, D.G. Brandon, J. Yahalom, and J. Zahavi, Electrochim. Acta, 15, 663 (1970).
21. P.H.G. Draper and J. Harvey, Acta Met., 11, 873 (1963).

22. D.G. Brandon, J. Zahavi, A. Aladjem, and J. Yahalom, J. Vac. Sci. Techn., 6, 783 (1969).

23. R.G. Keil and R.E. Salomon, J. Electrochem. Soc., 115, 628 (1968).

24. S. Mader, in Recrystallization, grain-growth, and textures (ASM, Metals Park, Ohio, 1966), p. 523.

25. Hj. Matzke, Lecture at the summer school on the physics of ionized gases, Herceg-Novi, Yogoslavia, 1970.

26. R. Kelly and Hj. Matzke, J. Nucl. Mat., 17, 179 (1965).

27. R. Kelly and C. Jech, J. Nucl. Mat., 30, 122 (1969).

28. H.M. Naguib and R. Kelly, Rad. Effects, 25, 79 (1975).

29. H.M. Naguib and R. Kelly, Rad. Effects, 25, 1 (1975).

30. I.S. Kerr, Acta Cryst., 9, 879 (1956).

31. R.A. Harrington and H.R. Nelson, AIMME, Inst. Metals Div., 137, 62 (1940).

32. R. Kerr, J. Soc. Chem. Ind., 57, 405 (1938).

33. G. Amsel, C. Cherki, G. Feuillade, and J.P. Nadai, J. Phys. Chem. Sol., 30, 2117 (1969).

34. M. Cohen, J. Electrochem. Soc., 121 (1974) 191c.

CHAPTER 4

ANODIC SECTIONING OF BERYLLIUM

4.1 Introduction

Over the past decade, various approaches for the microsectioning of metals have been developed. These include chemical dissolution,(1,2) anodic sectioning,(3-13) formation and dissolution of films other than oxides,(14) vibratory polishing,(15) bombardment-induced solubility of surface layers,(16,17) and sputtering.(18-20) These techniques have their main applications in measuring depth distributions of implanted ions and radiation damage, and in determining diffusion coefficients at low temperatures.(21)

While anodic sectioning is probably the most effective microsectioning technique, there is a severe problem in that it is not universally applicable, such that for some time the only substances allowing anodic sectioning were Al(3), Si(5,13), Au(6) and W(4). More recently programs undertaken in our laboratory(8,9,10) and elsewhere(11,12) have made possible the anodic sectioning of Mo(8), V(9), Nb, Ta(10), Ag(11), and Cu(12). It is thus possible to microsection elements having masses ranging from 27 to 196.

We will consider in this chapter the anodic sectioning of Be, which is the lowest mass target that can be conveniently worked with in the field of atomic collisions. The difficulty in the anodic sectioning of Be, as with most metals, appeared at first sight to lie in establishing conditions under which a barrier-type, stable, amorphous film could be formed. However, we showed in the previous chapter that such films were easily obtained by the use of electrolytes based on ethylene glycol which is saturated with Na_2HPO_4 or KH_2PO_4 or both Na_2HPO_4 and Na_2SO_4. The oxide films formed in these electrolytes are barrier type (defined in terms of the voltage-time and current-time characteristics), are formed with negligible dissolution, and are amorphous. As will be seen, these films readily permit microsectioning such that uniform layers 2.7-20 nm thick can be removed.

An important aspect of what follows is that an attempt will be made to establish a "logic" for anodic sectioning. We will, for example, show why the electrolyte must contain both sulphate and phosphate ions, and not just one or the other.

4.2 The Anodizing-Stripping Procedure

4.2.1 The Choice of the Electrolyte

The main requirements of an electrolyte to be used for anodic sectioning are that it should lead to films which are barrier-type, stable, and amorphous. Being barrier-type assures that a voltage-dependent limiting film thickness exists, stability assures, in a general sense, that the film does not dissolve extensively in the electrolyte during formation, while amorphicity often plays a role in enabling the films to be chemically stripped without the metal substrate being attacked. (Amorphous films have higher chemical potentials than do crystalline films.) We showed in the previous chapter that the most interesting electrolytes for Be are those consisting of ethylene glycol saturated with Na_2HPO_4, KH_2PO_4, Na_2SO_4, Na_2CO_3 or (Na_2HPO_4 + Na_2SO_4), the last being designated "electrolyte A". They were all found to lead to a voltage-dependent limiting film thickness as inferred by the voltage-time and current-time characteristics, discussed in Section 3.3. In addition, current efficiences were estimated by comparing $\int Idt$, i.e. the area under the current-time curves, with the film weight using electrolyte A. The results, shown in column 2 of Table 4.1, are subject to the major uncertainty that the film weights using electrolyte A are not fully relevant.

To evaluate the film stability, the extent of metal dissolution was determined. Be specimens were implanted with 30 keV ^{85}Kr (beta-active) to a dose of 2×10^{15} ions/cm^2, and the activity was noted before and after anodizing with presettings of 50 V and 3 mA/cm^2. If the activity profile is approximated as exponential (as in Fig. 4.4, to follow),

$$\text{integral concentration} = \exp(-x \ln 2/R_m) \qquad (4.1)$$

where R_m is the median range, taken from Figure 4.4 as 25.0 nm, results are obtained as in columns 3 and 4 of Table 4.1. Minimum losses clearly occurred with phosphate-containing electrolytes. It is readily seen by considering Figure 4.4 that the assumption of exponential profiles underestimates thicknesses in the range 90-100% activity. Specimens which were sectioned to about 50% activity and which should be accurately exponential with R_m = 25.0 nm were therefore used in conjunction with electrolyte A and the dissolution was found to be 2 ± 0.5 nm.

The question of the amorphicity of the films was dealt with in the previous chapter. The films formed in electrolyte A were found to be amorphous as indicated by reflection electron diffraction and gas-release spectroscopy, Sec. 3.5.

TABLE 4.1. Anodizing losses in ethylene-glycol based electrolytes for a preset voltage of 50 V and a preset current density of 3 mA/cm^2.

Electrolyte (ethylene glycol saturated with indicated compound)	Current efficiency*	Residual activity	Anodizing loss** (nm)
1. Na_2SO_4	$0.18 \pm .03$	0.73 ± 0.04	$\gtrsim 11.1 \pm 2.2$
2. Na_2CO_3	$0.23 \pm .03$	0.88 ± 0.02	$\gtrsim 4.6 \pm 0.9$
3. Na_2HPO	$0.90 \pm .04$	0.994 ± 0.008	$\sim > 0.2$
4. KH_2PO_4	$0.89 \pm .04$	0.994 ± 0.008	$\sim > 0.2$
5. 1:1 mixture of (1) and (3) ("electrolyte A")	$0.67 \pm .04$	0.986 ± 0.006	$\sim > 0.6$

---

* Deduced by assuming film weights as when electrolyte A is used.

** As calculated from eq. (4.1).

4.2.2 The Stripping Step

The search for a solvent for an anodic film is largely empirical, though is simplified if the film is labelled with a radioactive tracer. Specimens of Be were accordingly implanted with 30 keV ^{85}Kr, anodized with presettings of 50 V and 3 mA/cm^2 in each of the five electrolytes of Table 4.1, and exposed to a solvent. By considering the residual activity as in Fig. 4.1 it was found that 10% KOH had an optimum behaviour provided the electrolyte contained Na_2SO_4. Dissolution rates for the particular cases of electrolytes 1, 2, 3 and 5 are given in Table 4.2. Other

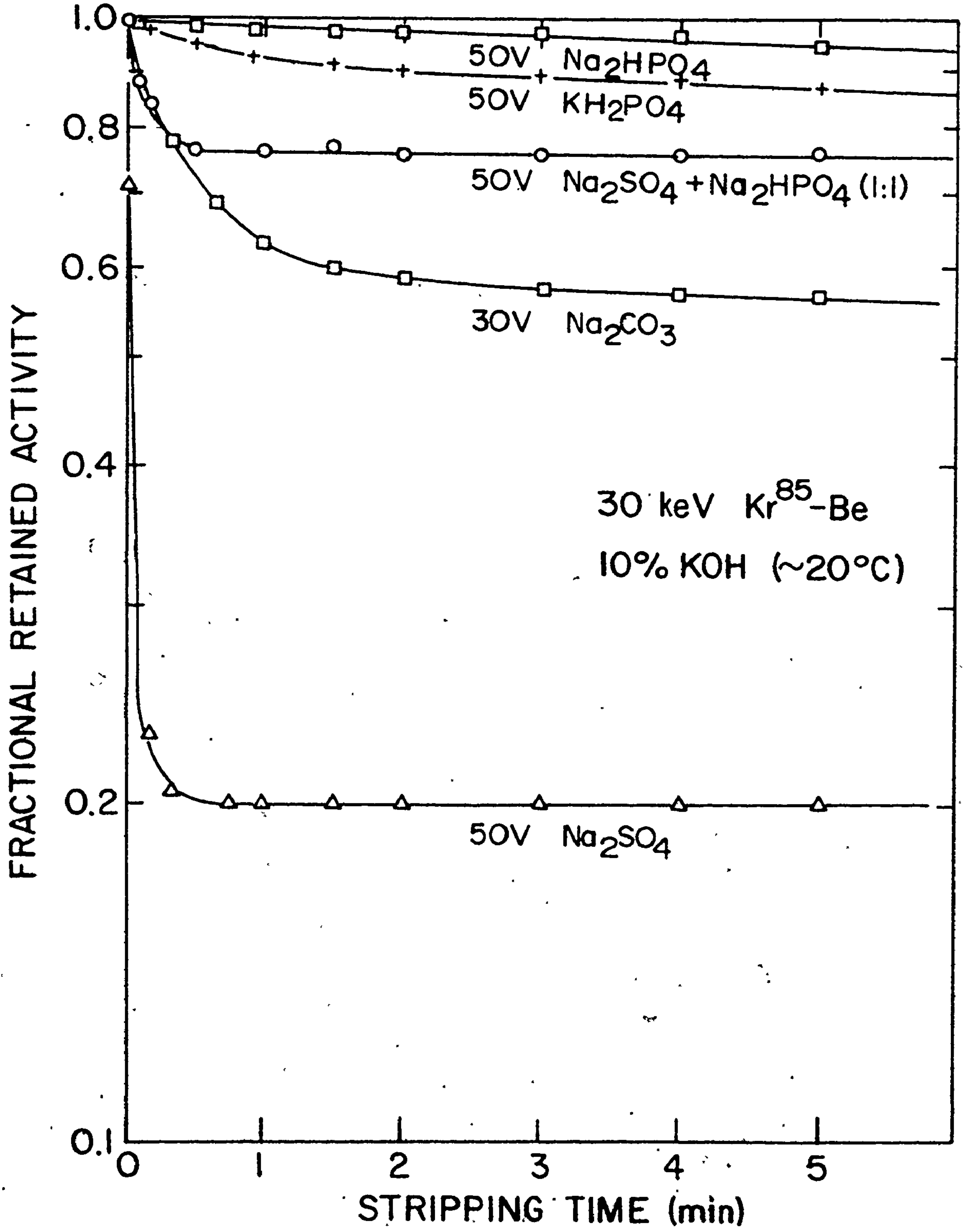

Fig. 4.1. Dissolution of anodic films on Be as inferred by the loss of activity that was introduced prior to anodization as 2 x 10^{15} ions/cm^2 of 30 keV ^{85}Kr. Films were formed at the voltages indicated in ethylene glycol saturated with the indicated compounds.

solvents considered were sulphuric acid, which attacked the metal, and solutions of Be salts, which were too slow. It has been hoped that solutions containing Be^{2+} would remove the anodic film by the formation of complex ions.(22)

Since phosphate incorporation minimized the dissolution losses (Table 4.1) and sulphate incorporation minimizes the stripping time (Table 4.2), it follows that a mixture might combine the behaviour. The results were favourable (Table 4.2).

The dissolution "end-point", 2 min in 10% KOH, was checked from the point of view of its actual representation of complete film stripping. In one series of experiments, specimens were anodically sectioned at 50 V 10-12 times. There was no evidence for accumulated film and the V-t curves were fully reproducible. The second check was done by noting the value of the initial voltage rise in the anodizing cell while applying a very small current density of 30 $\mu A/cm^2$. The initial voltage rise always lay in the region < 1V, corresponding to a thickness of roughly < 2 nm if one assumes the approximate relation, valid for virtually all anodizable metals

$$\text{(thickness in nm)} \approx (2.0 \pm 1.0) \times \text{volts.}$$

4.2.3 Summary of Anodic Sectioning Procedure

In summary, the films formed by anodizing Be for 2 min with a preset current density of 3 mA/cm^2 in electrolyte A at up to 50 V can be completely stripped within 2 min in 10% KOH solution. Electrolyte A, consisting of a 1:1 mixture of ethylene glycol saturated with Na_2SO_4 and ethylene glycol saturated with Na_2HPO_4, is chosen as leading to films having simultaneously low dissolution losses and optimum stripping behaviour.

TABLE 4.2 Rates of dissolution of anodic BeO films and Be metal in aqueous KOH at ∿ 20°C. Films were formed in the electrolytes indicated in Table 4.1.

Electrolyte	Solvent	Rate of anodic film dissolution (nm/s)	Rate of Be dissolution (nm/s)
#1	10% KOH	2	0.05
#2	10% KOH	0.1	0.05
#3	10% KOH	0.05	0.05
#5	sat. KOH	-	2.0
	10% KOH	1.0	0.05
	1% KOH	0.1	0.007

4.3 Formation of Doped Films

We found in the previous section that one of the key points in establishing the anodic sectioning technique for Be is to form the anodic film in electrolytes containing sulphate. The film then has enhanced solubility in 10% KOH. In fact, this principle has been also noted by Arora and Kelly(10) for films on Nb and Ta, and was exploited in establishing their anodic sectioning techniques. In addition, they have also observed that the incorporation of the electrolytic species into the anodic films is accompanied by an increase in the rate at which the film forms, as embodied in the quantity dV/dt for film growth at fixed current. For example, factor of two greater values of dV/dt are observed for Nb and Ta when a sulphate-containing electrolyte is used (cf. Fig. 2.6). They interpreted the result as originating from film doping such that the dielectric constant, ε_r, was decreased and as a result the dV/dt value was increased, as shown in Sec. 2.5.

Following this approach, values of dV/dt for film growth on Be in ethylene-glycol-based electrolytes have been determined with results as given in Table 4.3. It shows that the lowest dV/dt value, thence lowest inferred doping, is found for films formed in the carbonate-containing electrolyte. The highest dV/dt values, thence highest inferred doping, were obtained in the sulphate and phosphate-containing electrolytes. It should be pointed out that the dV/dt values were in most cases obtained by dividing the slopes by the total current I and not the film forming current i. Due to the high anodizing losses in the sulphate-containing electrolyte the film-forming current will be less as compared to the other electrolytes and this has been taken into account in Table 4.3.

It is of interest, as described in Sec. 4.2.2, that sulphate-doped films have greatly enhanced solubility rates in 10% KOH, whereas the stripping of films formed in the phosphate or carbonate-containing electrolytes was relatively slow. These results are in agreement with those reported on Ta by many authors, cf. Sec. 2.5, who indicated that phosphate doping does not lead to enhanced film solubility.

Thus for the incorporation of the electrolytic species into anodic films on Be has been inferred by dV/dt values and by the rate at which the film dissolves in 10% KOH. It will be seen in Sec. 4.4.2 that the gravimetric calibrations of the oxide film showed that 5-10% of the O^{2-} in the film is replaced by SO_4^{2-} and/or HPO_4^{2-}.

In Section 6.4, the presence and the distribution of the incorporated anions in the anodic films will be investigated by the photon-emission technique. The results will include a demonstration that the films are formed by cation migration and we point out here that such a mechanism is a sine qua non for doping to be practical.

TABLE 4.3 Values of dV/dt for constant-current film growth on Be in various electrolytes.

Electrolyte (ethylene glycol saturated with indicated compound)	dV/dt at 1 mA/cm^2 in volts/min*
1. Na_2SO_4	25** ± 3
2. Na_2CO_3	11 ± 2
3. Na_2HPO_4	26 ± 3
4. KH_2PO_4	25 ± 3
5. 1:1 mixture of (1) and (3)	25 ± 3

---

* Obtained by dividing the slopes of V-t curves at constant current by the total current I and not the film-forming current i.

** The anodizing losses in this electrolyte have been accounted for in obtaining this value.

4.4 Thickness Calibrations

4.4.1 Metal-Removal Thicknesses

Two methods were employed to determine metal-removal thicknesses. For larger thicknesses (25-50 V), weight-loss was used directly while for smaller thicknesses (10-20 V) the depth-distribution method(9) served to estimate the ratio (thickness)/(thickness at 50V). In the weight-loss method Be specimens were weighed, anodized and sectioned 5 to 12 times, and then reweighed. The repeated anodizing-stripping was, in fact, needed owing to the low density of the metal (1.85 g/cm^3). In the depth-distribution method, specimens were bombarded with 30 keV ^{85}Kr to a dose of 2 x 10^{15} ions/cm^2 and the residual activities were noted after repeated sectionings at a given low voltage. For example, the residual activity in three specimens after 20 sectionings at 10 V was found to be 0.16 ± 0.03. According to a 30 keV depth-distribution curve constructed from sectioning at higher voltages (Fig. 4.4, to follow), this activity corresponds to a thickness removed of 9.2 ± 0.4 μg/cm^2. The metal removed in a single sectioning at 10 V follows as being 0.46 ± 0.08 μg/cm^2.

Overall results are summarized in Table 4.4 and are included in Fig. 4.2. They can be represented to within 10% as follows:

$$\text{Thickness of metal removed} = -0.18 + 0.066\cdot V \ \mu g/cm^2$$
$$= -0.9 + 0.35\cdot V \ nm \qquad (4.2)$$

Fig. 4.3 compares metal-removal thicknesses for 8 systems permitting anodic sectioning.

4.4.2 Oxide Thicknesses

Oxide thicknesses for 20-50 V were determined by weight gain, using specimens having a surface area of 20.0 cm^2. Thicknesses for 10-15 V could, if desired have been obtained with a modified depth-distribution method.(9) The results are included in Table 4.4 and also in Fig. 4.2 and can be represented within 10% as follows:

$$\text{Oxide thickness} = -0.7 + 0.23\cdot V \ \mu g/cm^2$$
$$= -2.3 + 0.76\cdot V \ nm \qquad (4.3)$$

the nm form being contingent on the density being 3.0 g/cm^3.

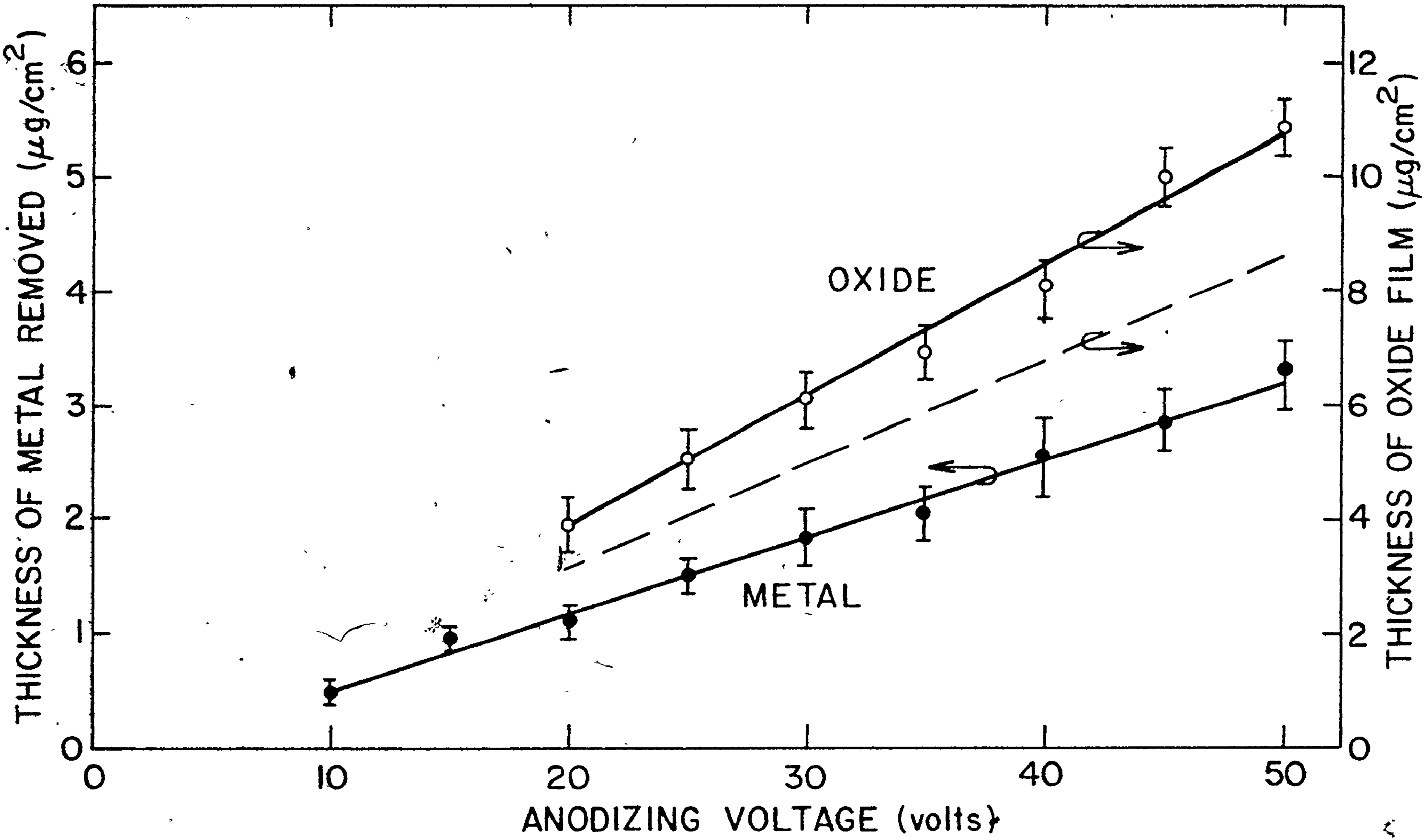

Fig. 4.2. Calibrations for metal-removal thicknesses (scale at left) and for oxide thicknesses (scale at right). The dashed line is for pure oxide based on metal-removal results.

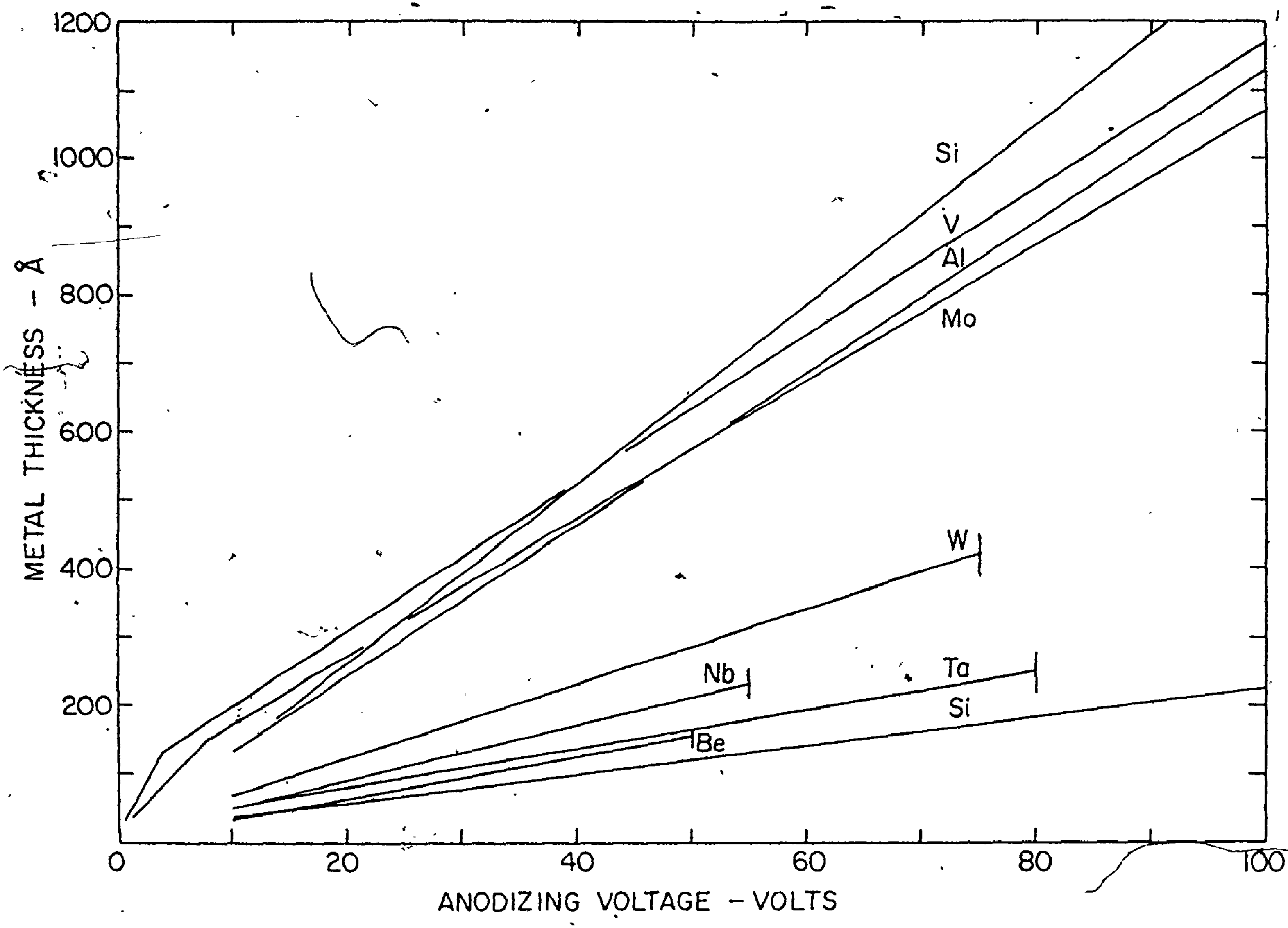

Fig. 4.3. Comparison of metal-removal thicknesses for 8 systems permitting anodic sectioning.

TABLE 4.4 Metal-removal and oxide-film thicknesses for Be anodized in electrolyte A

Anodizing voltage	Average metal-removal thickness ($\mu g/cm^2$)	Corresponding thickness from eq. (4.2) ($\mu g/cm^2$)	Oxide thickness ($\mu g/cm^2$)	Corresponding thickness from eq. (4.3) ($\mu g/cm^2$)
10	0.46 ± 0.08	0.48	-	-
15	0.95 ± 0.15	0.81	-	-
20	1.11 ± 0.15	1.14	2.92 ± 0.5	3.90
25	1.42 ± 0.15	1.47	5.06 ± 0.5	5.05
30	1.83 ± 0.26	1.80	6.12 ± 0.5	6.20
35	2.05 ± 0.24	2.13	6.88 ± 0.5	7.35
40	2.56 ± 0.35	2.46	8.14 ± 0.5	8.50
45	2.85 ± 0.25	2.79	10.3 ± 0.5	9.65
50	3.33 ± 0.41	3.12	10.85 ± 0.5	10.8

It will be noted in Fig. 4.2 that the observed oxide weights (solid line) are greater than would be expected for pure BeO based on the metal-removal weights (dashed line). The discrepancy is consistent with the film being doped by the incorporation of SO_4^{2-} and HPO_4^{2-} from the electrolyte. (The presence of S and P and their distribution in the anodic film are investigated in Sec. 6.4). Quantitatively, it can be understood if 5-10% of the O^{2-} in the film is replaced by SO_4^{2-} and/or HPO_4^{2-}. Whether this incorporation arises by the literal replacement of O^{2-} to yield a phase Be(O, SO_4, HPO_4), or by the physical trapping of Na_2SO_4 and/or Na_2HPO_4 is less easily decided. For example, the fact that Na profiles in the anodic films are nearer the surface than S and P profiles, Sec. 6.4, conveys little information owing to the likelihood that Na could migrate outwards (cf. (23), (24)). More significant is the result that the films crystallized to a product having the diffraction pattern of BeO alone, Sec. 3.5, as could be expected for a phase Be(O, SO_4, HPO_4).

4.5 Depth Distributions in Be and BeO

In view of the fact that, as already pointed out, Be is the lowest mass ~~target~~ that can be conveniently worked with in the field of atomic collisions, a limited number of experiments was carried out to determine the integral depth distribution of implanted 5, 15 and 30 keV ^{85}Kr ions in Be and BeO.

With Be, sectioning was accomplished using the procedure summarized in Sec. 4.2.3, with an anodizing voltage of 20 V for 5 keV and 50 V for 30 keV. Results based on a total of 40 experimental points are shown in Fig. 4.4 (solid lines). The reproducibility was such that the median ranges, i.e. depths at 50% activity, could be specified to within about 10% as follows:

1.9 μg/cm^2 for 5 keV
4.7 μg/cm^2 for 30 keV

With BeO the equivalent of sectioning was accomplished with the transmission technique. This consisted of forming anodic films on Be, implanting ^{85}Kr ions and counting the activity, stripping the films, and then determining the residual activity in the metal substrate. The results are shown in Fig. 4.5 (solid lines) with median ranges as follows:

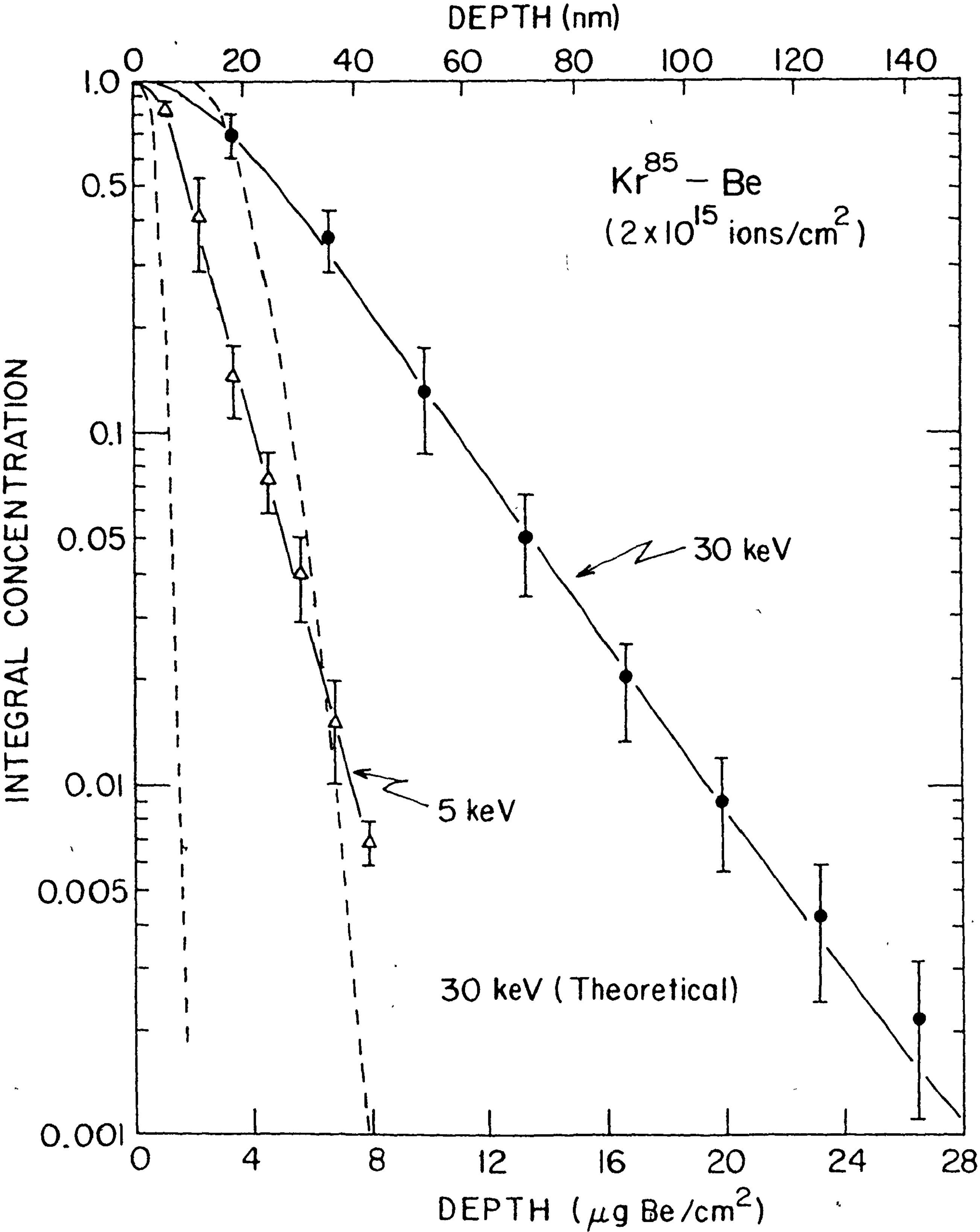

Fig. 4.4. Integral depth-distribution curves for 5 and 30 keV ^{85}Kr in polycrystalline Be. Dashed lines are the theoretical curves for amorphous Be.

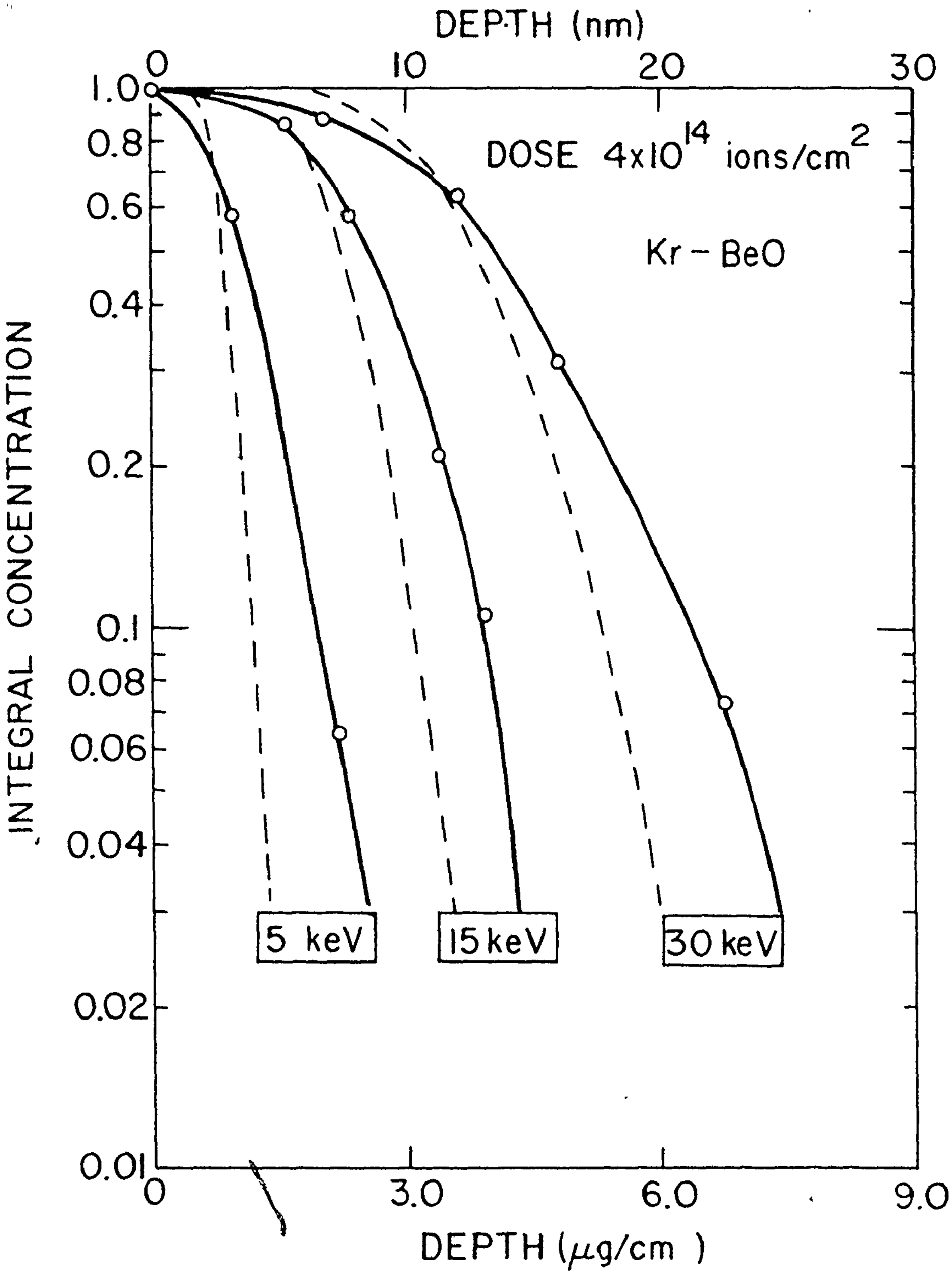

Fig. 4.5. Integral depth-distribution curves for 5, 15 and 30 keV ^{85}Kr in anodic BeO. Dashed lines are theoretical curves for amorphous BeO.

1.1 $\mu g/cm^2$ for 5 keV

2.6 $\mu g/cm^2$ for 15 keV

4.1 $\mu g/cm^2$ for 30 keV

Also shown in Figures 4.4 and 4.5 (dashed lines) are theoretical distributions constructed using an Edgeworth expansion in integral form(25) with the fourth moment ratio β_2 taken as:(26)

$$\beta_2 = 3 + \frac{5}{3}\ \beta_1,$$

where β_1 is the third-moment ratio. This expansion is as follows:

$$C^{int} = \frac{1}{2} \operatorname{erfc} (\zeta/2^{1/2}) - (1/(2\pi)^{1/2}) \exp(-\zeta^2/2)\ g(\zeta),$$

where ζ stands for $(x - \langle x\rangle)/\Delta x$ and $g(\zeta)$ stands for

$$\frac{\beta_1^{1/2}}{6} (1-\zeta^2) + \frac{\beta_1}{72} (5\zeta^3 - \zeta^5) + \ldots$$

The various ranges and moments were assigned values appropriate to carbon.(26)

The results were in all respects as expected, with Be showing the usual mixture of random and channeled stopping and BeO showing only random stopping. Noteworthy, however, is the fact that these results constitute an independent proof that anodic BeO is amorphous, the previous evidence being based on electron diffraction and gas-release, Sec. 3.5. The excessive skewness found with BeO, confirmed also with WO_3,(17) is possibly due to inadequacies in either the Edgeworth expansion or the Thomas-Fermi potential underlying the theoretical ranges and moments.

Powers and Whaling(27) have given experimental values for the ranges of Kr in Be using the momentum analysis of elastically scattered protons to accomplish the profiling. Their values for incident energies of 46 to 500 keV may be extrapolated to give 4.6 ± 0.8 $\mu g/cm^2$ at 30 keV, the present value being 4.7 ± 0.3 $\mu g/cm^2$.

4.6 Summary and Conclusions

(1) Most electrolytes consisting of ethylene glycol saturated with inorganic salts enable protective films to be grown on Be at 10-50 V. However, those formed in the presence of phosphate showed the least dissolution during anodizing, those formed in the presence of sulphate showed the highest rate of post-anodizing dissolution in aqueous 10% KOH, while those formed in the presence of both had the expected combined properties.

(2) The metal-removal and oxide thicknesses were calibrated and shown to have values as given by eqs. 4.2 and 4.3. The oxide "thicknesses", actually weights, were about 20-25% higher than expected from metal-removal thicknesses. This is understandable in terms of the incorporation of electrolyte constituents into the anodic film, such as 5-10% of the O^{2-} in the film is replaced with SO_4^{2-} and HPO_4^{2-}.

(3) Depth distributions in Be showed the expected mixture of random and channeled stopping, whereas those in BeO showed random stopping alone. The latter is of interest in constituting an independent proof that anodic BeO is amorphous.

(4) The experiments undertaken here on the anodic sectioning of Be have been described in such a way as to emphasize a "logic", in so far as one exists. For example, a systematic effort was made to establish conditions under which an anodic film could be formed which is simultaneously barrier-type, stable, and amorphous. Also, the mechanism of film formation on Be, as will be seen in Chapter 6, involves cation

transport and from this one can understand why doping was possible, thence why the film chemistry could be controlled. These principles can be used as a guide for establishing anodic-sectioning procedures with still unstudied systems. We may point out that the problem of anodically sectioning Zr, which forms a barrier film in many electrolytes, lies in the difficulty of stripping the anodic film. This in fact can be understood in terms of the above principles. It will be seen in Ch. 6 that the mechanism of film formation on Zr involves anion transport, hence doping is not possible. Also, it will be seen in Ch. 7 that the anodic oxide films formed on Zr are invariably crystalline.

REFERENCES TO CHAPTER 4

1. J.L. Whitton and Hj. Matzke, Can. J. Phys., 44 (1966) 2905.
2. R. Kelly, J. Appl. Phys., 39 (1968) 5298.
3. J.A. Davies, J. Friesen and J.D. McIntyre, Can. J. Chem., 38 (1963) 1526.
4. M. McCargo, J.A. Davies and F. Brown, Can. J. Phys., 41 (1963) 1231.
5. J.A. Davies, G.C. Ball, F. Brown and B. Domeij, ibid., 42 (1964) 1070.
6. J.L. Whitton and J.A. Davies, J. Electrochem. Soc., 111 (1964) 1347.
7. R.E. Pawel, Rev. Sci. Instr., 35 (1964) 1066.
8. M.R. Arora and R. Kelly, J. Electrochem. Soc., 119 (1972) 270.
9. M.R. Arora and R. Kelly, ibid., 120 (1973) 128.
10. M.R. Arora and R. Kelly, Electrochimica Acta, 19 (1974) 413.
11. N.Q. Lam, S.J. Rothman and L.J. Nowicki, J. Electrochem. Soc., 119 (1972) 715.
12. N.Q. Lam, S.J. Rothman and L.J. Nowicki, ibid., 119 (1972) 1344.
13. M.A. Wilkins, Harwell (U.K.) Report AERE R5875 (1968).
14. T. Andersen and G. Sørensen, Rad. Effects, 2 (1969) 111.
15. J.L. Whitton, J. Appl. Phys., 36 (1965) 3917.
16. C. Jech, Phys. Stat. Sol., 27 (1968) 573.
17. N.Q. Lam and R. Kelly, Can. J. Phys., 50 (1972) 1882.
18. H. Lutz and R. Sizmann, Z. Naturforsch., 19a (1964) 1079.
19. R. Kelly, Can. J. Phys., 46 (1968) 473.
20. D. Gupta and R.T.C. Tsui, Appl. Phys. Letters, 17 (1970) 294.
21. R.E. Pawel and T.S. Lundy, J. Electrochem. Soc., 115 (1968) 233.
22. N.V. Sidgwick, "Chemical Elements and their Compounds", Oxford University Press, London (1951) Vol. I, 211.

23. W.D. Mackintosh, F. Brown and H.H. Plattner, J. Electrochem. Soc., 121 (1974) 1281.

24. D.V. McCaughan, R.A. Kushner and V.T. Murphy, Phys. Rev. Lett., 30 (1973) 614.

25. I. Reid and R. Kelly, Rad. Effects, 17 (1973) 253.

26. W.S. Johnson, J.I. Gibbon and S.W. Mylroie, Projected Range Statistics in Semiconductors and Related Materials, Second Ed. (John Wiley and Sons, Inc., 1975).

27. D. Powers and W. Whaling, Phys. Rev., 126 (1962) 61.

CHAPTER 5

PHOTON EMISSION FROM ION-BOMBARDED SOLIDS

5.1 Introduction

In the past decade, various techniques have been developed to determine the chemical composition of a solid surface and to measure as a function of depth the concentration of its constituents. A number of these techniques combine sputter-etching the specimen with the analysis of the sputtered material or of that left in the sample at different stages of erosion. These include Secondary Ion Mass Spectroscopy (SIMS) (1), Surface Analysis by Sputtered Neutrals (2), Auger Electron Spectroscopy (AES) (3) and X-ray Photoelectron Spectroscopy (ESCA or XPS) (4). In this work another technique has been used, that of analysing the optical radiation emitted by sputtered particles. This relatively new method has been called Bombardment-Induced Photon Emission by Kelly and Kerkdijk (5), SCANIIR i.e. Surface Composition by Analysis of Neutral and Ion Impact Radiation by White _et al._ (6) and ORSP i.e. Optical Radiation from Secondary Particles by Braun _et al._ (7).

The bombardment-induced photon emission has been and is being used to study the fundamental electronic processes resulting from collisions. On the other hand, it can be used to detect components of a surface by the identification of prominent lines and bands. White _et al._ (6) used it to analyse complex solids such as volcanic glass and tektite and to obtain quantitative information on very small quantities of organic liquids such as blood. They found the line intensities proportional to the absolute concentration of specific constituents and obtained detection sensitivities ranging from 0.6 ppm for sodium to 800 ppm for potassium using a 0.3 μA ion beam and a 10 s integration time. Depth analysis is also possible, for if the sputtering rate is known, measurements of intensity versus time yield the depth distribution of any specific impurity. Although damage to the sample is inevitable, it was found that the excitation efficiency could be maximized and damage minimized by using heavy ions at low energies and low current densities (8).

In this chapter we will discuss some aspects of the bombardment-induced photon-emission technique which are related to our interest in this work, that is the sputtering, analysis, and profiling of anodic-oxide films. First we will present a brief description of the experimental apparatus. Then we will discuss some details about the origin of emitted photons, the mechanism for production of excited states, competing mechanisms for de-excitation and the enhancement of photon yields in the presence of oxygen. Finally we will conclude the chapter by some remarks about the application of this technique to analysis and profiling anodic-oxide films.

5.2 Experimental Apparatus and Technique

The experimental apparatus to study bombardment-induced photon emission requires i) an Ion Accelerator that can produce a monoenergetic ion beam in the low-energy range, up to 20 keV and ii) a Photon Detector unit that can separate different wavelengths and select the one needed.

An apparatus which satisfies these requirements is used in this work. It can be described briefly as follows:

i) The Ion Accelerator

Fig. 5.1 shows the main parts of the (4-20 keV) ion accelerator used in the bombarding process. These are an RF ion source leading to the accelerator column and then the target chamber. The system is held at a base pressure of 5 x 10^{-5} Pa by two four-inch Edwards oil diffusion pumps each fitted with a liquid-nitrogen trap. However, the operating pressure lay in the vicinity of 1 x 10^{-4} Pa while the pressure of the gas fed into the ion source was held at about 14 Pa. The gas can be any of Kr, Ar, Ne, Xe, N_2, O_2 or H_2. For most of this work Kr was used which was purified by a liquid-nitrogen trap at the gas inlet, although it has an additional purification by virtue of its source being the vapour above solid krypton at 77 K.

The ion source is an RF type (77 MHz). After the discharge, an extraction voltage of 4 keV forces the positive ions through the extraction canal into the main column of the accelerator. A magnet coil at the bottom of the discharge tube helps to concentrate the plasma at the extraction canal.

The accelerator column path is about 70 cm, with three ion focusing systems, two quadrupole deflectors and a Wien filter. Each focusing system is of the Einzel type, consisting of five equally spaced circular electrodes held at potentials, 0, +, +, +, 0. This acts as a double convex lens to focus the beam. The quadrupole deflector plates are used to keep the ion path along the column axis. The Wien filter is used to

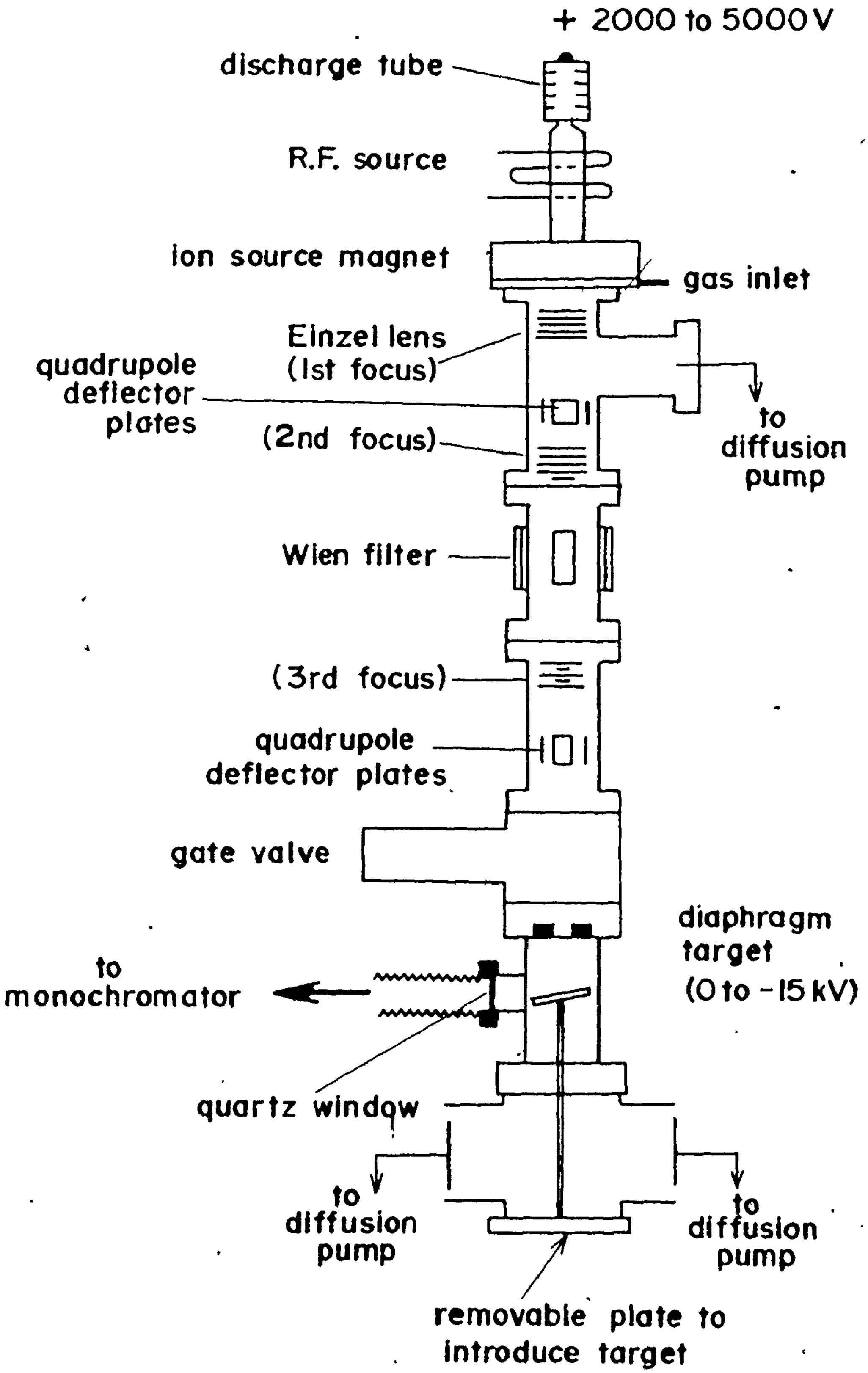

Fig. 5.1. Schematic of the ion accelerator.

mass separate the beam by an electric field normal to a magnetic field, both normal to the ion trajectory. Thus for a particle with charge q and velocity v, the electric force is $q\vec{E}$, the magnetic force is $q\vec{v} \times \vec{B}$, and the forces balance when $v = E/B$. Thus, the mass separation is affected through the dependence of the magnetic force on the velocity which, in turn, is inversely proportional to the square root of the mass.

The target chamber begins with a diaphragm to define the beam to an area of 0.28 cm^2 as well as to allow higher vacuum in the target chamber than in the upper column. The target, which is inclined 2° to the beam, is subjected to 0-12 keV negative potential to accelerate the ions so that the total energy is 4-16 keV. A Faraday cage above and below the target was maintained at 400-800 v negative with respect to the target in order to suppress any secondary electrons sputtered from the target and hence allow a reasonably accurate measurement of the beam current, which reaches up to 15 μA,

ii) Photon Detection

Two sets of photon detection units are connected to the ion accelerator. Such a facility enables two different constituents to be traced simultaneously during sputter profiling of the target. Each photon detection unit mainly consists of a monochromator that is coupled to a photomultiplier tube, then to a count-rate meter which is connected to a two-channel chart recorder.

Photons are detected at right angles to the incident ions through a quartz window to the monochromator to separate the different wavelengths and select the needed wavelength. Since quartz effectively absorbs all photons of wavelengths less than 200 nm, the range of study was limited. For example, it was not possible to detect the main oxygen photons because of their low wavelengths. The monochromator, a Jarrell-Ash 82-410, has a resolution of 0.3 nm at 313 nm with 150 μm entrance and exit slits. However, for depth profiling when a particular wavelength was followed with time the entrance slit was changed to 500 μm slit to give higher intensities and thus better statistics. The photomultiplier tube, an EMI 9789 QB, was kept at -30°C with a refrigerated housing which helps in decreasing the background of the spectrum. For more amplification the current leaving the photomultiplier tube is further amplified by a model 1140 C (Princeton Applied Research Corp.) pre-amplifier. Finally comes a 1140 A (P.A.R. Corp.) quantum photometer (i.e., count-rate meter) to convert the counts into current to be graphed by a Rikadenki two-pen chart recorder.

5.3 Origin of Photon Emission

The origin of photon emission during the ion bombardment of a target is basically understood in terms of radiative de-excitation. Most of the literature agrees (5,7,9-15) in attributing the photon emission to excited atoms, ions and molecules of both backscattered beam and sputtered target species. More particularly, four distinctive types of radiation were observed due to ion bombardment of a target. These are

1) radiation of discrete lines from excited states of sputtered target atoms and ions;
2) similar radiation from excited molecules;
3) radiation from excited states of backscattered beam particles; and,

4) a broad continuum which is emitted by some but not all targets (8), probably due to unresolved sputtered molecules (15,16).

Since the target surfaces were sufficiently clean to eliminate such molecules as BeH, since heavy ions, as used in this work, tend not to backscatter, and since beryllium is not one of the targets which yield a continuum (cf. Fig. 6.1), it is the first type of radiation which constitute our primary interest in this work, radiation of discrete lines.

The spectral analysis of the discrete radiation showed that they tend to have a slight Doppler broadening. This, in fact, is used to indicate that the excited particles are in free space, unaffected by the nearby surface (7). On the other hand, as argued by Veje (12,15), the mean radius of a highly excited atomic orbit is about 10-100 Å whereas the average distance between two neighbouring atoms in a solid is around 1 Å. Therefore, the excitation to a highly excited state cannot take place inside the solid but must happen either while the sputtered particle crosses the surface, or after it has passed. This, in fact, not only attributes the emission to sputtered species, but also suggests the excitation to occur on the surface or outside it.

Independently of Doppler broadening and the size argument, it has been shown experimentally that the radiation occurs several millimeters in front of the target (18), as shown in Fig. 5.2, giving rise to a luminous strip above the area of impact with no contribution from within the target itself (9,11). In addition, it has been shown that photon yields have an exponential decay with the distance from the target, Fig. 5.3 (ref. 19). However, even though the average energy of the sput-

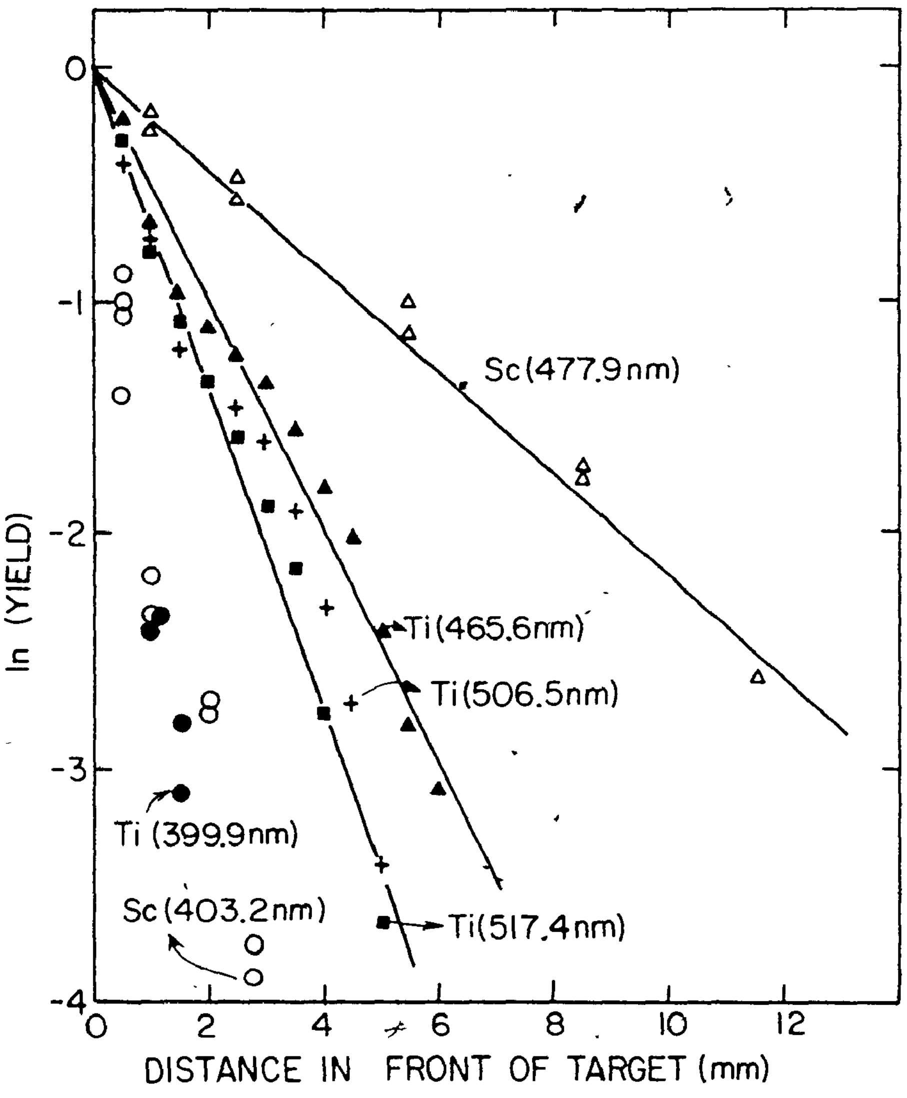

Fig. 5.3 ℓn yield vs. distance plot for lines of Sc and Ti spectrum (from reference 19).

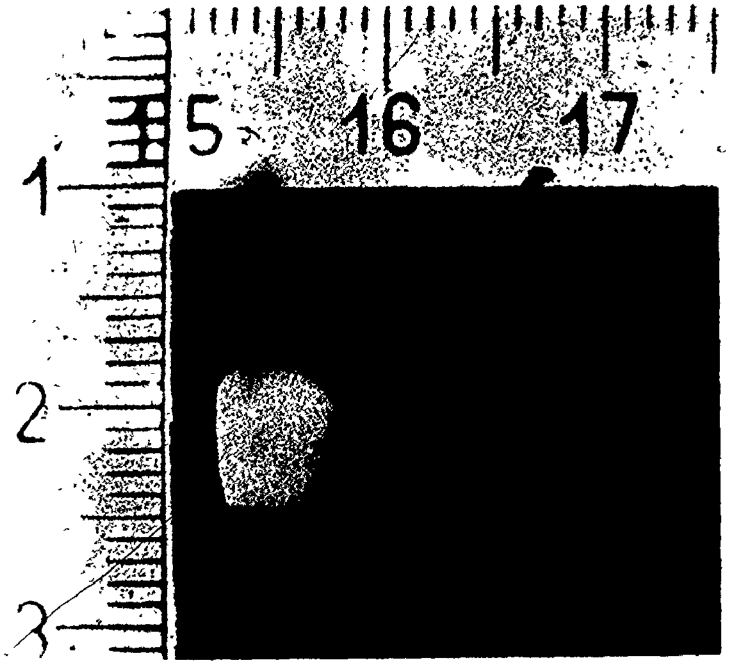

Fig. 5.2 Photograph showing the light emission when Tm target was bombarded with 230 KeV Xe^+ ions. The incident ion beam comes from the right. The light is visible over a distance of 1 cm (from reference 18).

tered particles is of the order of 10 eV (20), the Doppler profile indicates that the light-emitting particles have energies in the keV range. This discrepancy is believed to occur because of radiationless de-excitation processes competing with photon emission and, in general, dominating for the lower energy particles. These processes will be discussed in more detail in sec. 5.5 after we discuss the mechanisms for producing excited states in the following Section.

5.4 Mechanisms for Production of Excited States

The mechanism of production of excited states due to ion bombardment of a target is still not settled. However, various models have been proposed by various authors to explain how these excited states could be produced during ion bombardment. These include i) the thermal excitation model (21), an extension of the theory of secondary ion production (22), ii) resonant neutralization (23) based on the electronic exchange processes to particles near the solid surface.

Other models that have been discussed are those based on the interaction between sputtered particles and the beam (unfavourable (24)) and on charge exchange during the collision of an incoming ion with a surface atom (25). In addition, Blaise (26) has devised a model in which the surface of an oxygen-covered metal such as Al is assumed to resemble a diatomic molecule correlating with ions. Sputtering of metal atoms then, in effect, causes a molecule to trace out its potential curve and thus intersect (27) the potential curves of molecules of the same composition but which correlate with ground state or excited atoms. The necessary oxygen is always present on a metal surface under normal bombarding conditions (5).

A brief review will be given here for the first two models, the thermal excitation model and the resonant neutralization model, together with some details of the electronic exchange processes to particles near the surface. These, in fact, account for many details concerning photon yields and serve an important practical purpose in analysis and profiling, which is our primary interest here.

5.4.1 The Thermal Excitation Model

Various authors have discussed the phenomena of the thermal spike, in which the energy deposited beneath a solid surface by an incident ion is assumed to cause a high temperature to exist for a short time in the region of ion impact. Some (22,28-33) have suggested that one of the consequences of high temperature is an ionization equilibrium within the solid:

$$A^\circ \rightleftarrows A^+ + e \qquad (5.1)$$

Such ionization was proposed to account for the presence of ions amongst sputtered particles. The consequence is that the ion yield is proportional to exp(-I/kT), where I is the ionization energy. The writer, along with Good <u>et al.</u> (21), have extended the model to the case where excitation but no ionization is involved, the relevant equilibrium being:

$$A^\circ \rightleftarrows A^* \qquad (5.2)$$

Here, "*" denotes excitation and "°" denotes ground state.

They pointed out that this equilibrium would probably be incomplete within the target because of the large size of A*, though such an objection would not apply at or in front of the surface. When equilibrium prevails, the normalized probability of species A being in an excited state, A*, which lies ε_i above ground state is

$$P(\varepsilon_i) = (\omega_i/Q)\exp(-\varepsilon_i/kT) \tag{5.3}$$

where ω_i is the degeneracy of the energy state and Q is the internal partition function. The degeneracy can be taken as (2L + 1) provided the yields for states differing only in J are combined. The problem of evaluating Q is circumvented when a single substance is being studied.

The above relation has been found to correlate a large body of data on photon yields and, moreover, does so by requiring temperatures in the range 3600-5900 K. A similar range of temperatures is also deduced in work on the assumed thermal sputtering of oxides (34,35), the assumed thermal sputtering of metals (36,37), the assumed role of thermal sputtering in causing stoichiometry change (34,35), and the formation of secondary ions (22,28-33).

However, as mentioned above, the thermal excitation model in its simplest form entails an objection which does not apply to thermal ionization: atomic states with large quantum number n are much too large to be accomodated within a solid target. For excitation occurring in front of the surface, a further objection would appear to arise, namely that a thermal process is physically impossible. However, Coles (38) has recently reviewed surface ionization and points out that interactions which take place outside a target surface can involve collisionally sputtered atoms plus thermal electrons and would accordingly be characterized by a true temperature, the electron temperature.

Notwithstanding the above reservations, the thermal excitation model accounts for many of the details of the excited-state production. It also serves an important practical purpose concerning photon yields and the application of the photon-emission technique in analysis and profiling as discussed in Chapter 6: this is to indicate which photons will dominate with any given target.

5.4.2 The Resonant Neutralization Model

Electronic transitions can occur between an atomic species (atom, ion or molecule) and a solid as the particle approaches or recedes from the surface. If the atomic species are excited or ionized, they can interact with the surface to de-excite or to be neutralized by two kinds of processes; one-electron resonance processes and two-electron Auger processes. Hagstrum (23) symbolized these processes in a "triangle" of processes, Fig. 5.4. The triangle links the three states, $A^+ + ne_M^-$, $A^* + (n-1)e_M^-$ and $A° + (n-2)e_M^- + e^-$ where A° and A* signify, as defined before, atoms in normal ground states and excited states, respectively, A^+ signifies a singly charged ground ionic state, ne_M^- indicates n electrons resident in a metallic band, and e^- stands for a free electron. Note that the top of the triangle represents the first group of processes that are characterized by an electron transfer at constant energy from the solid to atomic ion or in the converse sense. On the other hand, the sides of the triangle represent the second group of processes, Auger type. In these processes, two electrons simultaneously make transitions

$$\begin{tikzcd}
A^{+} + ne_{M}^{-} \arrow[rr, shift left, "\text{RESONANCE NEUTRALIZATION}"] \arrow[dr, swap, "\text{AUGER NEUTRALIZATION}"] & & A^{*} + (n-1)e_{M}^{-} \arrow[ll, shift left, "\text{RESONANCE IONIZATION}"] \arrow[dl, "\text{AUGER DE-EXCITATION}"] \\
& A^{\circ} + (n-2)e_{M}^{-} + e^{-} &
\end{tikzcd}$$

Fig. 5.4. Triangle of resonant and Auger processes which occur at a solid surface due to the proximity of slowly-moving ionized, excited, or neutral atoms (23). "e_M^-" means an electron in the solid.

involving equal energy change, one electron gaining the energy lost by the other.

The above processes could be explained based upon a model of two independent potential systems (23,39), namely the electron energy diagram of the solid and the potential energy diagram of the atom, shown schematically in Fig. 5.5 (23). The metal is represented by a sommerfeld potential box of depth W filled with n electrons to the Fermi level. The work function ϕ is the minimum energy required to raise an electron to the energy continuum of free space. The atomic energy well is shown to the right, being basically just $e^2/4\pi\varepsilon_0 r$. The ionization potential of the atom I is measured from the vacuum level to the electronic ground state. The ground state can be excited by ε_i to occupy an excited state.

Let us consider the resonance neutralization process which is of particular interest here as it produces excited states; the other two processes will be considered in sec. 5.5.2. This process is represented by transition 1 in Fig. 5.5, which indicates the tunneling of a metallic electron across the energy barrier to settle into the atomic potential well. Such a transition yields an excited neutral atom:

$$A^+ + e^- \rightarrow A^* \qquad (5.4)$$

and in order for neutralization to take place, the energy level of the electron in the metal must coincide within narrow limits with that in the atom, i.e., resonant neutralization can take place only when,

$$W > I - \varepsilon_i > \phi \qquad (5.5)$$

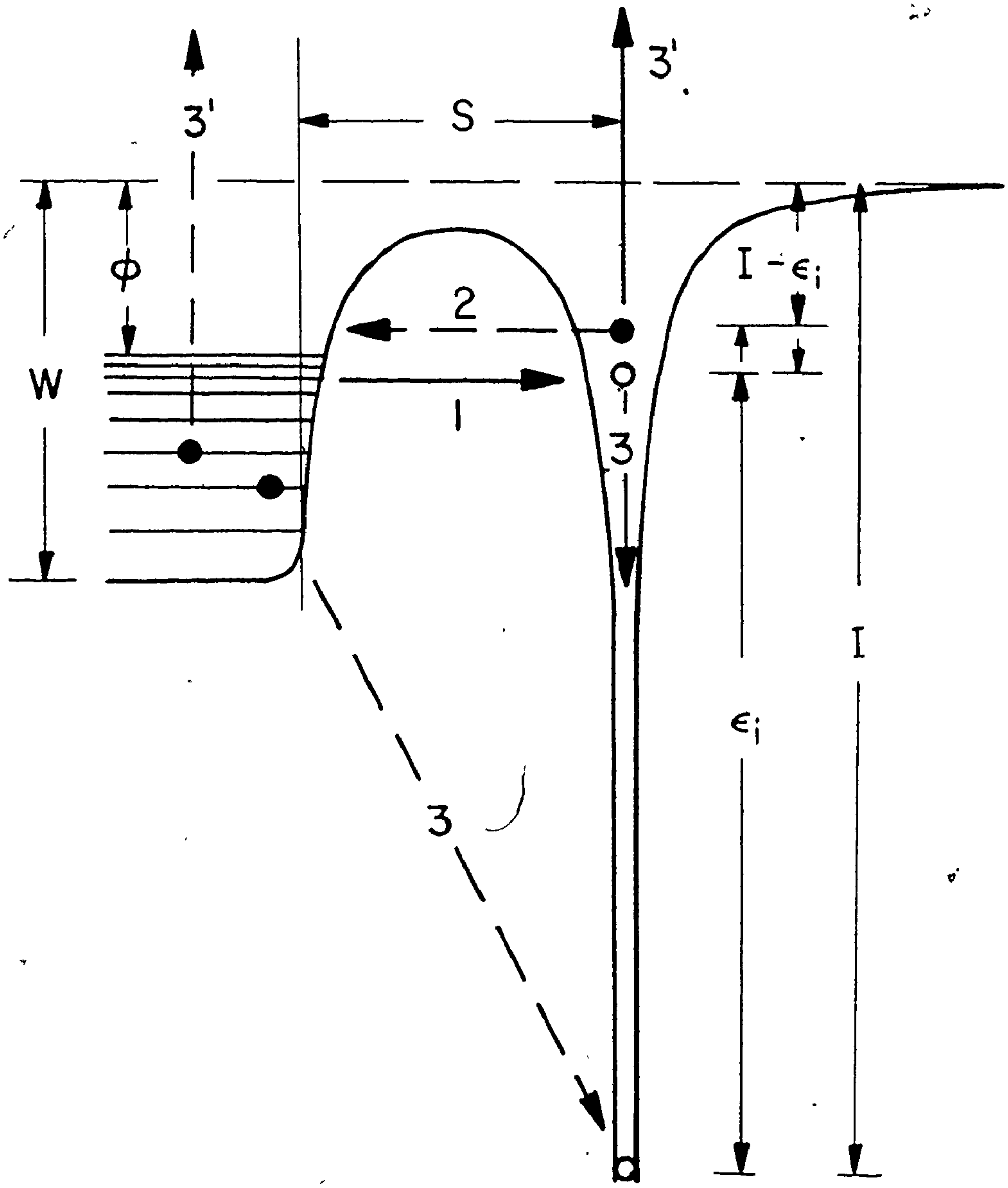

Fig. 5.5. Electron energy diagram illustrating resonant neutralization to an excited atomic state (transition 1), resonant ionization of a filled, excited atomic state (transition 2), and Auger de-excitation processes of a filled, excited atomic state (transitions 3 and 3') (31).

It has been demonstrated in channeling experiments with single crystals (40) that photon emission occurs with particles that emerge from the solid from a depth appreciably larger than one atomic layer. Thus particles can only get excited when leaving the surface as we tend to exclude the possibility that they are excited inside the solid and retain their excitation on the outward path. Excited particles are too large to be accomodated within the solid. It should be pointed out that the atomic lines showed shallower minima than ionic lines in these channeling experiments, revealing that the relevant particles originated on the average from a larger depth than emitting ions. These results lead to the conclusion that, after collision, the particles emerge from the solid in a state of excitation or ionization depending on their velocity at the point of exit. Slower particles coming from deeper tend to be neutral, whereas faster particles have a higher chance to be ionized.

5.5 Destruction of Excited States

The excited particles leaving a solid surface can de-excite by photon emission or by the competing nonradiative processes. These competing processes result from the interaction between the particles and the solid surface and are generally of two types: resonant type and Auger type as mentioned in sec. 5.4.2. These nonradiative processes, if energetically allowed, are significantly more efficient than radiative de-excitation (life-time for radiative de-excitation about 10^{-8} s, whereas for resonant and Auger processes about 10^{-14} s, 10^{-16} s, respectively); this can result in a substantial decrease in the photon yields due to ion-bombardment. Therefore, both the photon emission and the competing nonradiative processes will be considered in the following subsections.

5.5.1 Radiative De-excitation

As mentioned earlier, sec. 5.3, the emitted light during the bombardment process has been observed to extend to several millimeters above the target surface. The intensity of this emitted light is found to be dependent on the distance from the target (10,18,19), such that the logarithm of the intensity is inversely proportional to the distance, as shown in Fig. 5.3 (19). Such dependence in fact suggests a lifetime process. If the lifetime of the decaying process is τ, then at time t the probability of radiative de-excitation is $\exp(-t/\tau)$, and if we substitute for $t = \frac{s}{v}$, where s is the distance from the target surface and v is the particle velocity, then (18):

$$I(s) = I_0 \exp(\frac{-s}{v\tau}) \tag{5.6}$$

where I_0 is the intensity at the target surface. The average lifetime for this radiative de-excitation process is in the order of 10^{-8} s (42). Therefore, the emission of light will be the most probable process only if there is no faster de-excitation path.

5.5.2 Nonradiative De-excitation

Consider an excited atom a small distance "s" from the surface of a metal as shown in Fig. 5.5. If the excited state is above the Fermi level of the metal (position 2) the electron may tunnel directly into the metal; this is resonant ionization. If, however, the excited state is below the Fermi level (position 1) the atom, if it de-excites, is forced to undergo an Auger process in which 3 drops to ground state of the atom and 3' is ejected or vice versa. The transition rate as a function of distance, s, for either the Auger process or the resonant ionization has been approximated by (9,42,43):

$$P(s) = A \exp(-as) \tag{5.7}$$

where "A" is the radiationless transition rate at the surface and "a" is a parameter that follows from the radial part of the atomic wave function which determines the overlap of atomic and metallic wave functions (9) ($A \sim 10^{14} - 10^{15}\ s^{-1}$ and $a \sim 2 \times 10^{8}\ cm^{-1}$ (9,42)). From eq. (5.7) it follows that the probability R that an excited atom will escape from the surface and subsequently radiate a photon is given by

$$dR/dt = -P(s)R;$$

$$R = \exp(-A/av_{\perp}) \tag{5.8}$$

where $v_{\perp}$ is the velocity component of the sputtered atom normal to the surface. Thus, the probability of escape from the surface as an excited atom increases exponentially as the velocity component of the sputtered particle normal to the surface increases. Therefore, it is not surprising that it is the fast particles which contribute more efficiently to the observed radiation, when the nonradiative de-excitation processes are energetically allowed. This will be considered in more detail in the following section.

5.6 Enhancement of Photon Emission from Oxides

It has been reported by many authors (5,13,14,41) that the excitation efficiency or photon yield per incident ion is much greater at an oxide surface, up to 3 orders of magnitude , than at a metal surface. This has been repeatedly explained through the band-structure model. The argument is that excitation tends to be in general of high probability amongst sputtered particles but the survival of this excitation depends on whether the band structure of the target prevents radiationless de-excitation by resonant electron transfer, Fig. 5.6. An excited particle leaving a metal surface will often have an electron with potential energy lying opposite the conduction band of the metal. De-excitation can occur by tunneling, so that the excitation survives only when the particle is fast enough. An excited particle leaving an insulator surface, on the other hand, will often have an electron with potential energy lying opposite a large forbidden gap, making the resonant process impossible because of the lack of available vacant states. Only Auger processes would be possible, but these are inherently slow. Thus, both fast and slow particles survive resonant electron transfer and emit photons. Although this model appears to apply only to excited neutral atoms and ground-state ions, within this limitation particularly strong support comes from the information given in Fig. 5.7, taken from the work of White _et al._ (41). Not only is the photon yield higher from the insulator (SiO_2) than the metal (Si), but the Doppler broadening is such as to suggest that excitation survives only with fast particles in the case of the metal but with fast and slow particles in the other case.

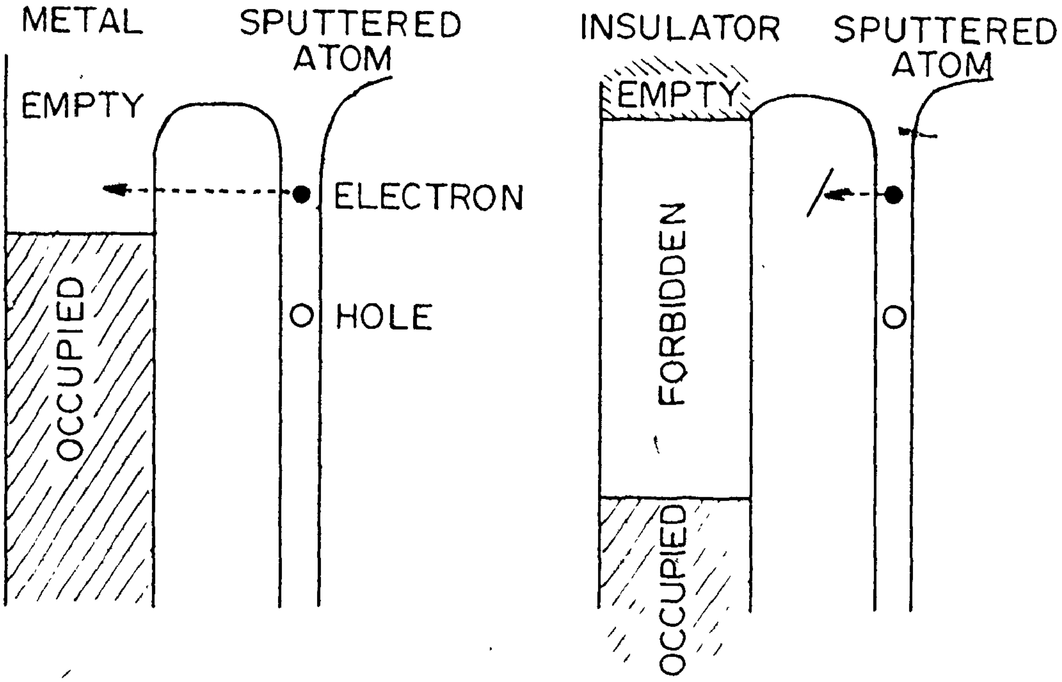

Fig. 5.6. Schematic potential-energy diagrams for an excited atom near a metal and near an insulator. Electronic transitions can take place as shown between the sputtered atom ~~and~~ the metal but not between the sputtered atom and the insulator.

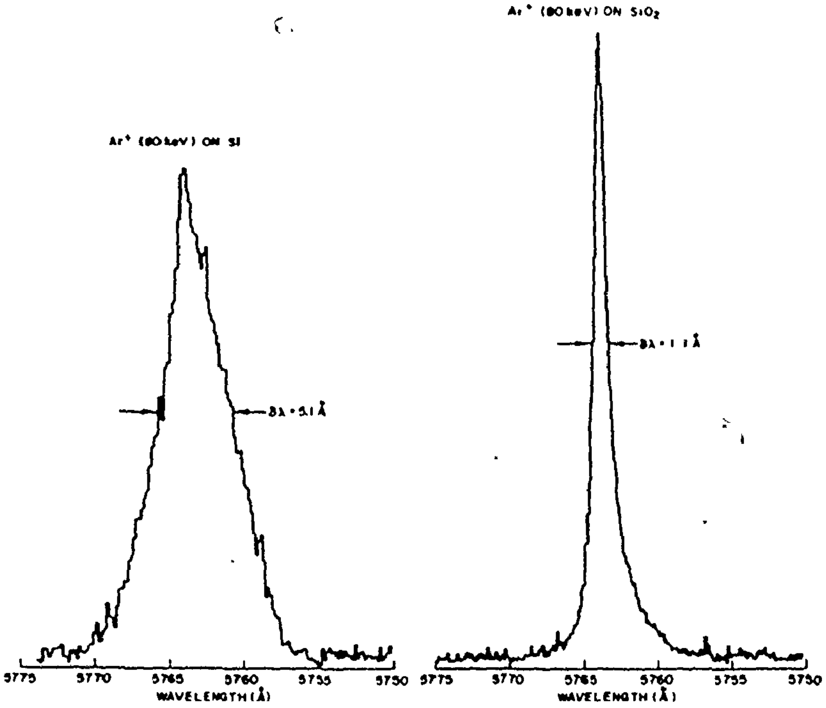

(a) (b)

Fig. 5.7. Si I photon profiles at 288.2 nm from Si and SiO_2 as measured by White et.al. (41). We note that the Doppler broadening is such as to suggest that an excited electron survives only with fast particles in the case of the metal but with both fast and slow particles (but mainly the latter) in the case of the oxide.

It should be pointed out that the enhancement of photon yields has also been noted by Kelly and Kerkdijk (5) and Thomas and de Kluizenaar (11) when a clean metal was bombarded either with oxygen or in the presence of oxygen in the rest gas. Both investigations again point to the band-structure model to explain the enhancement. The distinction between pure oxide and metal is clear, but even in the case of oxygen adsorbed on metal it has been found that the photon yield is proportional to the surface coverage of oxygen, i.e., $I \propto \theta_\infty$ where θ_∞ is the steady-state surface coverage (5). The oxygen enhancement is believed to occur due to local oxide-like band structure in the vicinity of each oxygen atom rather than an average band structure. Benninghoven (44) emphasized that it was the site of origin of a secondary ion rather than the average electronic structure which governed resonance processes. Thus an atom originating from a site next to an oxygen atom would behave as if from an oxide, resulting in a photon intensity proportional to oxygen coverage. In fact, this is found to be true in work on nickel covered by greater than 0.5 monolyers (45), where chemical shifts of the valence and core spectra of both nickel and oxygen indicated nickel-oxide type behaviour despite the oxide layer being incomplete.

5.7 Concluding Remarks for Analysis and Profiling by Photon Emission

(1) During ion-bombardment of a target, photons are emitted with discrete energies characteristic of the sputtered particles. The surface constituents can thus be determined by the identification and analysis of the optical lines and bands that are produced from these sputtered particles during the bombarding process. The photon emission technique

is a very sensitive probe for the surface region since low bombarding energies and heavy ions are used, and since the sputtering as well as excitation occur at the surface. In addition, as surface atoms are being continuously removed by the impinging ion beam, measurements made as a function of bombardment time can be used to provide depth-profile information.

(2) The mechanisms of light emission under heavy-ion bombardment are generally considered to involve two processes: the process of producing a sputtered excited particle and the process involving radiative de-excitation of that particle. Both processes are found to be significantly affected by the various electronic transition processes that may take place between a sputtered particle and a solid surface. These processes are mainly of two types: resonant type or Auger type. For example, excited states can be produced by the resonant neutralization process and, on the other hand, de-excitation by resonant and Auger processes are found to be highly competing processes with radiative de-excitation.

(3) An important feature that has emerged from the thermal excitation model is that photon yields tend to decrease as the energy of the upper level, ε_i, increases. In most cases studied, the yield is found to be describable as if thermal equilibrium is involved:

$$\text{Yield} \propto (2L + 1) \exp(-\varepsilon_i/kT)$$

A practical consequence of this in the analysis and profiling by the photon-emission technique is that for elements having low lying excited states the photon yields are significant. For this reason, as will be shown in the next chapter, high photon yields are obtained with Al, B, Be and Zr but not with O, P and S.

(4) Photon yields are generally higher from oxides than metals. This has been explained by the band-structure model which assumes that the forbidden bands of the oxide form barriers to resonant electronic transitions, making radiative decay the dominant de-excitation mechanism near the oxide surface. A practical consequence of yields being higher from oxides is that oxide films can be profiled in spite of the lack of a useful oxygen signal. This, in fact, enabled us to profile the anodic oxide films, which is of primary interest in this work.

REFERENCES TO CHAPTER V

1. A. Benninghoven, Surface Sci., 35 (1973) 427.
2. H. Oechsner and W. Gerhard, Phys. Lett., 40A (1972) 211.
3. P.W. Palmberg, J. Vacuum Sci. and Tech. 9 (1972) 160.
4. K.S. Kim, W.E. Baitinger, J.W. Amy and N. Winograd, J. Electron Spectrosc., 5 (1974) 351.
5. R. Kelly and C.B. Kerkdijk, Surface Sci. 46 (1974) 537.
6. C.W. White, D.L. Simms and N.H. Tolk, Science, 177 (1972) 481.
7. M. Braun, B. Emmoth and R. Buchta, Radiation Effects, 28 (1976) 77.
8. N.H. Tolk, D.L. Simms, E.B. Foley and C.W. White, Rad. Eff., 18 (1973) 221.
9. W.F. van der Weg and D.J. Bierman, Physica, 44 (1969) 206.
10. H. Kerkow, Phys. Stat. Sol. (a), 10 (1972) 501.
11. G.E. Thomas and E.E. de Kluizenaar, Vide, 176 (1973) 190.
12. K. Jensen and E. Veje, Z. Physik, 269 (1974) 293.
13. W. F. van der Weg and E. Lugujjo, Atomic Collisions in Solids, Vol. II, ed. S. Datz, B.R. Appleton and C.D. Moak (Plenum, New York, 1975) p. 511.
14. T.S. Kiyan, V.V. Gritsyna and Ya. M. Fogel, Nucl. Instr. and Methods 132 (1976) 435.
15. B. Dynefors, I. Martinson and E. Veje, Physica Scripta, 13 (1976) 308.
16. C.B. Kerkdijk, K.H. Schartner, R. Kelly and F.W. Saris, Nucl. Instr. and Methods 132 (1976) 427.
17. C.W. White, N.H. Tolk, J. Kraus and W.F. van der Weg, Nucl. Instr. Meth. 132 (1976) 421.

18. M. Braun, B. Emmoth and I. Martinson, Physica Scripta, 10 (1974) 132.

19. M.R. Morrow, O. Auciello and R. Kelly, submitted to Surface Science.

20. I.S.T. Tsong, Phys. Stat. Sol. (a), 7 (1971) 451.

21. C.J. Good-Zamin, M.T. Shehta, D.B. Squires and R. Kelly, Rad. Eff. 35 (1978) 139.

22. C.A. Andersen and J.R. Hinthorne, Anal. Chem., 45 (1973) 1421.

23. H.D. Hagstrum, Physics of Ionized Gases, Lectures at the Summer School, Herceg-Novi, Yugoslavia (1970) 190.

24. J.M. Fluit, L. Friedmann, J. van Eck, C. Snoek and J. Kistemaker, Proc. Fifth Int. Conf. on Ionization Phenomena in Gases (North-Holland, Amsterdam, 1962), p. 131.

25. I. Terzić and B. Perović, Surface Sci., 21 (1970) 86.

26. G. Blaise, Surface Sci., 60 (1976) 65.

27. C. Zener, Proc. Roy. Soc. of London, A137 (1932) 696.

28. R. Shimizu, T. Ishitani, T. Kondo and H. Tamura, Anal. Chem. 47 (1975) 1020.

29. F.G. Rüdenauer, W. Steiger and H.W. Werner, Surface Sci., 54 (1976) 553.

30. A.E. Morgan and H.W. Werner, Anal. Chem. 48 (1976) 699.

31. D.S. Simons, J.E. Baker and C.A. Evans, Anal. Chem., 48 (1976) 1341.

32. J.M. Schroeer, J. Vac. Sci. Tech., 14 (1977) 343.

33. P.J. Martin and R.J. MacDonald, Surface Sci., 62 (1977) 551.

34. T. Parker and R. Kelly, Proc. 3rd Int. Conf. on Ion Implantation in Semi-Conductors and Other Materials (Plenum, New York, 1973), p. 551.

35. R. Kelly, Proc. Int. Conf. on Phys. Met. of Reactor Fuel Elements (The Metals Soc., London, 1974), p. 275.

36. R.S. Nelson, Phil. Mag. 11 (1965) 291.

37. R.S. Nelson, J. Nucl. Mat. 18 (1966) 348.

38. J.N. Coles, Surface Sci. 55 (1976) 721.

39. L.J. Varnerin, Jr., The Physical Rev. 91 (1953) 859.

40. W.F. van der Weg, N.H. Tolk, C.W. White and J.S. Kraus, Private communication.

41. C.W. White, D.L. Simms, N.H. Tolk and D.V. McCaughan, Surface Sci. 49 (1975) 657.

42. H.D. Hagstrum, Phys. Rev. 96 (1954) 336.

43. C.W. White and N.H. Tolk, Phys. Rev. Letters 26 (1971) 486.

44. A. Benninghoven, Phys. Lett., 32A (1970) 427.

45. P.R. Norton and R.L. Tapping, Disc. Faraday Soc. (1975).

CHAPTER 6

SPUTTERING, ANALYSIS AND PROFILING OF ANODIC FILMS BY THE PHOTON-EMISSION TECHNIQUE

6.1 Introduction

During the anodization of metals, electrolyte components like B, P and S are known to become incorporated into the anodic films. We mentioned earlier in Chapter 4 that this incorporation is, in fact, one of the key points that could be used to aid the successful stripping of the anodic films, hence to establish a microsectioning technique. Up to this point, we have only inferred the presence of these components in the anodic films on Be from the gravimetric calibrations, Sec. 4.4.2, and from their effects on the etching rates of the films, Sec. 4.2.2, in addition to the $\frac{dV}{dt}$ criterion for doping, Sec. 4.3. In this chapter we will attempt to investigate this by a more direct means, i.e. to study the presence and the distribution of the incorporated species in anodic films formed on Be by employing the photon-emission technique.

The presence, and in some cases, the distribution of material incorporated from the electrolyte has been noted for Ta (1-8), Nb (3) and Al (9). The distributions were reported to be non-uniform, such that the inner part of the film, next to the metal, was almost pure oxide whereas the outer part contained the material from the electrolyte. In addition, this two-layer structure of an anodic film has been related, in some cases, to the mechanism by which the film is formed, namely to the cation transport number. Results include the value 0.46 ± 0.05 for Ta (3,8), ∿ 0.5 for Nb (3) and 0.77 ± 0.03 for Al (9). Most of the results have been obtained by a depth-profiling procedure that involved chemical sectioning combined with radiotracer methods (2-7, 9). This approach may in fact provide uniform removal of the anodic oxide layer, although great care is needed if reproducible sectioning rates are to be achieved for both the inner and outer layers of a film that is generally limited to a few hundred nanometers in thickness.

In this chapter, the results for profiling anodic-oxide films on Be as well as Zr and Al, as test cases, will be presented. The profiling technique which was used is based on sputter etching combined with detecting the secondary photons that are emitted from the sputtered particles. (It will be noted that there should be no problem with preferential sputtering in the case of BeO, Al_2O_3, and ZrO_2 (10), as they have no lower oxides.) First, we will present some results for the spectral distribution and yields of the emitted photons that were observed during the bombardment of Be and BeO films and for the sputtering rates for BeO and ZrO_2. Then, we will present results for the profiles of the incorporated B, P and S in the anodic films. Finally, these results will be related to the mechanism of anodic-film growth on Be, Al and Zr, including estimates of the cation transport numbers and comparisons with the defect structure and self-diffusion mechanism in the oxide.

6.2 The Spectral Distribution and Yields of Emitted Photons

The spectra observed during the bombardment of beryllium and beryllium oxide consist basically of discrete, well defined lines. Fig. 6.1 shows a typical scan from 200-400 nm of 12 keV Kr ion on Be. The features have been identified using spectral tables (11,12), and the results are summarized in Table 6.1. It should be noted that transitions of low-lying excited states are found to be strongly excited, for example 2p $^1P°$ (234.9 nm) and 3s ^3S (332.1 nm), whereas transitions from higher-lying excited states are found to be relatively weaker, for example 5d ^3D (205.6 nm) and 5d ^1D (351.6 nm). Moreover, when the logarithm of (yield/w), where w is the degeneracy, is plotted against the energy of the excited state, shown in Fig. 6.2, a straight line relationship is obtained implying that relation 5.3 is followed. The resulting slope of the line is found to infer a temperature of 4050 ± 350 K in accord with the prediction of the thermal-excitation model (3600-4600 K), sec. 5.4.1. More interesting is that the photon yields from the oxide, as shown in Table 6.1, are found to be much higher than those from the metal. This in fact indicates that the vacuum conditions of the present work, though far from being exceptional, are at least acceptable. More important, however, is that such oxygen enhancement of photon yields enabled us to profile anodic films on both Be and Zr in spite of the lack of a useful oxygen signal.

6.3. Sputtering Rates of Anodic-Oxide Films on Be and Zr

Consider a thin oxide film formed on Be and let us make use of the oxygen enhancement of photon yields for profiling this oxide film as shown in Fig. 6.3. At the left the BeI (234.9 nm) photon yield

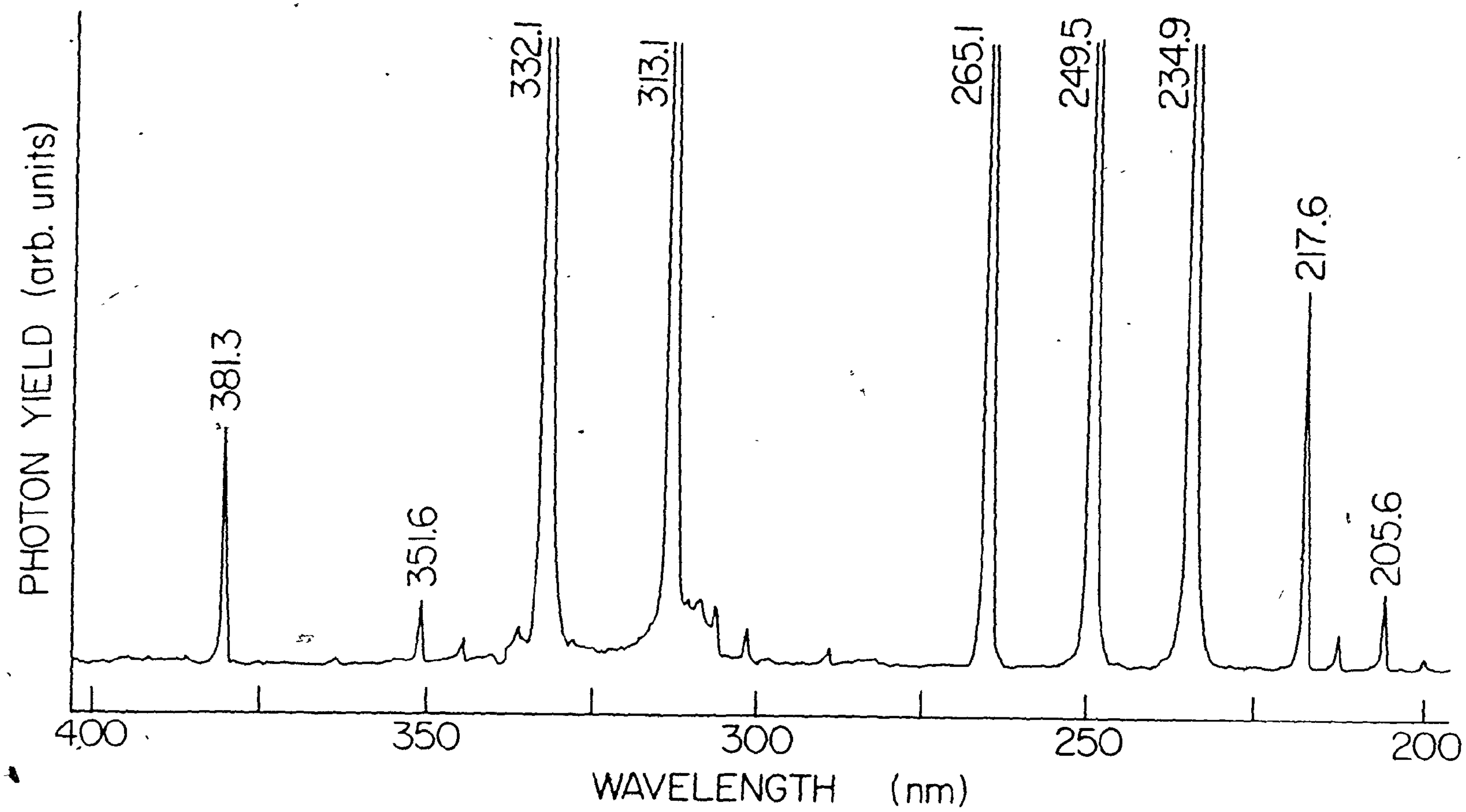

Fig. 6.1. Spectrum resulting when a Be target is bombarded with 12 keV Kr^+.

TABLE 6.1: The principal photons and their yields observed in the region 200-400 nm when Be and BeO anodic film are bombarded with 12 keV Kr$^+$.

Wavelength (nm)	Yield (counts/s)		Transition (lower - upper)	Degeneracy w_i	Energy of upper state in eV
	Metal	Oxide			
205.6	130	500	5d $^3P^\circ$ - 5d ^3D	5	8.75
217.6	590	1400	4d $^3P^\circ$ - 4d ^3D	5	8.42
234.9	21,000	71,000	2p ^1S - 2p $^1P^\circ$	3	5.28
249.5	6,500	31,200	3d $^3P^\circ$ - 3d ^3D	5	7.69
265.1	4,900	16,200	$2p^2$ $^3P^\circ$ - $2p^2$ ^3P (doubly excited)	3	7.46
313.1	15,000	59,000	2p ^2S - 2p $^2P^\circ$ (Be II)	-	3.96
332.1	44,000	198,000	3s $^3P^\circ$ - 3s ^3S	1	6.46
345.5	60	190	$2p^2$ $^1P^\circ$ - $2p^2$ ^1S (doubly excited)	1	8.86
351.6	120	490	5d $^1P^\circ$ - 5d ^1D	5	8.80
381.3	480	2160	4d $^1P^\circ$ - 4d ^1D	5	8.53

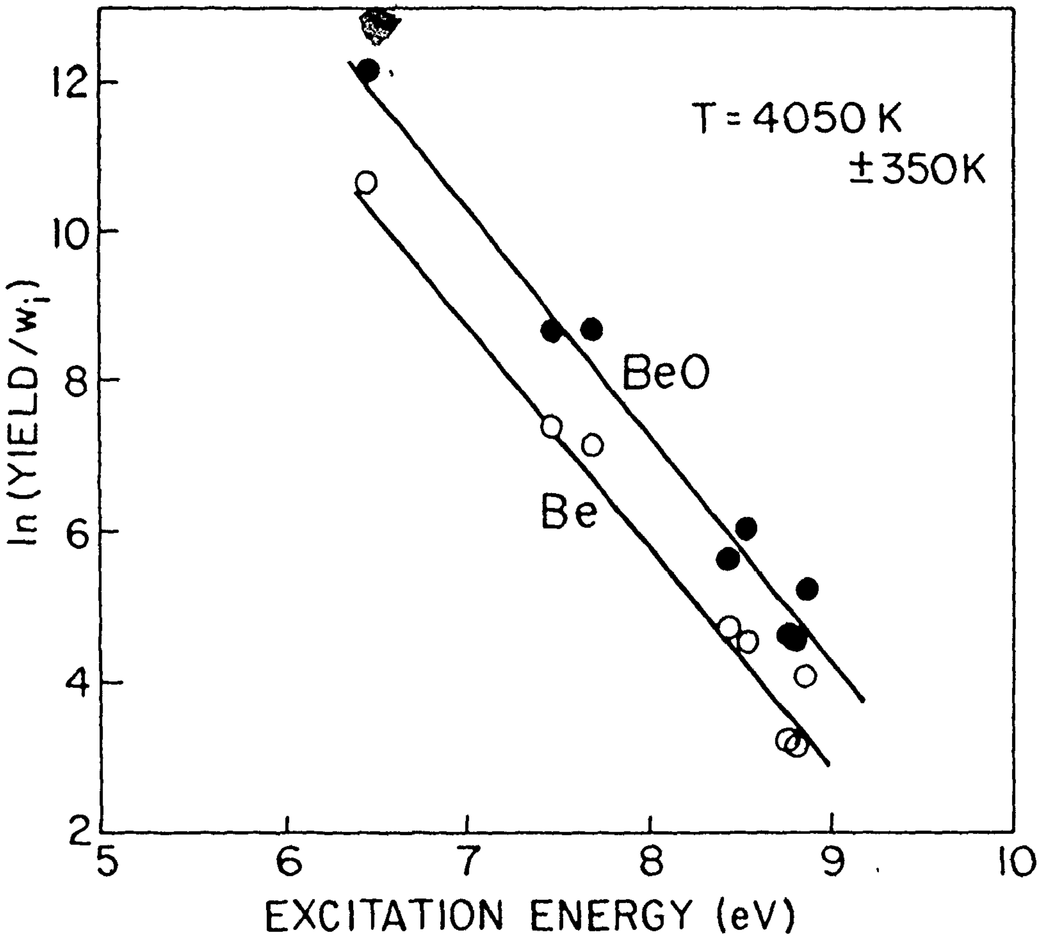

Fig. 6.2. Photon yields vs. excitation energy for Be and anodic BeO when bombarded with 12 keV Kr^+ at a current density of 15 μA/cm^2. "w_i" is the degeneracy.

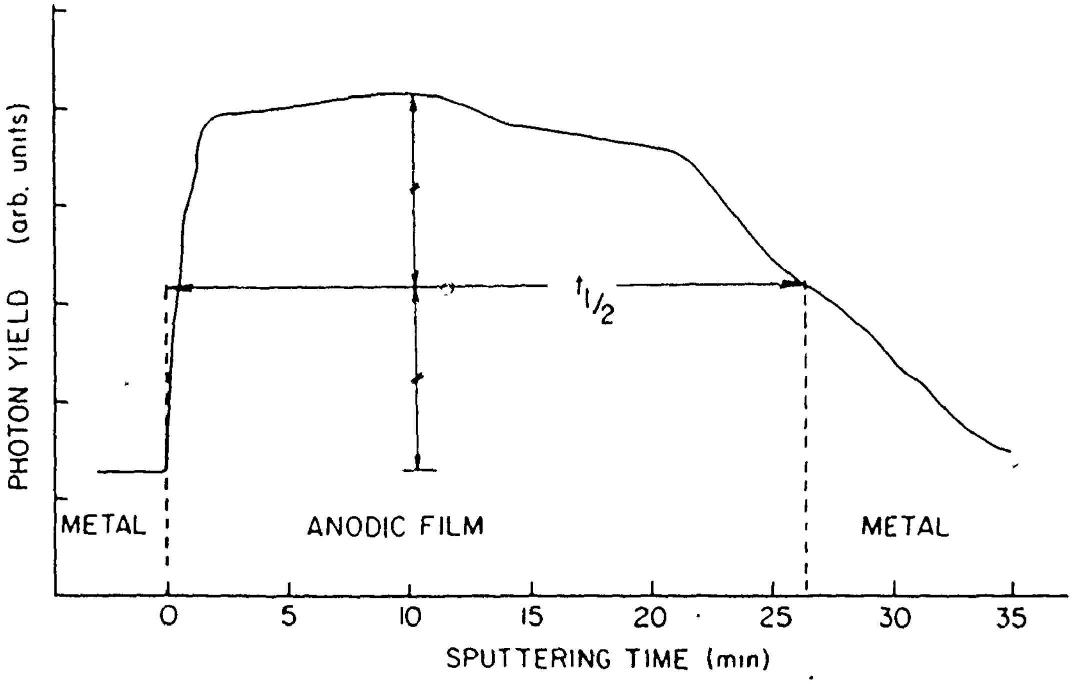

Fig. 6.3. Composition-depth profile for anodic film formed by anodizing Be in the ethylene-glycol-based electrolyte with a preset potential of 50 V. Sputtering was undertaken with 15 μA/cm^2 of 12 keV Kr$^+$, and the anodic film was inferred from the enhancement of the Be signal at 235 nm. The lack of an abrupt film-metal interface is regarded as an artifact of the ion beam being non-uniform.

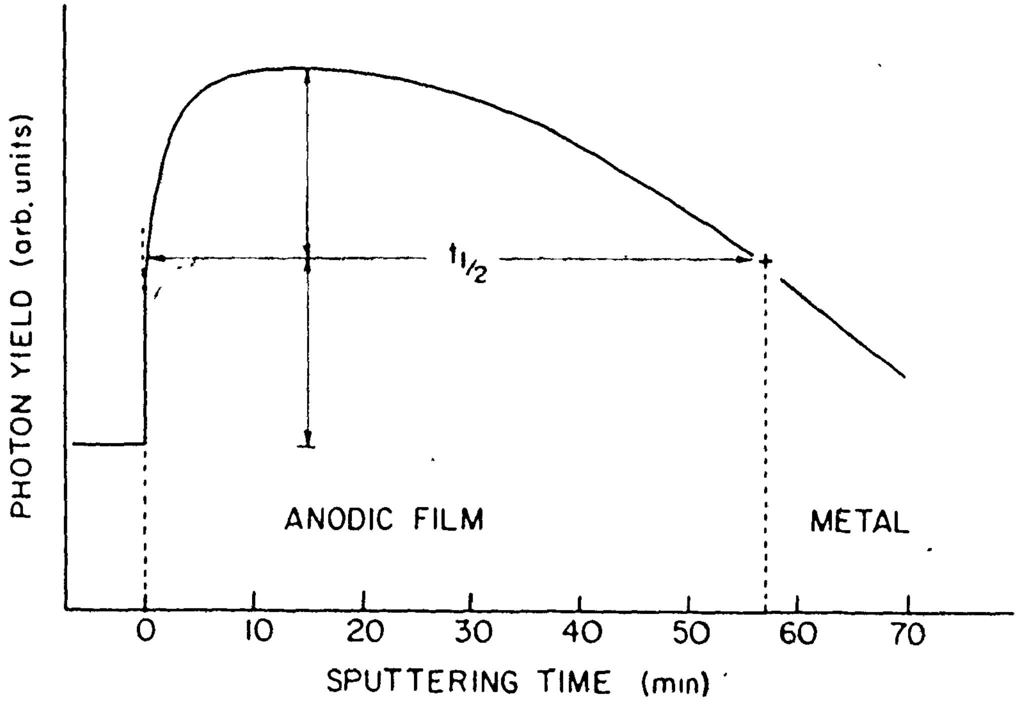

Fig. 6.4. Like Fig. 6.3 but for anodic film formed on Zr in 3% ammonium pentaborate at 100 V. The anodic film was inferred from the enhancement of Zr signal at 463.4 nm.

characteristic of the metal is shown. When the ion beam starts to sputter through the oxide, the high photon yield characteristic of the oxide is obtained. Furthermore, when the oxide film (50 V thick) has been sputtered away and the metal substrate is reached, the photon yield drops again to the metal level. However, it should be pointed out here that the high yield from the film falls gradually when the metal substrate is reached and this, in fact, was found in all the profiles obtained in the present work. This lack of an abrupt fall is regarded as an artifact of the ion beam being non-uniform and not a description of the film-metal interface. Another possible reason which could have aided this gradual drop is recoil implantation, i.e. the sputtering of the oxide forward into the metal. As such, it was found convenient to take (as shown in Fig. 6.3) the time for half-intensity $t_{1/2}$ as being the time to sputter the anodic film. Similar results for the sputtering of anodic films on Zr are obtained. Fig. 6.4 shows the observed yields from the ZrI (463.4 nm) line, while profiling an anodic-oxide film (100 V thick) formed on Zr in 3% ammonium pentaborate. Again a gradual drop of photon yields is observed when the metal substrate is reached and the time for half-intensity $t_{1/2}$ is taken as being the time to sputter the anodic film.

Sputtering coefficients for BeO and ZrO_2 can now be calculated from the profiles since the oxide-film thicknesses are known. For Be, the thickness of the anodic-oxide film x was discussed in Section 4.4.2 and found to be $x \simeq 0.21$ V $\mu g/cm^2$ ($\sim$ 0.7 nm/V), whereas for Zr the oxide-film thickness is estimated to be $x \simeq 1.3$ V $\mu g/cm^2$ ($\sim$ 2.0 nm/V) (13). The thickness sputtered at any time t (min), by a current i (μA), follows as

$$x = \frac{i\ t\ S < m > C \times 10^6}{A\ N}\ \mu g/cm^2 \qquad (6.1)$$

where S = sputtering coefficient (atom/incident ion)

$< m >$ = mean atomic weight of solid = 12.5 (g/mol) for BeO

= 44.33 (g/mol) for ZrO_2

$C = 3.74 \times 10^{14}$ ion/μA min

A = area of beam = 0.28 cm^2

and $N = 6.023 \times 10^{23}$ atom/mol

We thus obtain

$$\left.\begin{aligned} x &= 0.0078\ i\ t\ S \quad \text{for BeO} \\ &= 0.098\ i\ t\ S \quad \text{for } ZrO_2 \end{aligned}\right\} \qquad (6.2)$$

From the oxide profiles, the time to cut through the oxide $t_{1/2}$ and the beam current are known. Thus using the above relations for the oxide thickness, the sputtering coefficients can be calculated,

$$\left.\begin{aligned} S &= 35\ x/it \quad \text{for BeO} \\ \text{or} \quad S &= 10.2\ x/it \quad \text{for } ZrO_2 \end{aligned}\right\} \qquad (6.3)$$

The times to cut through the oxide, film thicknesses, beam currents, and wavelengths of the photons used in profiling are shown in Table 6.3 for BeO films and Table 6.4 for ZrO_2. The calculated values of the sputtering coefficients are shown in the last column, the average being 4.3 ± 0.6 atom/ion for BeO and 2.1 ± 0.3 atom/ion for ZrO_2, both for 12 keV Kr. For comparison, the sputtering coefficients for some oxides for 10 keV Kr together with the results of the present work are shown in Table 6.5. Our result suggests that BeO and ZrO_2 sputter normally and not thermally like WO_3, which has a significantly higher sputtering coefficient, 9.2 atom/ion. Normal sputtering is, of course, essential for a profiling study so we conclude that it is feasible to sputter profile BeO and ZrO_2.

TABLE 6.2. Calculation of sputtering coefficients of BeO anodic films with 12 keV Kr beam, using the photon-emission technique.

Film thickness (volts)	Be wavelength (nm)	i^* (μA)	$t_{1/2}$ (min)	S (atom/ion)
50	234.9	4.0	25	4.0
50	234.9	5.0	17	4.7
50	249.5	4.5	22	4.0
50	249.5	3.5	29	3.9
50	249.5	4.0	27	3.7
50	249.5	5.0	15	5.3
50	332.1	5.0	16	5.0
50	332.1	4.0	27	3.7

average S = 4.3 ± 0.6

---

* ± 1 μA, accuracy ≈ 20%

TABLE 6.3. Calculation of sputtering coefficient of ZrO_2 anodic films with 12 keV Kr beam, using the photon-emission technique.

Film thickness (volts)	Zr wavelength (nm)	i^* (μA)	$t_{1/2}$ (min)	S atom/ion
25	352	10	16	2.1
50	352	9	39	1.9
50	352	9	42	1.8
50	463.4	10	34	1.9
50	463.4	9	36	2.1
100	463.4	10	59	2.2
100	463.4	10	52	2.5
100	463.4	10	54	2.4

average S = 2.1 ± 0.3

---

* ± 1 μA, accuracy ≈ 10%.

TABLE 6.4. Sputtering coefficients for some oxides for 10 keV Kr

Oxide	S (atom/ion)	Ref.
BeO	4.3 ± 0.6 (12 keV)	present
ZrO_2	2.1 ± 0.3 (12 keV)	present
Al_2O_3	2.4 ± 0.3 (12 keV)	(14)*
	1.8 ± 0.4	(15)
Nb_2O_5	3.4 ± 0.5	(15)
SiO_2	4.2	(15)
Ta_2O_5	2.5 ± 0.5	(15)
WO_3	9.2 ± 1.2	(15)

---

* using the photon-emission technique.

6.4 Profiling of Electrolyte-species Incorporated in Anodic Films

As mentioned earlier, B, P, and S are known to become incorporated into anodic films that are formed in electrolytes containing borate, phosphate and sulphate. The distributions of these species in anodic films formed on Be and Zr are investigated in this work by the photon-emission technique. This is done by sputtering the anodic films with a 12 keV Kr beam, meanwhile the characteristic photons that are emitted from the sputtered particles are detected.

The following aspects of secondary-photon profiling should be considered. First, it is noted that the first excited state for non-metallic elements, such as C, Cl, Kr, O, P and S, lie in the vacuum-ultra-violet (Column 1-3 of Table 6.5) and are therefore inaccessible with an air-filled monochromator like the one employed in this work. Thus, transitions amongst higher excited states must be chosen (Column 4-5 of Table 6.5) and the resulting photon intensities are less satisfactory. For example, the observed signal/noise ratio was about 2.5 in case of P (214.9 nm) line and about 2 in case of S (393.3 nm) line. However, unlike P and S, B yields a rather strong photon signal, for example a signal/noise ratio of about 100 for the line at 249.7 nm. On the other hand, since this wavelength was found to interfere with a Be line (249.5 nm) while profiling anodic films on Be, the B (208.9 nm) line was used instead, which yielded a signal noise ratio of about 40. Thus, in fact, boron constitutes perhaps the most easily detected electrolyte constituent amongst those in common use.

TABLE 6.5 Excited states relevant to secondary-photon profiling

Element	First excited state (notation; energy in eV)	Wave length of emitted photon (nm)	Alternative excited state (notation; energy in eV)	Alternative wave length (nm)
Al	4s ^2S;3.14	394.4	———	
B	3s ^2S;4.96	249.7*	$2p^2$ ^2D; 5.93	208.9
Be	2p $^1P°$;5.28	234.9	———	
C	3s $^3P°$;7.49	165.6**	CH $^2\Delta$	431.4
Cl	4s ^2P; 9.20	134.7**	———	
Kr	----- 10.0	123.6**	———	
O	3s $^3S°$;9.52	130.2**		
P	4s ^4P ;6.93	178.8**	4s ^2P;7.18	214.9
S	4s $^3S°$;6.86	180.7**	5p ^5P;9.16	469.4*
			S II 4d ^2F; 19.35	393.3
Si	4s $^3P°$; 4.92	252.0	———	
Zr	5p ^3G ; 3.52	352.0	———	

---

* These wavelengths conflict with Be.

** Not detectable with an air-filled monochromator.

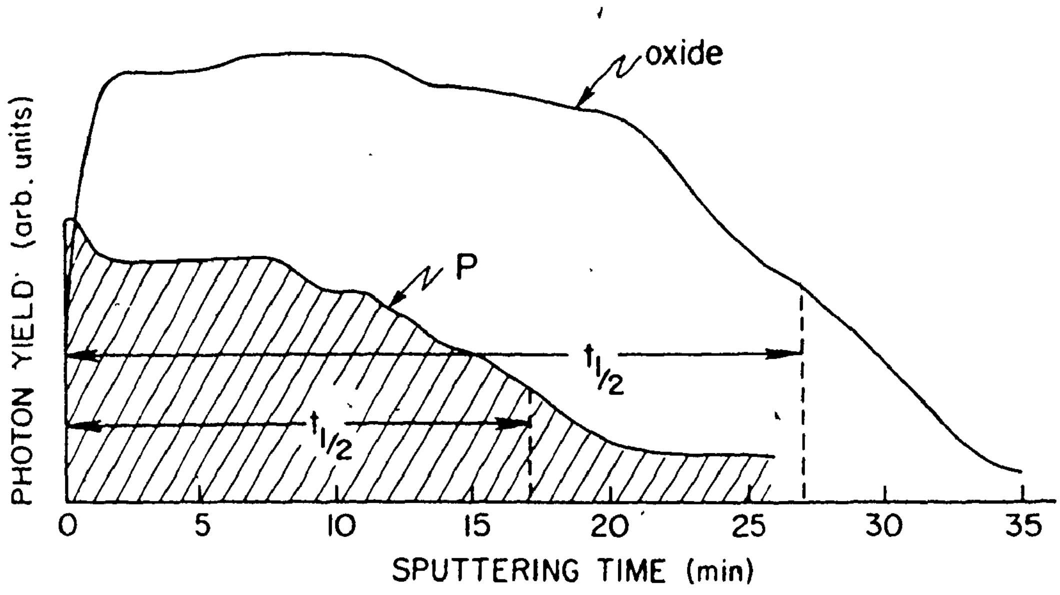

Fig. 6.5. Composition-depth profiles for both P and for the anodic film under similar conditions as in Figure 6.3. P was detected at 215 nm.

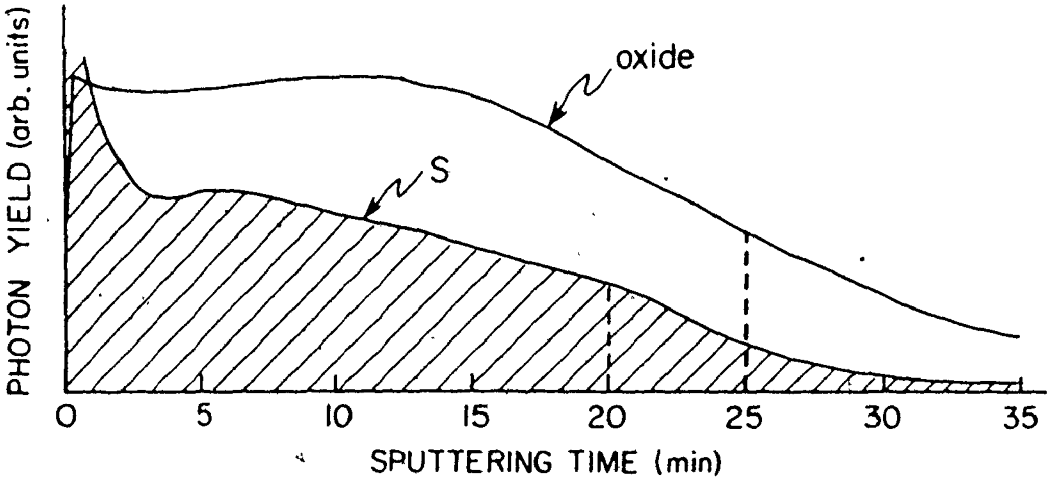

Fig. 6.6. Like Fig. 6.5 but for S which was detected at 393.3 nm.

It should be noted here that the sputtering rates, found in Section 6.3, have uncertainties of $\sim 20\%$. Hence, our profiles, if to be based on these sputtering rates, will have uncertainties of $> 20\%$. Therefore, the depth-profiles of B, P, and S were determined by using two monochromators. Thus one of these species is detected by one monochromator, meanwhile the oxide film is profiled by the other.

The depth profiling of P impurities in the anodic film on Be is shown in Fig. 6.5. The film is formed at 50 V in an ethylene-glycol electrolyte containing both Na_2HPO_4 and Na_2SO_4. The times $t_{1/2}$ and t_d, shown in Fig. 6.5 correspond to the total film thickness and the thickness of the P-containing layer (doped layer). There is evidently a significant incorporation of P which extends almost to the entire film. The depth profiling for S impurities in the same film was undertaken, the results being very similar to those for P as shown in Fig. 6.6. Additional profiling experiments were undertaken for both P and S, the results being summarized in Table 6.6.

The boron profiling, with B constituting the most easily detected electrolyte constituent, was carried out for anodic films formed on both Be and Zr. The results are shown in Fig. 6.7 and Tables 6.6 and 6.7. The anodic films on Be were formed at 50 V in an ethylene-glycol electrolyte containing 5% ammonium pentaborate, while those on Zr were formed at 25-100 V in 3% ammonium pentaborate. In addition, the B profiling in anodic films formed at 100 V in 5% ammonium pentaborate on Al (14), with the same general conditions as in the present work, is shown in Fig. 6.7. Similar results were also obtained for films formed on Al in an ethylene-glycol electrolyte containing 5%

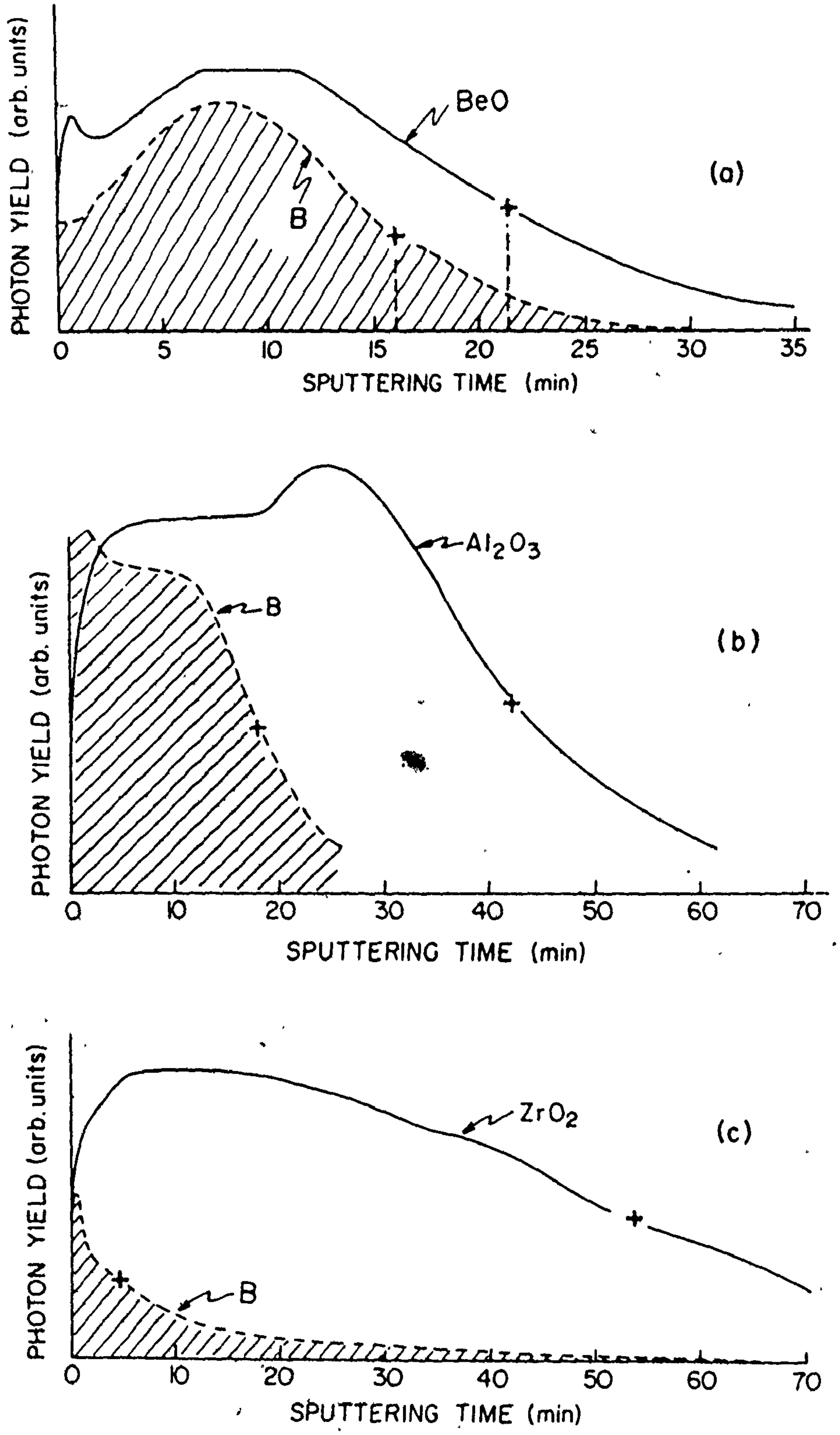

Fig. 6.7. Composition-depth profiles for both B and for the anodic films for anodized Be (a), Al (b), and Zr (c). The anodic films contain B to depths ranging from nearly the entire film with Be to the outer ∿ 10% with Zr. The profiles are, as usual, of bad quality owing to the ion beam being non-uniform.

TABLE 6.6 Calculations of "f", the fraction of the thickness doped, from the total thickness for oxide films formed on Be.

Film thickness (volts)	anion tracer used	i (μA)	t_d (min)	$t_{1/2}$ (min)	f
50	B	4.5	16	21	0.76
50	B	5	14	17	0.82
50	B	3.5	25	30	0.83
50	P	4	18	25	0.72
50	P	4	17	27	0.63
50	P	4	20	26	0.77
50	S	4.5	19	26	0.74
50	S	4.5	20	26	0.77
50	S	4.5	20	25	0.80

average f = 0.76 ± 0.06

TABLE 6.7 Calculation of "f", the fraction of the thickness doped, from the total thickness for Zr.

Film thickness (volts)	anion tracer	i (μA)	t_d (min)	$t_{1/2}$ (min)	f
25	B	10	2.5	16	0.16
50	B	9	4.5	39	0.12
50	B	10	4.3	34	0.13
50	B	9	4.8	42	0.11
50	B	9	3.3	36	0.09
100	B	10	7.5	59	0.13
100	B	10	5.5	52	0.11
100	B	10	6.2	54	0.11

average f = 0.12 ± 0.03

sodium tetraborate (14).

The depth profiles of B in the anodic films on Be, Al and Zr shown in Fig. 6.7 indicate that in all cases the films consist of two parts. The outer part includes the incorporated material from the electrolyte, while the inner part is almost pure oxide. However the thickness ratios differ greatly from one case to the other, with Be at one end, Zr at the other, and Al an intermediate case. This result will be related to the mechanism of the film growth in the following section.

6.5 Mechanism of Anodic-Film Growth

The indication from the profiling experiments that anodic films have two parts, of which the outer contains impurities from the electrolyte, enables conclusions to be reached about the mechanism of film growth.

The formation of anodic films is normally described in terms of the migration of metal cations outwards, of oxygen anions inwards, or of a combination of both (16) (Fig. 6.8). It should be noted that the metal cation migrating outwards will lead to the formation of new oxide at the oxide/electrolyte interface, and conversely for oxygen anion migration inwards. Ions like BO_3^{3-}, PO_4^{3-}, and SO_4^{2-}, if present in the electrolyte, will be adsorbed on the film surface and, in principle, subject to being incorporated into the film that is formed at the oxide/electrolyte interface. If these ions, in whatever form they assume when incorporated, are not mobile then the portion of the film containing them will correspond to metal-ion migration while the remainder of the film will correspond to oxygen-ion migration. If in addition, dissolution of

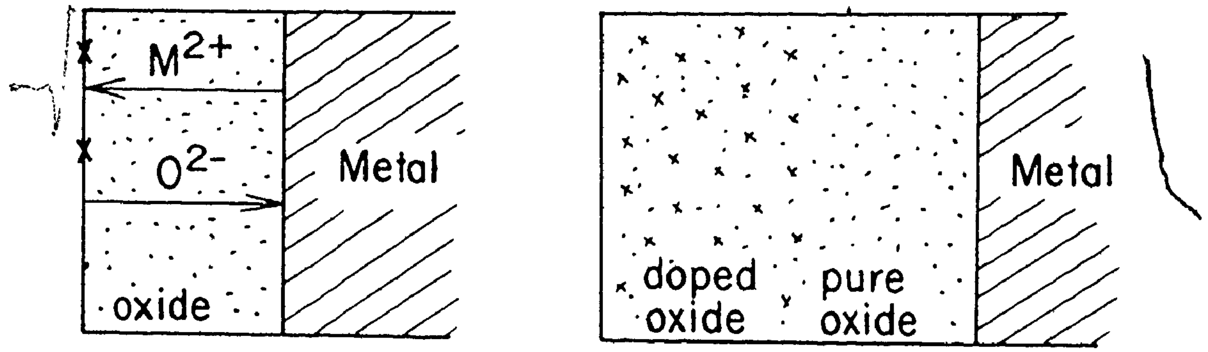

Fig. 6.8. Schematic diagram of defect transport during the formation of an anodic film. Outward motion of metal ions leads to film which will tend to pick up material from the electrolyte and conversely for the inward motion of oxygen ions.

TABLE 6.8 Cation transport numbers

Ion	Present work	Previous work	Cation size (nm)	Mobile defect
Be^{2+}	0.76 ± 0.06	-	0.035	Cation (19,20)
Al^{3+}	0.45 ± 0.10 (14)	0.58 ± 0.03 (16); 0.77 ± 0.03 (9)	0.051	Cation (21,22)
W^{6+}	-	0.34 ± 0.04 (16)	0.062	-
Ta^{5+}	-	0.29 ± 0.02 (16); 0.46 ± 0.05 (3,8)	0.068	-
Nb^{5+}	-	0.27 ± 0.04 (16); ∼ 0.5 (3)	0.069	-
Hf^{4+}	-	0.05 (16)	0.078	Anion
Zr^{4+}	0.12 ± 0.03	0.03 ± 0.02 (16)	0.079	Anion (23-25)

the film during anodizing is unimportant (true at least for Be, Sec. 3.6, and Al (17)), the ratio of the thickness of the doped layer to the total film should yield the cation transport number, with values as shown in Table 6.8. Included in Table 6.8 are previous results for Al, W, Ta, Nb, Hf, and Zr (3,8, 9, 14, 16). The similarities between the present and previous results with Zr and Al serves as an indication for the effectiveness of the approach used here.

It is of interest that the cation transport numbers described here for anodic films correlate both with the ion size and with the nature of the mobile defect as inferred from self-diffusion work with the corresponding oxides. As seen in Column 4 of Table 6.8, there is a gradation from cation transport with Be, Be^{2+} being particularly small, to anion transport with Zr. Moreover, if O^{2-} is indeed too large to move in BeO, then it is quite reasonable to have assumed in obtaining the transport numbers that the incorporated B, P, and S, in principle present as BO_3^{3-}, PO_4^{3-} and SO_4^{2-}, were immobile. The relevant sizes here are 0.180 nm (O^{2-}), 0.214 nm (BO_3^{3-}), 0.238 nm (PO_4^{3-}), and 0.230 nm (SO_4^{2-}) (18).

Ionic radii are not always a good guide in the matter of defect transport, and fail, for example, to explain why with ZrO_2 it is O^{2-} rather than Zr^{4+} which is mobile. However, the study of the defect structure of ZrO_2 (23-25) indicates that it has an excess of oxygen interstitials which are quite mobile. Let us therefore consider a correlation between cation transport number and the nature of the mobile defect as inferred from self-diffusion work. Insofar as information is available (19-25), the correlation is successful as shown in Column 5 of Table 6.8.

6.6 Summary and Concluding Remarks

(1) The emitted photons from Be and BeO are found to have discrete energies, with significantly higher yields from the oxide than the metal. Also, a straight-line relation is found when the logarithm of the photon yield is plotted against the energy of the excited state for both Be and BeO. The slope of the line is found to infer a temperature of 4050 ±350 K. This is in accord with the prediction of the thermal-excitation model discussed in Chapter 5, though does not prove its correctness.

(2) Not only are significant photon yields observed from Be, but also from other metallic elements that have low-lying excited states, like B and Zr. On the other hand, most of the non-metallic elements, such as C, Cl, O, P and S, are found to have first excited states in the vacuum ultra-violet and are therefore inaccessible with an air-filled monochromator. Thus, transitions amongst higher excited states had to be chosen and the observed yields were less satisfactory.

(3) The oxygen enhancement of photon yields have made it possible to profile anodic-oxide films on Be, as well as Zr, in spite of the lack of a useful oxygen signal. As the oxide-film thicknesses are known, sputtering coefficients for BeO and ZrO_2 could be determined from the profiles and found to be 4.3 ± 0.6 and 2.1 ± 0.3 atom/ion, respectively, for 12 keV Kr. These values indicate "normal" sputtering, as distinct from thermal sputtering, and suggest that it is feasible to sputter profile BeO and ZrO_2.

(4) Due to the high uncertainty in the sputtering rates, the depth-profiles of B, P and S in the anodic films were determined by using two monochromators, so that two species could be detected at the same time.

This enabled us to determine the fraction of the doped thickness with a higher certainty.

(5) The mechanism of film growth during anodizing of Be, Al and Zr is discussed, based on the fraction of the thickness doped in the above profiles. As a result, cation transport numbers were inferred and found to be 0.76 ± 0.06 (Be), 0.45 ± 0.10 (Al from ref. (14)), and 0.12 ± 0.03 (Zr). The transport numbers are found to correlate with the nature of the mobile defect in the oxide as inferred from self-diffusion work. On the other hand, the similarity between the present and previous results for Al and Zr serves as an indication for the effectiveness of the approach used here.

REFERENCES TO CHAPTER 6

1. D.A. Vermilyea, Acta. Met., 2, 482 (1954).
2. P.H.G. Draper, Acta Met., 11, 1061 (1963).
3. J.J. Randall, W.J. Bernard, and R.R. Wilkinson, Electrochim. Acta, 10, 183 (1965).
4. D.M. Smyth, T.B. Tripp, and G.A. Shirn, J. Electrochem. Soc., 113, 100 (1966).
5. D.M. Smyth, ibid., 113, 1271 (1966).
6. G. Amsel, C. Cherki, G. Feuillade, and J.P. Nadai, J. Phys. Chem. Solids, 30, 2117 (1969).
7. C.J. Dell'Oca and L. Young, J. Electrochem. Soc., 113, 1545 (1970).
8. R.E. Pawel, J.P. Pemsler, and C.A. Evans, ibid., 119, 24 (1972).
9. J.J. Randall and W.J. Bernard, Electrochim. Acta, 20, 653 (1975).
10. H.M. Naguib and R. Kelly, Rad. Effects, 25 (1975) 1.
11. W.L. Wiese, M.W. Smith and B.M. Glennon, Atomic Transition Probabilities, Vol. I, National Bureau of Standards, Washington, D.C. (1966) 22.
13. J.J. Polling and A. Charlesby, Proc. Phys. Soc., 67B (1954) 201.
14. C.J. Good, M.Sc. Thesis, McMaster University (1976).
15. R. Kelly and N.Q. Lam, Rad. Effects, 19 (1973) 39.
16. J.A. Davies, B. Domeij, J.S.P. Pringle and F. Brown, J. Electrochem. Soc., 112 (1965) 675.
17. J.A. Davies, J. Friesen and J.D. McIntyre, Can. J. Chem., 38 (1960) 1526.
18. N.N. Greenwood, "Ionic Crystals, Lattice Defects, and Non-stoichiometry" (Butterworth, London, 1968), p. 35.

19. S.B. Austerman, J. Nucl. Mat., 14, 248 (1964).

20. J.B. Holt, ibid., 11, 107 (1964).

21. A.E. Paladino and W.D. Kingery, J. Chem. Phys., 37, 957 (1962).

22. Y. Oishi and W.D. Kingery, J. Chem. Phys., 33, 480 (1960).

23. W.H. Rhodes and R.E. Carter, J. Am. Cer. Soc., 49, 244 (1966).

24. L.A. Simpson and R.E. Carter, J. Am. Cer. Soc., 49, 139 (1966).

25. A. Madeyski and W.W. Smeltzer, Mat. Res. Bull., 3, 369 (1968).

CHAPTER 7

THE STRUCTURE OF ANODIC-OXIDE FILMS

7.1 Introduction

We mentioned earlier in Section 2.4 that anodic-oxide films formed on metals are found to be of variable structure and, in view of the importance of these ideas to what follows, we repeat part of what was said. Anodic films are formed either in the amorphous or the crystalline state depending on the material, on the film thickness, and on the various anodizing conditions, including the kind of electrolyte being employed and the anodizing temperature. In particular, the films formed on Hf(1), Sn(2), Zn(3) and Zr(4,5) are believed to be invariably crystalline, those on Ge(6) and Si(7) are believed to be invariably amorphous, while those on Al(8), Be (Ch.3), Mo(9,10), Nb(11), Ta(8,10-12), Ti(5,8,10), V(10,13), W(5,8,10) and U(11,14) have been found to have a variable structure. If we regard amorphous films to be the norm in the last 9 cases, then crystalline films can be said to appear under conditions as follows:

high anodizing temperature	Al, Nb, Ta and Ti
particular electrolytes	Be
small film thicknesses (<10 V, i.e. $\lesssim$ 30 nm)	Mo, Ta, V, W and U
large film thicknesses or long anodizing times	Al, Nb, Ta and Ti

The question of why the various anodic films are amorphous or crystalline has not been answered yet. There is no previous rule which could be followed to determine the structure for anodic films, with the exception of the very recent attempt made by Arora and Kelly.(10) In this attempt, to be discussed in more detail in Sec. 7.2.3, analogy was proposed between the crystallization produced by the energy deposited by an impacting ion and that produced by a defect moving in the oxide under an electric field. If such analogy is valid, then, based on the same criterion for the crystallinity of an ion bombarded solid (also to be discussed below in Sec. 7.2.2), oxides can be classified as follows. Those oxide which have (crystallization temperature/melting temperature) = $T_c/T_m \gtrsim 0.3$ will be formed amorphous, while those having $T_c/T_m \lesssim 0.3$ will form crystalline. However, in spite of this model being valid for 18 out of 20 cases considered by Arora and Kelly, they admit that the model can be disputed on a quantitative basis. In addition, the model is not able to explain why we have a variable structure on the same metal depending on the anodizing conditions, as mentioned earlier for 9 cases, since it only considers the material of the anodic film and its crystallization and melting temperatures.

Therefore, we feel the need for an alternative criterion that determines the structure of anodic films. Such a criterion should not only consider the material of the anodic film but also the conditions under which the film is formed. It is the object of this chapter to develop such a criterion. To this end we are going to present first a very brief review of the existing criteria for the structure of oxides. Then we will try to apply formal crystallization theory, i.e. the theory of nucleation and growth of crystals in undercooled liquids, to anodic-oxide films. Finally, we will attempt, based on the above picture, to develop a criterion for the structure of anodic films.

7.2 Previous Criteria for the Structure of Oxides and Oxide Films

In this section we present a very brief review of the previous models or criteria that are employed to predict the structure of oxides. In each case we will try to correlate the model to anodic-oxide films.

7.2.1 Sun's Bond Strength Criterion, Rawson's Modification, and our own Modification for Anodic Films

Sun(15) suggested that one would expect a correlation between the ability of a material to form a glass (or an amorphous solid) and the strength of interatomic bonds, since the process of atomic rearrangement that takes place during the crystallization of the material may involve the breaking and reforming of these bonds. Therefore the stronger the bonds the more sluggish will be the rearrangement process and hence the more readily will a glass be formed. He also showed that the single M-O bond strengths in glass-forming oxides are in fact particularly high, > 375 kJ/mol, whereas for modifiers the values are < 250 kJ/mol. The single M-O bond strength for an oxide of formula MO_a is calculated by dividing the energy E_d required to dissociate the oxide into its constituent gaseous atoms by the number of oxygen atoms surrounding the atom M in the crystal or the glass. E_d can be defined for an MO_a oxide as follows:

$$E_d = a\,\Delta H_f(O)_g + \Delta H_f(M)_g - \Delta H_f(MO_a)_s \qquad (7.1)$$

Here, $\Delta H_f(O)_g$ and $\Delta H_f(M)_g$ are the heats of formation of atomic oxygen and atomic metal and $\Delta H_f(MO_a)_s$ is the heat of formation of the solid oxide.

Rawson(16) modified Sun's criterion as follows. If one were to relate glass formation to the ease with which primary valence bonds can be broken at the freezing temperature , one should consider not only the strength of the bonds but also the amount of thermal energy available to break them. The melting temperature itself in the case of simple substances or compounds is a rough measure of the amount of energy available. Rawson therefore, suggested that one should use not the single bond strength, but the ratio of the bond strength to the melting temperature T_m in kelvins as a criterion for glass formation. Such a criterion however, cannot be applied to anodic-oxide films as they are formed at ordinary temperatures and not quenched from the liquid state at temperatures higher than T_m. Therefore, we suggest the following modification.

For an anodic oxide film to form in the amorphous or the crystalline state, one should consider the strength of interatomic bonds in the liquid state at ordinary temperatures. The stronger the bonds the more sluggish will such a film crystallize and hence more readily will it form in the amorphous state.

We have calculated the bond strength for some oxides from the heat of formation data available in the JANAF tables for the solid oxide, the liquid oxide and both atomic oxygen and atomic metal. The results are shown in Table 7.1 and can be summarized as follows:

Based on Sun's criterion we get the following order:

SiO_2, WO_3, Ta_2O_5, Nb_2O_5, Al_2O_3, V_2O_5, MoO_3, TiO_2, BeO, ZrO_2

for the ability to form a glass (or an amorphous solid).

Table 7.1 Calculations of interatomic bonds for some oxides corresponding to Sun's criterion $B_{M-O(solid)}$, Rawson's modification B_{M-O}/T_m and our own modification for anodic films $B_{M-O(liquid)}$.

Oxide	$E_{d(solid)}$ kJ/mol	Number of bonds (16,17)	$B_{M-O(solid)}$ kJ/mol	T_m K	B_{M-O}/T_m J/mol.K	$E_{d(L)}$ kJ/mol	$B_{M-O(L)}$ kJ/mol
SiO_2	1856	4	464	1993	233	1847	462
WO_3	2442	6	407	1748	233	2388	398
Ta_2O_5	4856	(5-6)x2	405-486	2058	197-236	4767	397-477
V_2O_5	3831	5x2	383	943	406	3828	382
Nb_2O_5	4611	(5-6)x2	384-461	1785	215-258	4543	378-454
Al_2O_3	3075	4x2	384	2327	165	2982	372
MoO_3	2151	6	359	1068	336	2111	352
TiO_2	1916	6	319	2123	150	1856	309
BeO	1175	4	294	2820	104	1123	281
ZrO_2	2216	8	278	2923	95	2142	268

Based on Rawson's modification we get the following order:

V_2O_5, MoO_3, Nb_2O_5, Ta_2O_5, SiO_2, WO_3, Al_2O_3, TiO_2, BeO, ZrO_2

Based on our modification for anodic films we get the following order:

SiO_2, WO_3, Ta_2O_5, V_2O_5, Nb_2O_5, Al_2O_3, MoO_3, TiO_2, BeO, ZrO_2

Generally speaking, all three criteria agree with the experimental results that ZrO_2 is invariably crystalline and BeO and TiO_2 are normally crystalline, Nevertheless they serve only for ordering and not for making numerical predictions.

7.2.2 Naguib-Kelly Criterion

This model has been suggested by Naguib and Kelly(18) to explain the state of crystallinity of ion-bombarded solids, though, as discussed below, can be employed also with anodic films. Briefly stated the argument is as follows. During ion bombardment of crystalline solids, displacement cascades will form and consist of a compact liquid-like region surrounded by crystal, provided the ion is sufficiently heavy. For incident ion energy ζ, x-straggling Δx, y-straggling $\langle y^2 \rangle^{1/2}$, mean atomic spacing λ, and heat capacity 3k, the initial temperature of the cascade will be given approximately by:

$$T \approx \zeta \ \lambda^3 / \Delta x \ \langle y^2 \rangle \ 3k \qquad (7.2)$$

or about 3000 K (19). The cascade cools rapidly with a $\bar{t}^{3/2}$ cooling law and crystallization begins when the temperature falls below the melting point (T_m). The total distance moved by the crystallization front follows as:

$$x_c = (1/\lambda) \int_{t_1}^{t_2} D_c \, dt, \qquad (7.3)$$

where t_1 is the time when $T = T_m$, t_2 is any subsequent time when T is somewhat greater than T_2 (the ambient temperature) and D_c is the diffusion coefficient for crystallization. If D_c is taken as proportional to $\exp(-\Delta h_c/kT)$ and T is given by $(T_\infty + At^{-3/2})$, equation (7.3) can be evaluated. Their final result is that x_c is less than λ, i.e. crystallization is avoided, if the following is true:

$$T_c/T_m \gtrsim 0.3$$

Here Δh_c is the activation energy of crystal growth (i.e. the Δh corresponding to Δg in eq. 7.11) and T_c is the crystallization temperature as measured in a typical thin-film experiment with a 2 to 15 minute time scale. Values for T_c/T_m together with the state of crystallinity after ion bombardment are shown in Table 7.2, which was presented (10) to show the plausibility of the model. More interesting is employing this model to anodic films as will be discussed now.

7.2.3 Arora-Kelly Criterion

The question of why the various anodic films are amorphous or crystalline was attempted for the first time by Arora and Kelly (10). In their argument, they draw a tentative parallel between anodically formed oxides and oxides which have been subject to high-dose ion bombardment as discussed above. Such a comparison is not necessarily unreasonable, for just as an anodic oxide is created at low temperatures and is therefore unable to equilibrate, so particle impact causes dis-

TABLE 7.2. Summary of oxide film crystallinity (10).
Cr = crystalline, am = amorphous

Oxide	State when formed anodically	State when ion-bombarded	T_c/T_m (K/K)
ZnO	Cr	Cr	0.17
BeO	Cr*	Cr	0.25
HfO_2	Cr	Cr	∿ 0.25
ZrO_2	Cr	Cr	0.27
UO_2	Cr	Cr	0.30
TiO_2	am+ or Cr	am	0.35
Ta_2O_5	am+	am	0.38 - 0.46
SnO_2	Cr	am	∿ 0.41
Nb_2O_5	am+	am	0.42-0.49
Fe_2O_3	am	am	∿ 0.43
Al_2O_3	am	am	0.43
WO_3	am	am	0.43
Bi_2O_3	am	am	0.49
MoO_3	am	am	0.49
SiO_2	am	am	0.57
V_2O_5	am	am	0.61
GeO_2	am	am	0.65
MoO_2	Cr	Cr	-
δ-Ta-O	Cr	Cr	-
U_3O_8	am	am	-
WO_2	Cr	Cr	-

---

* With most electrolytes, though not "electrolyte A" of Sec. 3.3. The latter introduces significant P and S (Sec. 6.4).

\+ With unheated electrolytes and/or low current densities, particularly in the case of TiO_2.

ordering similar to the liquid state which in many instances is preserved by quenching. Such quenching, in the case of ion-bombarded solids, is likely to succeed when $T_c/T_m \gtrsim 0.30$ as mentioned before. They propose that anodic films can be treated the same way and to follow the same criterion. In their argument they draw an analogy between the energy deposited by an incident ion with what they called "the field-imparted energy" defined as follows. If q is the charge of the mobile defect in the oxide, e the electronic charge, λ_c mean cation spacing* and E_f is the formation field, the latter energy is just:

$$\zeta = qe\lambda_c E_f \qquad (7.4)$$

They then assumed that this energy will be dissipated in roughly 10^{-11} to 10^{-12} s , based on the relation $Kt = r^2$ and taking K, the thermal diffusivity, as 10^{-2} to 10^{-3} $cm^2\ s^{-1}$ and r as 1 nm. The next jump of the defect occurs at a much longer time, as they deduced an average time for a jump during anodizing to be in the order of 0.04 s per λ_c^2 of surface. Therefore, they concluded that the mobile defect behaves, following each field assisted jump, like a displacement spike cascade of point dimensions and with temperature.

$$T = qe\lambda_c E_f/3k \qquad (7.5)$$

The remainder of the argument assumes full parallelism to that for a true displacement cascade, such that anodic films for which $T_c/T_m \gtrsim 0.3$ will tend to avoid crystallization and therefore be amorphous. This

---

* The use of λ, the mean atomic spacing, in ref. (10) was not strictly correct. The mean cation spacing, λ_c, which can be taken as a sort of jump distance, is preferable.

criterion was applied to 20 cases, and it was found that for 18 cases the state of crystallinity is as expected (Table 7.2). The two exceptions are anodic TiO_2 and SnO_2 films, though since they had intermediate values of T_c/T_m, were claimed to be only partial exceptions.

The main weakness in the argument of the above crystallization model relates to the dimensions of the heated region. The heat deposited by an impacting ion is distributed over a sufficient volume, $\Delta x<y^2>$, for heat conduction theory to have a reasonable chance of being valid, whereas that due to anodizing is localized to a single atom. On the other hand, an anodic film with thickness $x = 100\ \lambda_c$ suffers, as is easily shown, about 5×10^3 defect jumps per λ_c^2 surface, so there are 5×10^3 chances for crystallization to initiate per λ_c^2 surface. Another problem is that some oxides, such as MoO_2 and WO_2, are metallic conductors (20) and should not support a large field to form a crystalline film. The model can therefore, as admitted by the authors, be disputed on a physical basis in spite of being valid for 18 out of 20 cases described.

7.3 Application of Formal Crystallization Theory to Anodic Films

The formal theory of crystallization has been well developed for pure liquids. In such theory crystallization always seems to take place by a process of nucleation and growth. That is, small crystals form and grow into undercooled liquid, all transformations occurring at the liquid/crystal interface. Therefore, two processes are necessary to describe crystallization: the nucleation of a crystal in an undercooled liquid (or an amorphous phase) and the velocity u of its growth after nucleation. With the knowledge of these two, we should be able to define the conditions for crystallization or bypassing crystallization, i.e: having an undercooled liquid or an amorphous solid.

No attempt will be made here to review the theory of crystallization of pure liquids. There are a number of excellent reviews which have presented the detailed treatment and derivation of such theory as well as its application to the formation of silicate glasses, as by Turnbull$^{(21)}$ and the references cited therein. We shall, therefore, restrict ourselves to introduce the results of such theory for the two processes, nucleation and growth; try to apply such theory to the formation of anodic oxide films; and attempt to determine the conditions under which an anodic oxide film will form in the amorphous or in the crystalline state.

7.3.1 Nucleation of a Crystalline Phase

The crystal nucleation resistance of a liquid can be understood in terms of a simple nucleation theory devised by Turnbull$^{(21)}$. The "resistance" arises from the work, γA, which must be done to form the crystal/liquid interface, A being the area and γ the surface energy or the tension of the interface.

On the other hand, nucleation is motivated by the free energy change in the crystallization of the bulk liquid, which is the product of the volume V and the free energy change per unit volume, ΔG_c:

$$\Delta G_c = (G_L - G_s)/\overline{V} \qquad (7.6)$$

Where G_L is the molar free energy of formation of the liquid

G_s is the molar free energy of formation of the solid

$\overline{V}$ is the molar volume

Thus, balancing the two terms, the resistance γA which increases with the area A and the motivation term ΔG_c which increases (in magnitude) with volume V, leads to the condition that only those crystals larger than some critical size r^* can on the average become nuclei for crystal growth, where

$$r^* = -\frac{2\gamma}{\Delta G_c} \qquad (7.7)$$

Turnbull has described the condition for bypassing crystallization, hence for the formation of an amorphous phase, by considering the condition that nucleation be suppressed. Since the existence of one stable nucleus may be enough to crystallize the whole volume, the first nucleus should not be allowed to form. The formation of the first nucleus will require at least the time t_{min} for all the molecules i^* constituting the nucleus of the size r^* to rearrange from a liquid configuration to a solid configuration, i.e.,

$$t_{min} = i^* \tau_i \qquad (7.8)$$

where τ_i is the jump time, which can be correlated to the viscosity of the liquid. Therefore, a liquid will not crystallize if cooled to its glass temperature in less than t_{min}.

Such theory is good enough to explain why it is difficult to bypass the crystallization of normal liquids, like metals, thence to obtain amorphous metals. Thus, the cooling rates needed are extremely high, in the order of 10^{12} Ks^{-1}. But what about anodic films? Can this theory be employed with anodic films which form at room temperature? What, for example, might the critical size r^* be for anodic films formed at room temperature?

To calculate r^* for anodic oxide films, two parameters are needed: the [illegible] change per [illegible] G_s G_l

γ_{SL}, both at room temperature. For the first parameter one can in particular cases make use of recent tabulations (22-24) of the Gibb's free energy formation for liquid and crystalline oxides as a function of temperature (Column 3 of Table 7.3). For the second parameter, γ_{SL}, various tabulations exist for metals and alkali-halides but not for oxides. However, a rough semi-empirical relation exists (25) between the surface energy and the heat of melting ΔH_m as follows:

$$\gamma_{SL} \lambda_M^2 = 0.3\Delta H_m \qquad (7.9)$$

where now λ_M is the mean molecular spacing as defined in Appendix I.

The heat of melting at room temperature is tabulated (22-24) and from this γ_{SL} follows with eq. 7.9 (Column 2 of Table 7.3). The important result is that the critical sizes of the nuclei r^* are very small, being of the order of the mean molecular spacing (Columns 4 and 5 of Table 7.3). Therefore, even allowing for a factor of 2 or greater error in the empirical relation of eq. 7.9 for γ_{SL}, the following conclusion can be reached. The crystallization of anodic films, formed at room temperature, has no nucleation problem and what determines the state of their structure (amorphous or crystalline) is how fast these nuclei are able to grow. Growth rates are considered in the following section.

The above conclusion has further importance. Since nucleation is evidently not a problem we see why the Arora-Kelly criterion should have worked as well as it did. This criterion, it will be recalled, dealt solely with crystal growth, making no mention at all about nucleation.

TABLE 7.3. Calculations of r^* for some oxides.

Oxide	γ_{SL_2} J/m^2	ΔG_c(298 K) 10^9 J/m^3	r^* nm	$\lambda_M$$^{(+)}$ nm
Al_2O_3-γ	0.29	2.47	0.24	0.35
BeO	0.54	6.63	0.16	0.24
MoO_3	0.15	0.96	0.30	0.37
Nb_2O_5	0.16	0.98	0.33	0.46
SiO_2	0.036	0.28	0.26	0.34
Ta_2O_5	0.22	1.43	0.31	0.45
TiO_2	0.32	2.90	0.22	0.32
WO_3	0.20	1.41	0.29	0.38
V_2O_5	0.15	0.76	0.39	0.45
ZrO_2	0.32	3.04	0.21	0.34

(+) Deduced as in Appendix I.

It should be pointed out here that the classical treatment of nucleation, presented above, has a serious drawback in that it uses bulk values to γ and ΔG_c for volumes containing only few molecules. This presents, in fact, one of the real limitations of the validity of the classical treatment of nucleation. However, the non-classical nucleation treatment developed by Cahn and Hilliard$^{(26)}$ for two component systems having large supersaturation does not offer a real alternative in our case. In this treatment, the free energy is considered as having an additional term arising from the local composition gradient, and r^* is therefore larger. In short, a non-classical treatment applicable to a one-component system like ours has not been established yet. We proceed to consider growth rates in the following section.

7.3.2 Velocity of the Crystallization Front

The propagation velocity, u, of crystal growth in an undercooled liquid with no accompanying composition change, has been discussed elsewhere$^{(21)}$ and represented formally as follows:

$$u = (fD_c/\lambda_c)\ [1 - \exp(\lambda_M^3 \Delta G_c/kT)] \qquad (7.10)$$

where f is the fraction of crystal surface sites to which molecules can be attached, λ_c is (as before) the mean cation spacing, and D_c is the rate constant, having the dimensions of a diffusion coefficient, which governs the transport of molecules across the liquid/crystal interface. D_c is given by:

$$D_c = \lambda_c^2\ \nu\ \exp[-\ \Delta g/kT] \qquad (7.11)$$

where Δg is the free energy barrier for crystal growth. Such a D_c appeared also in eq. 7.3.

To use equation 7.10 effectively for predicting u, we need to know more about the product fD_c. Turnbull,$^{(21)}$ in applying this relation to crystal growth, suggested that D_c can be obtained from its correlation to the fluidity ϕ of the under-cooled liquid through the Stokes-Einstein equation$^{(21)}$:

$$u = \frac{f\ kT\ \phi}{3\pi\lambda_c^2}\left[1 - \exp(\lambda_M^3 \Delta G_c/kT)\right] \qquad (7.12)$$

Then he assumed that f and the driving free energy terms were both equal to unity and calculated the velocity of crystal growth for some silicate glasses. The results were reported to agree to within a factor of three with what was experimentally measured.

The question remains as to whether one can apply this theory to anodic films. Since there are here no data available for anodic-film fluidity ϕ, for D_c, and for "f", one can try to proceed as follows. First the free energy term for the crystal/liquid interface was calculated for various oxides at room temperature and found to be equal to unity. Extrapolation of D values from high temperatures to lower temperatures, for example from 1500-2000 K to 1000 K, is not valid because of short circuit diffusion (27). But some information about D_c comes from anodizing experiments, if one uses the field-flux relations (2.7). Let us suppose that the rate constant D_c and the parameter f in equation (7.10) can be identified with the self-diffusion constant of the oxide D and the parameter n' (in fractional units) in equation 2.7. We may then calculate n'D from the value of the electric field E and the anodizing current. For ZrO_2, as an example which forms a crystalline film, $E \approx 5 \times 10^8$ V/m, q is 2, since O^{2-} is mobile, and the current density i can be given a typical experimental value of 3 mA/cm^2. This results in a value for the parameter n'D of about 2 x 10^{20} cm^2/s. If we assume this value for fD_c in equation (7.10), we can calculate u to be 5 x 10^{-15} ms^{-1}, or, in terms of thickness for an anodizing experiment of 2 min duration, 2 x 10^{-13}m. This of course implies that such an anodic film could never be crystalline, which is not true.

The conclusion is that the kinetic barrier at the crystallization front is lower than that for diffusion through the oxide. Although no quantitative information has been reported about the lowering of the energy barrier at the crystallization front, it is instructive to try to correlate it with the free-energy gradient at the interface, Fig. 7.1, just as one treats the lowering of energy barriers for moving ions under the effect of an electrical field (see Fig. 2.3). This lowering can be applied to cases of an ion moving both through the oxide, Verwey's model, and at the interface, the Mott-Cabrera model (Fig. 2.4).

7.4 Criterion for the Structure of Anodic-Oxide Films

We first define a "crystallization parameter"

$$E^* = \frac{\Delta G'_c}{qe\lambda_M} \equiv \frac{\Delta G''_c}{qF\lambda_M} \qquad (7.13)$$

which has the units of electric field, $\Delta G'_c$ being in units of J/molecule, $\Delta G''_c$ being in units of J/mol, and F being the Faraday. Since ΔG_c is the free energy change which is driving particles having charge qe to jump across the amorphous/crystalline interface over the jump distance λ_M, E^* can be interpreted as the equivalent electric field which would produce the same change. We note at this point that it is an assumption that ΔG_c is distributed over λ_M rather than a multiple of λ_M and that we have no proof that the assumption is correct. Csepregi et al. (28,29) have made

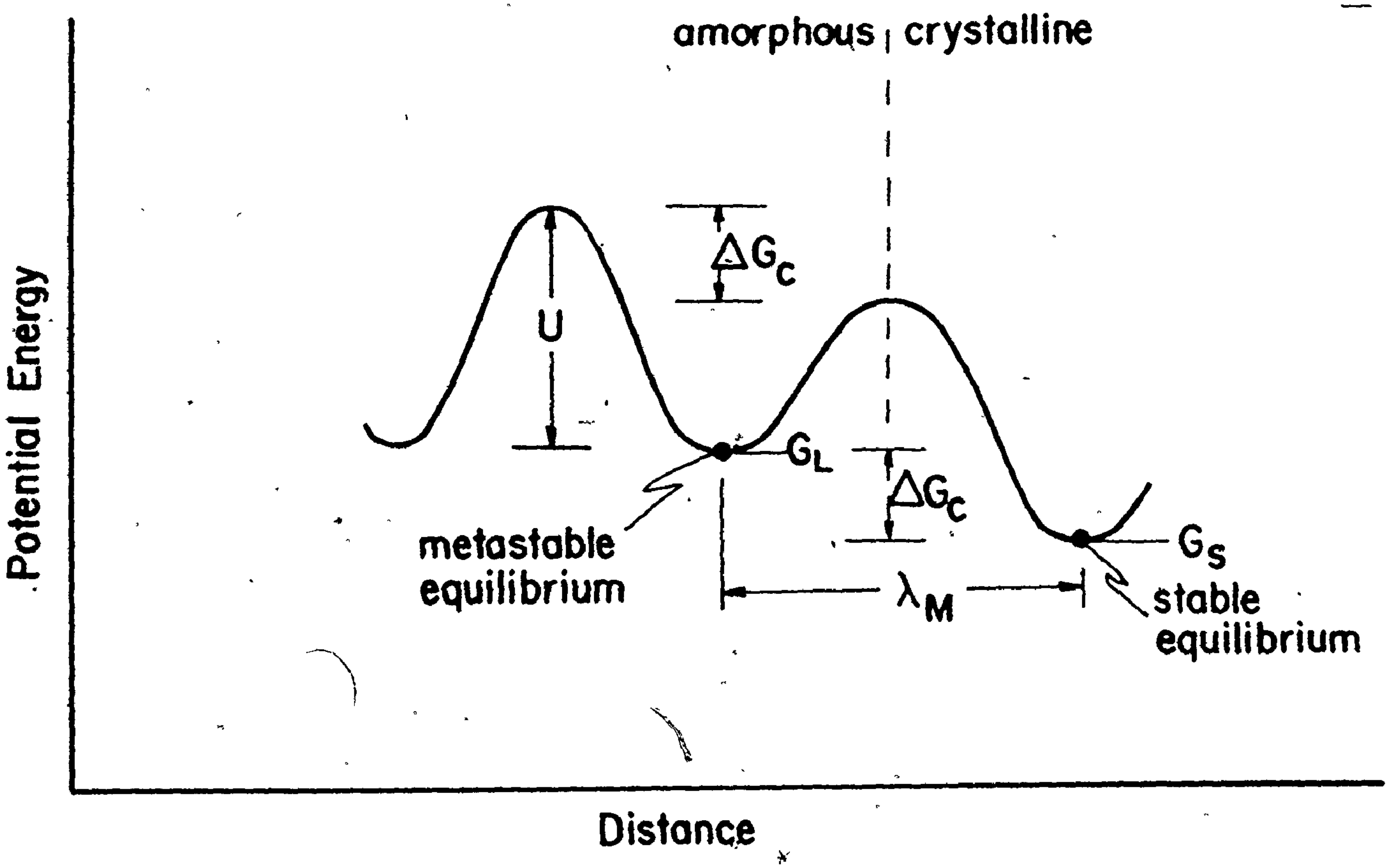

Fig. 7.1. Schematic energy-distance relationship at the crystalline/amorphous interface, showing that the free energy of crystallization can be treated as a tilting of the barrier energy at the interface.

the same assumption in their treatment of the crystallization of ion-bombarded Si(28) and Ge(29), but again without proof. We note, however, that by making this assumption they achieved a remarkably lucid interpretation of the velocity of crystal growth vs. crystal orientation. Results of our calculations for the parameter E^* are shown in Table 7.4.

To predict the state of crystallinity of the anodic oxide film, we propose that it is sufficient to compare E^* with the formation field, E_f.

(i) if $E^* > E_f$ then the barrier tilt at the crystallization front exceeds the barrier tilt due to the formation field and the film will be formed more likely in the crystalline state.

(ii) if $E^* < E_f$ then the barrier tilt at the crystallization front is less than the barrier tilt due to the formation field and the film will be formed more likely in the amorphous state.

Values of E^* and E_f together with the observed and predicted states of crystallinity for various anodic films are shown in Table 7.5. In all cases, the reported state of crystallinity is the same as that predicted. The following details are also significant:

1) An explanation for why a metal like Be sometimes forms a crystalline film and sometimes an amorphous film follows from the above model based on the formation field E_f having different values under different anodizing conditions, mainly the composition of the electrolyte. Such variations in E_f can be understood, as proposed by Arora and Kelly(30) and mentioned in Sec. 2.5, in terms of variations in the dielectric properties of an anodic-oxide film due to impurities being incorporated from the electrolyte into the film. This has been investigated for the case of Be in Sec. 4.3 and Sec. 6.4.

TABLE 7.4 Calculation E^* for some oxides. For λ_M, see Appendix I.

Oxide	ΔG_c (298 K) kJ/mol	q	E^* 10^8 V/m
ZrO_2	76.03	4	10.22
V_2O_5	41.09	10	1.90
WO_3	47.77	6	4.20
TiO_2	54.52	4	9.00
Ta_2O_5	76.9	10	3.57
SiO_2	6.28	4	0.97
Nb_2O_5	58.5	10	2.63
MoO_3	29.5	6	2.76
BeO	50.83	2	11.01
Bi_2O_3	85.19	6	3.22
Al_2O_3-γ	63.5	6	6.29

TABLE 7.5. Values of E^* and E_f together with the reported and predicted state of crystallinity for anodic oxide films.

Oxide	E^* 10^8V/m	E_f 10^8V/m	State reported	State predicted	Certainty of prediction (1 > 2 > 3)
ZrO_2	10.22	5(31,32)	Cr	Cr	1
V_2O_5	1.90	2.8(13)	am	am	2
WO_3	4.20	4.6(30)	am	am	3
TiO_2	9.00	3(33)	Cr	Cr	1
Ta_2O_5	3.57	6.4(34)	am	am	1
SiO_2	0.97	17.2(7)	am	am	1
Nb_2O_5	2.63	3.5(30)	am	am	2
MoO_3	2.76	2.9(9)	am	am	3
BeO	11.01	15	am	am	2
		5(35)	Cr	Cr	1
Al_2O_3	6.29	9.1(39)	am	am	2

2) The problem of MoO_2 and WO_2, mentioned earlier while discussing Arora's model, is to some extent resolved. Such oxides, reported to be crystalline, are metallic conductors and should not be able to support the large electric field needed to form a crystalline film based on Arora's model. However, from the present model such films by virtue of being formed at low electrical field will tend to crystallise. This explanation could in principal be extended to the other cases of very thin films (< 10V) formed on Ta and V reported to be crystalline, though the compositions of the lower oxides have not been fully identified in these two cases.

7.5 Prediction for the Structure of Anodic Films for Unstudied Systems

By way of exploring the above model, we would like to discuss a number of cases for which predictions can be made. These include cases where anodic-oxide films have not been formed (or if formed, no data are available for the formation field). Provided we have the free-energy data available for both the liquid and the solid oxides (22,23,24) we can calculate the values of the crystallization parameter E^*. The results are shown in Table 7.6.

For the purpose of predicting the structure of the anodic films if it should turn out that they can be formed, we have assumed an average value of 5 x 10^8 V/cm for the formation field, E_f. Thus, employing the present criterion, the predicted states of the anodic films together with the certainty of the predictions are shown in Table 7.6.

To explore these predictions the following details are significant:

1) If an anodic-oxide film were to be formed on B it is predicted with a high certainty level that it would be amorphous. This prediction is expected independently from the properties of the oxide. For example, in glass technology B_2O_3 is well known as a glass-forming compound like SiO_2.

TABLE 7.6. Calculations of E^* and predictions of the state of crystallinity of anodic-oxide films for unstudied systems.

Oxide	ΔG_c (298 K) kJ/mol	λ_M nm	q	E^* 10^8 V/m	State predicted if $E_f = 5 \times 10^6$ V/cm	Certainty of prediction 1 >2> 3
B_2O_3	10.9	0.36	6	0.524	am	1
Bi_2O_3	85.2 (+)	0.46	6	3.22	am	2
CaO	70.5	0.30	2	12.05	Cr	1
Cr_2O_3	103	0.37	6	4.9	-	-
Li_2O	40.8	0.29	2	7.29	Cr	2
MgO	66.5	0.27	2	12.99	Cr	1
Na_2O	40.2	0.36	2	5.85	-	-
PbO	14.4	0.34	2	2.22	am	2
SrO	67.2	0.33	2	10.52	Cr	1

(+) This value is calculated by extrapolation from higher temperature data given in ref. (36).

2) The anodic-oxide film formed on Bi is, as predicted, found to be amorphous (37). However, the formation field under which the anodic film was formed was not reported. The present model predicts E_f to be $> 3.2 \times 10^8$ V/m.

3) Exploring the predictions for the cases of Ca, Li, Sr and to some extent Mg does not seem useful due to the instability of these metals in air and their tendency to decompose to hydroxides in solutions containing water. However, it might be worth trying to anodize Mg in non-aqueous electrolytes and explore the prediction of the formation of a crystalline anodic film.

4) With the remaining two cases Pb and Cr, where it seems plausible that one might form an anodic-oxide film, it is worth trying to explore the prediction for Pb. On the other hand, since Cr presents a borderline case, one may try to change E_f while forming the anodic film so that one may get variously either an amorphous or crystalline film.

7.6 Inadequacies in the Present Crystallization Model

In spite of the fact that the present criterion appears to be reasonably successful in predicting the structure of anodic-oxide films, it should be pointed out that some points have been overlooked. These points can be summarized as follows:

1) The assignment of bulk values to the surface energy γ_{SL} and the free energy of crystallization ΔG_c for volumes of nuclei containing few molecules constitutes one of the real limitations of classical nucleation treatment as presented here. However, as discussed in Sec. 7.3.2, the non-classical treatment of Cahn and Hilliard(26) does not offer an advantage in treatment that is relevant to our case.

2) The assumption that ΔG_c causes a free energy gradient that is confined only to the jump distance λ_M at the interface is quite arbitrary. However, the alternative of defining some greater thickness would be equally arbitrary, whereas the use simply of λ_M at least has precedent in the work of Csepregi et al.(28,29) From another point of view, the assumption of ΔG_c being confined to the distance λ_M gives reasonable structural predictions.

REFERENCES TO CHAPTER 7

1. M.T. Thomas, J. Electrochem. Soc., 117 (1970) 396.
2. E. Giani and R. Kelly, ibid., 121 (1974) 394.
3. S.M. EL Raghy (University of Cairo), personal communication (1975).
4. P.H.G. Draper and J. Harvey, Acta Met., 11 (1963) 873.
5. D.G. Brandon, J. Zahavi, A. Aladjem and J. Yahalom, J. Vac. Sci. Technol., 6 (1969) 783.
6. S. Zwerdling and S. Sheff, J. Electrochem. Soc., 107 (1960) 338.
7. M.A. Wilkins, Harwell (U.K.) Report AERE-R5875 (1968).
8. R.A. Harrington and H.R. Nelson, AIMME Inst. Metals, 137 (1940) 62.
9. M.R. Arora and R. Kelly, J. Electrochem. Soc., 119 (1972) 270.
10. M.R. Arora and R. Kelly, J. Materials Science, 12 (1977) 1673.
11. R. Kelly and N.Q. Lam, Rad. Effects, 19 (1973) 39.
12. D.A. Vermilyea, J. Electrochem. Soc., 102 (1955) 207.
13. M.R. Arora and R. Kelly, ibid., 120 (1973) 128.
14. O. Flint, J.J. Polling and A. Charlesby, Acta Met., 2 (1954) 696.
15. Sun, J. Am. Ceram. Soc., 30 (1947) 277.
16. H. Rawson, Inorganic Glass-Forming Systems, Academic Press (1967).
17. A.F. Wells, Structural Inorganic Chemistry, 3rd Edition, Oxford University Press (1967).
18. H.M. Naguib and R. Kelly, Rad. Effects, 25 (1975) 233.
19. T. Parker and R. Kelly "Proceedings of the 3rd International Conference on Ion Implantation of Semi-Conductors and Other Materials, Plenum, New York (1973) 551.
20. D.B. Rogers, R.D. Shannon, A.W. Sleight and J.L. Gillson, Inorg. Chem., 8 (1969) 841.

21. D. Turnbull, Modern Aspects of the Vitreous State, Editor J.D. Mackenzie, Vol. I, Butterworths, London (1960) 38.
22. JANAF Thermochemical Tables, D.R. Stull and H. Prophet, NSRDS-NBS, 37 (1971).
23. JANAF Thermochemical Tables, 1974 Supplement, J. Physical and Chemical Reference Data, Vol. 3 (1974) 311-480.
24. JANAF Thermochemical Tables, 1975 Supplement, ibid., Vol. 4 (1975) 1-75.
25. J.H. Brophy, R.M. Rose and J. Wulff, The Structure and Properties of Materials, Vol. II, John Wiley and Sons (1964) 52.
26. J.W. Cahn and J.E. Hilliard, J. Chem. Phy., 31, (1959) 688.
27. W.W. Smeltzer, R.R. Haering and J.S. Kirkaldy, Acta Met., 9, 880 (1961).
28. L. Csepregi, J.W. Mayer and T.W. Sigmon, Applied Physics Letters, A54 (1975) 157.
29. L. Csepriġi, R.P. Kullen and J.W. Mayer, Solid State Communications, 21, (1977) 1019.
30. M.R. Arora and R. Kelly, Electrochim. Acta , 19 (1974) 413.
31. A. Charlesby, Acta Met., 1 (1953) 340.
32. J.J. Polling and A. Charlesby, Proc. Phys. Soc., 67B (1954) 201.
33. S. Yamaguchi, J. Electrochem. Soc., 108 (1961) 302.
34. J. Siejka, J.P. Nadai, and G. Amsel, ibid., 118 (1971) 727.
35. K.E. Heusler, Ber. Bunsengesellschaft, 67 (1963) 943.
36. I. Barin, O. Knacke and O. Kubaschewski, Thermochemical Properties of Inorganic Substances, Supplement, Springer-Verlag, Dusseldorf (1977) 93.
37. S. Ikonopisov, L. Andreeva and Ts. Nikolov, J. Electrochem. Soc., 120 (1973) 717.

APPENDIX I

Calculations of λ_M, the mean molecular spacing, for some oxides:

$$\lambda_M = (M/\rho N_o)^{1/3}$$

where M = molecular weight

ρ = density of the oxide

$N_o = 6.023 \times 10^{23}$ molecule/mol.

Oxide	M (g/mol)	ρ (g/cm^3)	λ_M (nm)
Al_2O_3	101.96	3.97	0.35
B_2O_3	69.64	2.46	0.36
BeO	25.01	3.01	0.24
Bi_2O_3	495.96	8.55	0.46
CaO	56.08	3.32	0.30
Cr_2O_3	151.99	5.21	0.37
K_2O	94.2	2.32	0.41
Li_2O	29.88	2.01	0.29
MgO	40.31	3.58	0.27
MoO_3	143.94	4.69	0.37
Na_2O	61.98	2.27	0.36
Nb_2O_5	265.81	4.47	0.46
PbO	223.21	9.53	0.34
SiO_2	60.08	2.65	0.34
SrO_2	103.62	4.7	0.33
Ta_2O_5	441.89	8.2	0.45
TiO_2	79.9	4.26	0.32
V_2O_5	181.88	3.36	0.45
WO_3	231.85	7.16	0.38
ZrO_2	123.22	5.6	0.34

CHAPTER 8

SUMMARY AND SUGGESTIONS FOR FUTURE RESEARCH

8.1 Summary

1) The results presented here have shown that the behavior of Be with regard to anodization is much like that of Al and Sn. Porosity, dissolution, and crystallinity can be varied almost at will depending on the electrolyte. A fairly good correlation is shown to exist between the three possible results when anodizing is attempted, namely dissolution alone, both formation and dissolution of a film, and film formation alone, and the pH as predicted by the Pourbaix diagram. Doping, i.e., electrolyte incorporation, also plays a role, however, and it is therefore difficult to judge whether pH or doping is more important in particular cases.

2) It has been demonstrated for the first time that Be can be anodized under controlled conditions such that a protective, stable, and amorphous film is formed. The key lies in the use of neutral non-aqueous electrolytes based on ethylene glycol. The formation of such films is in principle of importance in the understanding of anodic oxidation from an electrochemical point of view, but it was regarded here as being of greater interest to work on diffusion and ion-solid collisions. It led in this work to establishing a microsectioning technique, hence to the possibility of studying diffusion and ion depth distributions in Be, the latter being of particular interest in view of the low mass of Be. It led also to the possibility of studying secondary particle emission from BeO and the possibility of correlating the depth profiles of incorporated anions with the mechanism of film formation.

3) The metal-removal and oxide thicknesses were calibrated. The oxide "thicknesses", actually weights, were about 20-25% higher than expected from the metal-removal thicknesses. This was found to be understandable in terms of the incorporation of electrolyte constituents into the anodic films, such that 5-10% of the O^{-2} in the film appears to be replaced with SO_4^{-2} or HPO_4^{-2}. The important detail here seems to be the significant doping of the films formed in the sulphate-containing electrolytes, as such films show on enhanced dissolution rate in 10% KOH and can therefore be quantitatively removed.

4) Depth distributions in Be showed the expected mixture of random and channelled stopping, whereas those in BeO showed random stopping alone. The latter is of interest in constituting an independent proof that anodic BeO is amorphous.

5) The emitted photons during bombardment Be and BeO anodic films are found to have discrete energies with significantly higher yields from the oxide than the metal. This has made it possible to profile anodic films on Be, as well as Zr, in spite of the lack of a useful oxygen signal. As the oxide thicknesses were known, sputtering coefficients for BeO and ZrO_2 were determined and found to be 4.3 ± 0.6 and 2.1 ± 0.3 atom/ion, for 12 keV Kr. These values indicate "normal" sputtering, as distinct from thermal sputtering, and suggested that it is feasible to sputter-profile BeO and ZrO_2 anodic films.

6) The depth profiles of incorporated electrolyte components (B, P and S) in the anodic films on Be and Zr were determined by the photon emission technique. In all cases, including Al from previous work, the film

is found to consist of two parts. The outer part includes the incorporated material from the electrolyte, while the inner part is almost pure oxide. However, the thickness ratios differ greatly from one case to the other, with Be at one end, Zr at the other, and Al an intermediate case.

7) The mechanism of film growth during anodizing of Be, Al and Zr is discussed, based on the fraction of the doped thickness in the above profiles. As a result, cation transport numbers are inferred and found to be 0.76 ± 0.06 (Be), 0.45 ± 0.1 (Al) and 0.12 ± 0.03 (Zr). The transport numbers are found to correlate with the nature of the mobile defect in the oxide as inferred from self-diffusion work. On the other hand, the similarity between the present and previous results for Al and Zr serves as an indication for the effectiveness of the approach used.

8) A criterion for the structure of anodic-oxide films has been developed based on the kinetics of the formation and crystallization processes of the oxide. This criterion has been applied to all cases for which information is available and the state of crystallinity of the anodic films as predicted was found to be, in all cases, the same as that reported. Furthermore, the criterion was explored to make predictions for unstudied systems.

9) Finally, the principles of anodic sectioning Be have been described here in such a way as to emphasize a "logic", insofar as one exists. For example, a systematic effort was made to establish conditions under which an anodic film could be formed which is simultaneously barrier-type, stable, doped and amorphous. In particular, the mechanism of film growth on Be was seen to involve cation transport, and from this one can under-

stand why doping was possible, thence why the film chemistry could be controlled. These principles can be used as a guide for establishing anodic sectioning procedures with still unstudied systems. We may point out that the problem of anodically sectioning Zr, which forms a barrier film in many electrolytes, lies in the difficulty of stripping the anodic films. This can now be understood in terms of the above principles, in that doping anodic ZrO_2 is not possible since film formation involves anion transport. The film chemistry cannot therefore be altered.

8.2 Future Work

1) Anodic-sectioning techniques should now be developed for materials of high technical importance like Pb, Fe and Zn with particular emphasis on doping and on the use of non-aqueous electrolytes. We may point out that anodic-oxide films on Pb were predicted by this work to form more likely in the amorphous state, hence it is highly probable that the anodic sectioning of Pb can be achieved. Preliminary work with Fe has already been carried out in a recent demonstration that barrier-type films can be formed provided phosphate doping is exaggerated.

2) The relatively incomplete knowledge of the diffusion behavior of Be can now be extended to lower temperatures by the use of the anodic sectioning technique.

3) Refinements of some of the details of the crystallization model developed here for explaining anodic-film structure is needed. Also important is to try to extend the model so that it can be employed to describe the crystallization of amorphous solids in general.